

**REDESIGN OF A HIGH-PRESSURE, SINGLE-SINKER MAGNETIC
SUSPENSION DENSIMETER TO MEASURE HIGHLY ACCURATE
DENSITIES FOR FLUIDS: APPLICATIONS TO HELIUM, ARGON, AND
HELIUM + METHANE MIXTURES**

A Dissertation

by

ROBERT ALLEN BROWNE

Submitted to the Office of Graduate and Professional Studies of
Texas A&M University
in partial fulfillment of the requirements for the degree of

DOCTOR OF PHILOSOPHY

Chair of Committee,	James Holste
Co-Chair of Committee,	Kenneth Hall
Committee Members,	Perla Balbuena
	Maria Barrufet
Head of Department,	Nazmul Karim

December 2017

Major Subject: Chemical Engineering

Copyright 2017 Robert Allen Browne

ABSTRACT

The petrochemical industry requires highly accurate equations of state (EoS) to calculate thermodynamic properties such as densities and calorific properties. However, the accuracy of an EoS depends upon the accuracy of the data used to construct it. Thus, a need exists for high accuracy p - ρ - T measurements. Multiple apparatus can provide high accuracy p - ρ - T measurements, but they do not operate over broad ranges of pressure and temperature. One apparatus that can operate over a broad range is a single sinker magnetic suspension densimeter (MSD). This work presents the redesign of the TAMU MSD.

This apparatus is a unique MSD because its pressure measurement range extends to 200 MPa. A system redesign has enabled the apparatus to achieve a temperature range of 300 to 500 K. The redesign entailed creating a new electrical heating system, heating shields, vacuum insulation, and new frame. Improvements for the measurement processes of the system include a new measurement sequence that reduces measurement time by approximately half.

After recommissioning the MSD, nitrogen measurements validated the system performance. After verifying system accuracy, measurements included two pure fluids, helium and argon, from 300 to 450 K up to 200 MPa. Additional measurements included three binary mixtures of methane + helium covering the same property ranges.

Finally, this work proposes a new approach to creating mixing rules for binary mixtures of “simple” molecules based upon a quadratic compositional dependence of the residual Helmholtz energy. This approach describes the contributions from interactions between unlike molecules with an interaction Helmholtz energy. A rational polynomial in

density with coefficients having both temperature and compositional dependence describes these interactions within the accuracy of experimental measurements. This form is less complex than other mixture models that include exponential terms in density, thus the approach is more attractive for process modeling. Mixtures containing methane, ethane, nitrogen, carbon dioxide, argon, hydrogen, krypton and helium provide tests for the mixing rule.

DEDICATION

To my parents, family, and friends for whose support I will be forever grateful.

ACKNOWLEDGEMENTS

I would like to thank my committee chairs, Dr. James Holste and Dr. Kenneth Hall, first for the opportunity to be a part of their research group and for all the knowledge and guidance they have given me over the years. They have contributed a large amount to both my personal and professional development and I am forever grateful.

I would like to thank my committee member Dr. Maria Barrufet for her guidance and advice as well as providing resources to help solve issues I encountered during a project.

I would like to thank my committee member Dr. Perla Balbuena not only for her guidance and advice but also for growing my interest in Thermodynamics during my first semester course with her.

Thanks also go to Dr. Mark McLinden at NIST for his assistance, recommendations, and discussions throughout the design process. Also, thanks to Dr. Eric Lemmon at NIST for sharing data with me. Thanks to both Randy Marek and Jason Caswell for their technical knowledge and assistance in construction of multiple components needed for the experiments.

Thanks to all my team members, Martin Gomez, Diego Ortiz, Pilar Suarez, Catherine Sampson, Diego Cristancho, and Andrea Tibaduiza for all their exchanges of knowledge, lessons they taught me, and seeing me through the highs and lows. Thanks to Shashank Kamdar, Mauricio Carvajal, William Prieto, and Robert Blando for their help throughout my work. Thanks to the department faculty, staff, and students for making my time at Texas A&M University a great experience.

Finally, thanks to my mother, father, and my entire family for their encouragement and patience throughout this process and Edna Mendez for supporting me and helping me throughout my work.

TABLE OF CONTENTS

	Page
ABSTRACT	ii
DEDICATION	iv
ACKNOWLEDGEMENTS	v
TABLE OF CONTENTS	vii
LIST OF FIGURES.....	x
LIST OF TABLES	xvi
1. INTRODUCTION.....	1
1.1. Experimental methods and apparatus for density measurements	3
1.1.1. Burnett apparatus	3
1.1.2. Isochoric apparatus	4
1.1.3. Continuously weighed pycnometer	5
1.1.4. Vibrating tube densimeter	5
1.1.5. Hydrostatic buoyant force and magnetic suspension densimeter	8
1.2. Data sets for pure fluids and helium + methane mixtures	21
1.2.1. Argon data sets	21
1.2.2. Helium data sets	22
1.2.3. Helium + methane data sets	25
1.3. Fundamental equations of state and current reference equations	25
1.4. Objectives	28
2. SINGLE SINKER MAGNETIC SUSPENSION DENSIMETER	
APPARATUS	30
2.1. Apparatus description	33
2.1.1. High pressure measurement cell and balance	33
2.1.2. Suspension and coupling system	39
2.1.3. Mounting and alignment system	40
2.1.4. Measurement sequence	45
2.1.5. Temperature measurement.....	46
2.1.6. Heaters and heating shields.....	51
2.1.7. Vacuum chamber and feedthroughs	63
2.2. Auxiliary systems	67
2.2.1. Feed and compression system manifold	67
2.2.2. High vacuum system.....	71

2.3. Temperature measurement methodology and control	75
2.4. Pressure measurement	78
2.5. LabVIEW data acquisition	83
2.6. Silicon sinker	88
2.7. Re-commissioning and checking for bias errors	90
3. DENSITY MEASUREMENTS	92
3.1. Uncertainty analysis	92
3.2. Pure components density measurements	94
3.2.1. Nitrogen	94
3.2.2. Argon	95
3.2.3. Helium	99
3.3. Methane + helium mixtures	104
3.3.1. Sample preparation	105
3.3.2. 75% Methane + 25% helium	107
3.3.3. 45% Methane + 55% helium	110
3.3.4. 25% Methane + 75% helium	110
3.3.5. Replicate mixtures	114
4. MIXING RULE BASED UPON RESIDUAL HELMHOLTZ ENERGY	120
4.1. Mixing rules of a virial equation	120
4.2. Mixing rule based upon residual Helmholtz free energy.....	122
4.2.1. GERG mixing rules	123
4.2.2. Interaction residual Helmholtz energy based upon a polynomial (rational) form.....	127
4.2.3. Fit results.....	132
5. CONCLUSIONS AND RECOMMENDATIONS.....	181
REFERENCES	184
APPENDIX A	199
APPENDIX B	201
APPENDIX C	202
APPENDIX D	203
APPENDIX E.....	212
APPENDIX F.....	214

APPENDIX G	217
APPENDIX H	240

LIST OF FIGURES

	Page
Figure 1. Graph of deepwater oil and gas projects [2]	2
Figure 2. Overview of a VTD [14].....	7
Figure 3. The two-sinker MSD developed by Kleinrahm and Wagner (modified from [21])	11
Figure 4. Compact single sinker MSD [28]	13
Figure 5. Overview of the TAMU MSD [22]	15
Figure 6. The operations of the MSD (modified from Rubotherm Operating Instructions [39])	16
Figure 7. Weighing scheme and changing device with the Ta weight on the left and Ti weight on the right [40].....	17
Figure 8. Distribution in pressure and temperature of the experimental data used to develop the argon reference EoS [49]	23
Figure 9. Distribution in pressure and temperature of the experimental data used to develop the helium reference EoS [50]	24
Figure 10. Previous MSD design [40].....	31
Figure 11. MSD after the completed redesign	32
Figure 12. Cross section of weighing balance from Mettler Toledo [67]	35
Figure 13. Overview of the MSD and dimensions in mm [39].....	36
Figure 14. Electrical feed-through to the balance	38
Figure 15. Position sensor box	41
Figure 16. Electromagnet (EM) hanging from the balance.....	44
Figure 17. New thermopile.....	48
Figure 18. Electrical terminal box for the thermometry leads	50
Figure 19. Example of a typical electrical heater that was used for the shield supports	52

Figure 20. Inner Shield.....	54
Figure 21. Outer Shield.....	55
Figure 22. Outer shield support attached to EM clamp.....	57
Figure 23. Lower radiation shield.....	59
Figure 24. Cross section of the upper radiation shield (not drawn to scale).....	61
Figure 25. Upper radiation shield.....	62
Figure 26. Feedthrough collar.....	64
Figure 27. RTD feedthrough flange.....	66
Figure 28. Compression system for the MSD with solid lines for the fluid of interest and dashed lines for compressing gases.....	69
Figure 29. FPS system used in the MSD.....	72
Figure 30. Schematic diagram of high vacuum pumping system for MSD.....	73
Figure 31. The high vacuum system (mechanical pump not shown).....	74
Figure 32. Current sources fabricated by the physics electronics shop at TAMU.....	76
Figure 33. Heater power control box.....	79
Figure 34. Overview of temperature measurement and control system.....	80
Figure 35. Pressure transducer setup [22].....	82
Figure 36. Overview of the communication between the equipment used in the mass measurements.....	85
Figure 37. Illustrates the LPT port pin combination required for controlling the suspension coupling and weight changing device [71].....	86
Figure 38. Image of the table for pin combination commands for the balance [71].....	87
Figure 39. Relative deviations of measured nitrogen densities compared to Span <i>et al.</i> [47] reference EoS for this work × 303 K, + 398 K and Mantilla <i>et al.</i> [32] □ 298.15 K, Δ400 K.....	96

Figure 40. Relative deviations of measured argon densities compared to the Tegeler <i>et al.</i> [49] reference EoS for this work \square 303 K, \diamond 350 K, + 400 K, and Δ 450 K	97
Figure 41. Relative deviations of measured helium densities compared to the Ortiz-Vega <i>et al.</i> [50] reference EoS for this work \square 303 K, + 350 K, * 399 K, and Δ 450 K	100
Figure 42. Relative deviations of measured helium densities at \sim 303 K from the Ortiz-Vega <i>et al.</i> [50] reference EoS using the silicon sinker (Δ) with error bars and the titanium sinker before (\square) and after (\diamond) the silicon sinker was installed.....	103
Figure 43. Process flow diagram of the in-house mixing apparatus	106
Figure 44. Relative deviations of measured densities from \square GERG-2008 [57] and \circ AGA8-DC92 [58] for methane ($x \approx 0.75$) + helium mixtures at 303 K, 350 K, 396 K and 450 K.....	109
Figure 45. Relative deviations of measured densities from \square GERG-2008 [57] and \circ AGA8-DC92 [58] for methane ($x \approx 0.45$) + helium mixture at 303 K, 350 K, 398 K and 450 K.....	111
Figure 46. Relative deviations of measured densities from \square GERG-2008 [57] and \circ AGA8-DC92 [58] for methane ($x \approx 0.25$) + helium mixture at 303 K, 350 K, 397 K and 450 K.....	112
Figure 47. Relative deviations of measured densities from GERG-2008 [57] for \square methane ($x \approx 0.75$) + helium and Δ methane ($x \approx 0.73$) + helium and from AGA8-DC92 [58] for \circ methane ($x \approx 0.75$) + helium and * methane $x \approx 0.73$) + helium at 303 K.....	116
Figure 48. Relative deviations of measured densities from GERG-2008 [57] for \square methane ($x \approx 0.55$) + helium and Δ methane ($x \approx 0.50$) + helium and from AGA8-DC92 [58] for \circ methane ($x \approx 0.55$) + helium and * methane ($x \approx 0.50$) + helium at 303 K.....	117
Figure 49. Relative deviations of measured densities from GERG-2008 [57] for \square methane ($x \approx 0.25$) + helium and Δ methane ($x \approx 0.26$) + helium and from AGA8-DC92 [58] for \circ methane ($x \approx 0.25$) + helium and * methane ($x \approx 0.26$) + helium at 303 K	118
Figure 50. Relative deviations of measured densities from AGA8-DC92 for methane ($x \approx 0.50$) + helium sample for this work Δ 303 K and Hernández-Gómez <i>et al.</i> [55] \square 299 K.....	119

Figure 51. Overview of the mixtures included in GERG [57]	126
Figure 52. Relative deviation of the measured compressibility factors from the EoS predictions for methane + nitrogen mixtures	136
Figure 53. Relative deviation of the measured compressibility factors from the EoS predictions for methane + nitrogen mixtures: this work (\diamond), GERG (\square)	137
Figure 54. Relative deviation of the measured compressibility factors from the EoS predictions for methane + ethane mixtures	140
Figure 55. Relative deviation of the measured compressibility factors from the EoS predictions for methane + ethane mixtures: this work (\diamond), GERG (\square)	141
Figure 56. Relative deviation of the measured compressibility factors from the EoS predictions for nitrogen + carbon dioxide mixtures	144
Figure 57. Relative deviation of the measured compressibility factors from the EoS predictions for nitrogen + carbon dioxide mixtures: this work (\diamond), GERG (\square)	145
Figure 58. Relative deviation of the measured compressibility factors from the EoS predictions for methane + carbon dioxide mixtures	148
Figure 59. Relative deviation of the measured compressibility factors from the EoS predictions for methane + carbon dioxide mixtures: this work (\diamond), GERG (\square)	149
Figure 60. Relative deviation of the measured compressibility factors from the EoS predictions for ethane + carbon dioxide mixtures	152
Figure 61. Relative deviation of the measured compressibility factors from the EoS predictions for ethane + carbon dioxide mixtures: this work (\diamond), GERG (\square)	153
Figure 62. Relative deviation of the measured compressibility factors from the EoS predictions for argon + nitrogen mixtures	156
Figure 63. Relative deviation of the measured compressibility factors from the EoS predictions for argon + nitrogen mixtures: this work (\diamond), GERG (\square)	157
Figure 64. Relative deviation of the measured compressibility factors from the EoS predictions for hydrogen + nitrogen mixtures	160

Figure 65. Relative deviation of the measured compressibility factors from the EoS predictions for hydrogen + nitrogen mixtures: this work (\diamond), GERG (\square)	161
Figure 66. Relative deviation of the measured compressibility factors from the EoS predictions without compositional dependence in n_4 for helium + argon mixtures (+ $x_{\text{He}} = 0.80$, \times $x_{\text{He}} = 0.60$, \diamond $x_{\text{He}} = 0.41$, and \square $x_{\text{He}} = 0.22$)	163
Figure 67. Relative deviation of the measured compressibility factors from the EoS predictions with compositional dependence in n_4 for helium + argon mixtures (+ $x_{\text{He}} = 0.80$, \times $x_{\text{He}} = 0.60$, \diamond $x_{\text{He}} = 0.41$, and \square $x_{\text{He}} = 0.22$)	164
Figure 68. Relative deviation of the measured compressibility factors from the EoS predictions for the current model (\diamond) and GERG (\square) for mixtures of helium + argon.....	165
Figure 69. Relative deviation of the experimental compressibility factors from the equation of state predictions He + Kr mixtures with no composition dependence in the interaction residual Helmholtz energy (\times He 0.25, \diamond He 0.50, and \square He 0.75)	167
Figure 70. Relative deviation of the measured compressibility factors from the EoS predictions for He + Kr mixtures with additional composition dependence in the interaction residual Helmholtz energy (\times He 0.25, \diamond He 0.50, and \square He 0.75)	168
Figure 71. Relative deviation of the measured compressibility factors from the EoS predictions for helium + nitrogen mixtures without composition dependence in n_4	171
Figure 72. Relative deviation of the experimental compressibility factors from the EoS predictions for helium + nitrogen mixtures without composition dependence in n_4 for Briggs <i>et al.</i> [97] data (\times He 0.90, \diamond He 0.80, \square He 0.70, + He 0.60, * He 0.50, o He 0.40, Δ He 0.30, \star He 0.20, and \triangleright He 0.10).....	172
Figure 73. Relative deviation of the experimental compressibility factors from the EoS predictions for helium + nitrogen mixtures with composition dependence in n_4	174
Figure 74. Relative deviation of the experimental compressibility factors from the EoS predictions for helium + nitrogen mixtures with composition dependence in n_4 for Briggs <i>et al.</i> [97] data (\times He 0.90, \diamond He 0.80, \square He	

0.70, + He 0.60,* He 0.50, o He 0.40, Δ He 0.30, ☆ He 0.20, and ▷ He 0.10).....	175
Figure 75. Relative deviation of the experimental compressibility factors from the EoS predictions for the current model (◇) and GERG (□) for mixtures of helium + nitrogen.....	176
Figure 76. Relative deviations of experimental compressibility factors from the EoS predictions for helium + methane mixtures with composition dependence in n_2 but not n_4 (□ He 0.75, ◇ He 0.55, × He 0.25).....	178
Figure 77. Relative deviations of the experimental compressibility factors from the EoS predictions for helium + methane mixtures with composition dependence in both n_2 and n_4 (□ He 0.75, ◇ He 0.55, × He 0.25)	179
Figure 78. Relative deviation of the measured compressibility factors from the EoS predictions for helium + methane mixtures: this work (◇), GERG (□)	180

LIST OF TABLES

	Page
Table 1. Supply gas cylinder specifications	93
Table 2. Argon measurement uncertainties	98
Table 3. Helium measurement uncertainties	101
Table 4. Mixture masses, compositions and uncertainty	108
Table 5. Methane + helium measurement uncertainties.....	113
Table 6. Replicate mixture masses, compositions and uncertainty	115
Table 7. Methane + nitrogen mixture data used in the fit	135
Table 8. Methane + ethane mixture data used in the fit	139
Table 9. Nitrogen + carbon dioxide mixture data used in the fit	143
Table 10. Methane + carbon dioxide mixture data used in the fit.....	147
Table 11. Ethane + carbon dioxide mixture data used in the fit.....	151
Table 12. Argon + nitrogen mixture data used in the fit	155
Table 13. Hydrogen + nitrogen mixture data used in the fit	159
Table 14. Helium + nitrogen mixture data used in the fit	170

1. INTRODUCTION

Energy plays a pivotal role in today's society with almost all facets of life connected to it. Most energy is derived from fossil fuels that are composed of deposited organic material. This includes coal, crude oil, and natural gas. Natural gas is the cleanest burning of the preceding options, which makes it an attractive energy source compared to the others.

In 2016, approximately 27.5 trillion cubic feet of natural gas was consumed in the United States, accounting for more than 29% of the overall consumption [1]. Accurate predictions in the physical properties are of great importance as even small errors in these properties could result in millions of dollars of uncertainty per year.

Computer-aided process design requires highly accurate equations of state (EoS) that provide accurate thermodynamic properties such as densities, entropies and energies. These properties can be used to optimize unit operations, safety, economics, processing and transportation of fluids. However, the accuracy of an EoS depends upon the accuracy of the data used to construct it. Thus, a great need exists for accurate p - ρ - T measurements. Many apparatus exist that can achieve highly accurate p - ρ - T measurements, but most cannot do so over a broad range of pressure and temperature. With deep gas reservoirs ranging in pressures from 138-200 MPa with temperatures reaching up to 478 K as shown in Figure 1, a need exists for an apparatus that can operate in these extreme ranges [2].

One such apparatus that can handle these harsh conditions is a magnetic suspension densitometer (MSD), which is the main focus of this work. Other apparatus for high accuracy p - ρ - T measurement include: Burnett, continuously-weighed

pycnometer, and isochoric [3]. These apparatus are discussed briefly in the following sections. For more details on these apparatus please refer to the density chapter in reference [4].

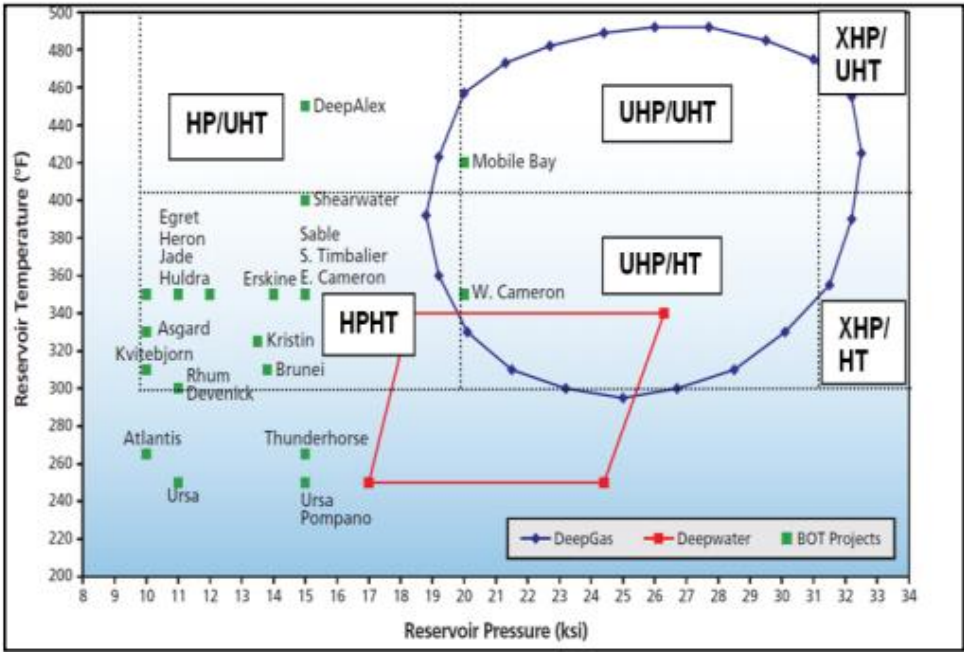


Figure 1. Graph of deepwater oil and gas projects [2]

1.1. Experimental methods and apparatus for density measurements

1.1.1. Burnett apparatus

A Burnett apparatus [5] contains two interconnected volumes inside an isothermal bath. Measurements consist of loading a fluid into one of the volumes (V_a) up to an initial pressure. Then, the interconnecting valve is opened and the sample is expanded into the other, evacuated volume (V_b) and allowed to equilibrate at the initial temperature. Once the system has reached equilibrium, the interconnecting valves are closed and the final pressure is recorded. The second volume is evacuated again and the process repeated until the pressure reaches the lower limit of the pressure measurement device [6]. Both densities and second and third virial coefficients can be estimated using this method [7, 8]. Density for the i -th expansion is calculated using the following:

$$\rho_i = \rho_m \pi_\infty^{m-i} \prod \frac{1 + \gamma_{ab} P_i}{1 + \gamma_a P_{i-1}} \quad (1.1)$$

in which

$$\pi_\infty = \lim_{p \rightarrow 0} \frac{V_a + V_b}{V_a} \quad (1.2)$$

Subscript m represents the final expansion, γ_j is the pressure distortion of the volume j (a or a+b), and π_∞ is the cell constant at zero pressure.

Although a Burnett apparatus provides accurate measurements, the main drawback is little control over the distribution of measured pressures because of fixed volumes for the expansions. Another drawback is that the system is very difficult to automate because

there is a frequent need to open and close valves and typically a dead weight gauge is used for the pressure measurements, which requires adjustment of a balancing pressure.

1.1.2. Isochoric apparatus

An isochoric apparatus is a simple apparatus that contains one cell with a well-defined volume and mass under vacuum and at a reference temperature. Measurements start with the sample being loaded into the cell and either weighed or calculated using prior knowledge of the density of the sample at the preset temperature and pressure to get the initial density. Typically, the latter method is preferred because it does not require frequent assembly and disassembly. The cell is placed in an isothermal bath along with an insulation system (typically a vacuum chamber) and set to a predetermined temperature. After the system reaches equilibrium, the pressure and temperature of the system is recorded.

Subsequently, the temperature of the system is adjusted and the system allowed to re-equilibrate at the new pressure. These steps are repeated in equal temperature steps until the isochore is completed; then a new isochore is started. This, in principle, is simple but because of distortions of the cell with changes in temperature and pressure and mass exchange with external volumes, corrections must be made to create “true” isochores [3]. Details on these effects and how to account for them may be found in Cristancho [9]. and Tibaduiza *et al.* [10].

One advantage of the isochoric apparatus is that it can be used to determine phase boundaries using the discontinuous change in slope of the isochore at the phase boundary

[11, 12]. Another advantage is that the experimental values give insight into the derivative $(\partial p / \partial T)_p$, which is difficult to derive from isothermal measurements. These derivatives can then be used in the calculation of energies and entropies as in shown by Tibaduiza *et al.* [10].

1.1.3. Continuously weighed pycnometer

In the continuously-weighed pycnometer [13], a sample cell of defined volume is suspended directly from a balance in an isothermal chamber. Taring the weight of the cell and feed line gives the mass of sample, which along with the volume of the cell (adjusted for temperature and pressure distortions) yields the density of the sample. This setup includes a design requirement that the feed line and other components do not add any variable loading on the balance. Another disadvantage of this apparatus is the inability to check for drifts in the balance and the possibility of additional forces acting on the balance skewing the mass measurement.

1.1.4. Vibrating tube densimeter

Another isothermal apparatus that can handle these harsh conditions is the vibrating tube densimeter (VTD). It consists of a hollow tube made out of a metallic or glass material bent in a “U” or “V” shape. The tube is then forced to vibrate by using a magnet, drive coil, and current source to produce a variable magnetic field. Another magnet is attached to the tube in different place and with the oscillation of the tube induces

current in a pick-up coil when then is converted into a frequency. A schematic of the system is shown in Figure 2.

A VTD can be modeled as a simple harmonic oscillator leading to the following relation between density and the period of oscillation (frequency);

$$r = a(T, p)t^2 - b(T, p) \quad (1.3)$$

Here α and β are determined empirically, semi-empirically [14, 15], or based upon physical parameters such as Young's modulus [16]. Although physical models exist, they can vary greatly with different apparatus and configurations. Thus, a reference and calibration fluids are still required to ensure accuracy [17]. Dependence upon calibration is one of the drawbacks of the VTD because the accuracy of the measurement is limited by the density uncertainties of the fluids chosen for calibration. A common reference point that is used is the vacuum ($\rho_f=0$) point. The vacuum parameters vary significantly with temperature, requiring an empirical relation between the temperature and frequency. One commonly used function is a simple quadratic in temperature [18, 19].

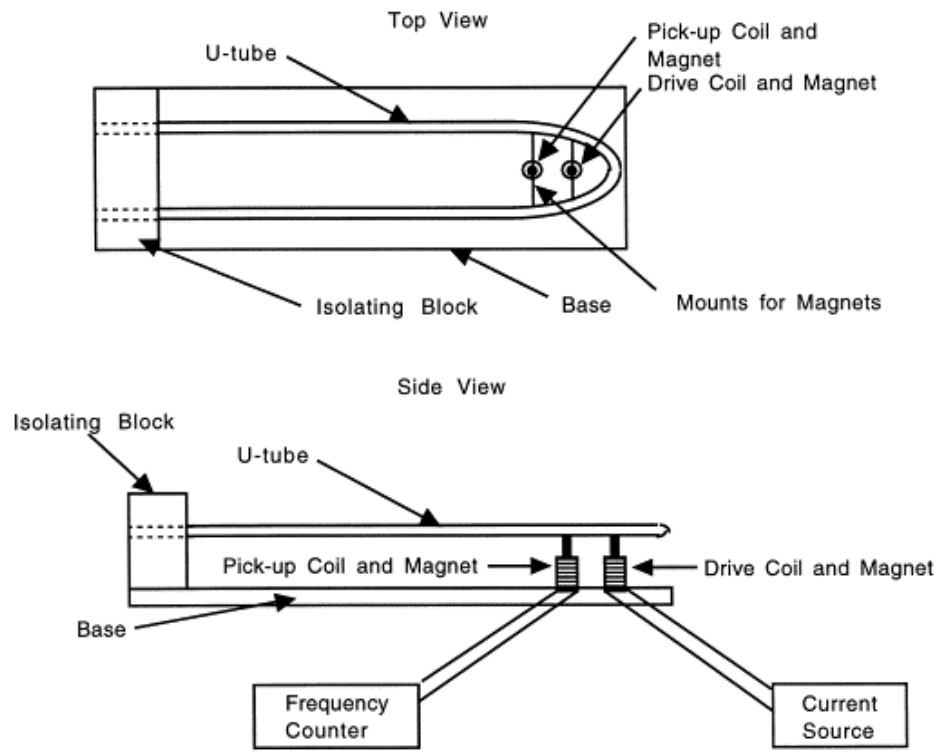


Figure 2. Overview of a VTD [14]

For calibration fluids, a well-known fluid with densities similar to the fluids of interest is chosen to reduce uncertainties. The uncertainties can be minimized by using another apparatus that does not depend upon fluid calibration, an MSD in our case, to validate an EoS or provide experimental values with which to compare. Gomez-Osorio *et al.* [19, 20] used the above steps for a high pressure VTD using the TAMU MSD. The pairing of these apparatus is useful because they complement each other's strengths. The VTD provides more rapid measurements than the MSD because of a smaller sample size. The MSD provides additional measurements at the selected conditions to ensure/validate the VTD measurements.

1.1.5. Hydrostatic buoyant force and magnetic suspension densimeter

The principle of a hydrostatic buoyancy balance is based upon Archimedes principle, which states that the buoyant force exerted on an object immersed in a fluid is equal to the weight of the fluid that the object displaced. This leads to the follow relation for the density of the fluid:

$$\rho_f = \frac{m_o - m_a}{V_o(T, p)} \quad (1.4)$$

in which ρ_f represents the density of the fluid being measured, m_o is the true mass of the object, which in our case is a cylindrical sinker, m_a is the mass of the sinker immersed in the fluid, and V_o is the volume of the object (sinker) that depends upon temperature and pressure. No calibration fluid is required to obtain accurate density measurements, but the mass and volume of the sinker must be known. Measurements were initially done by

suspending a wire from the bottom of a balance submerging the sinker in the fluid. These apparatus have multiple issues caused by the physical contact between the balance and sample of interest such as a limited operating range and surface tension effects on the suspended wire [21, 22].

To overcome the physical contact issue Masui *et al.* [23] and Kleinrahm and Wagner [24, 25] developed a hydrostatic density balance along with magnetic coupling in 1984. The non-physical contact from the coupling in [23-25] provides the benefit of measuring samples over wider ranges of temperature and pressure than most other apparatus.

1.1.5.1. Two sinker densimeters

In 1984, Kleinrahm and Wagner [24] developed a two-sinker magnetic suspension densimeter for density measurements of pure fluids in both the gas and liquid phase as well as the saturation curves. To achieve the non-physical contact an electromagnet (EM) is suspended from the bottom of an analytical balance and current is driven through the EM to lift a permanent magnet (PM) inside the sample cell using a position sensor, control system and feedback loop. Attached to the PM shaft is a lifting device that can pick up or lower the object that is used for the measurements. However, magnetic interactions between the PM, EM and the surrounding materials also introduce a force transmission error (φ) into the measurement. This effect is discussed in detail in section 1.1.5.4.

Two sinkers, a gold disk and a glass sphere, of the same mass and surface area but different volumes were used to negate any adsorption effects. This serves as one of the

main advantages over a single sinker densimeter, although it comes at the cost of a more complex system to manipulate two sinkers.

Kleinrahm and Wagner's densimeter has a temperature range of 60-340 K at pressures to 12 MPa. Reported uncertainties in density are 0.01-0.02% or 0.0015 kg m^{-3} , whichever is larger [21]. Figure 3 presents Kleinrahm and Wagner's two-sinker MSD design.

In 2007, McLinden and Lösch-Will developed a two-sinker densimeter similar to the one above with a wider temperature and pressure range (90-520 K up to 40 MPa) [26]. Density uncertainties are estimated at $0.015\% + 0.001 \text{ kg}\cdot\text{m}^{-3}$. Improvements compared to Kleinrahm and Wagner's apparatus are the more compact design, higher resolution in density, and smaller sample size leading to shorter equilibration times.

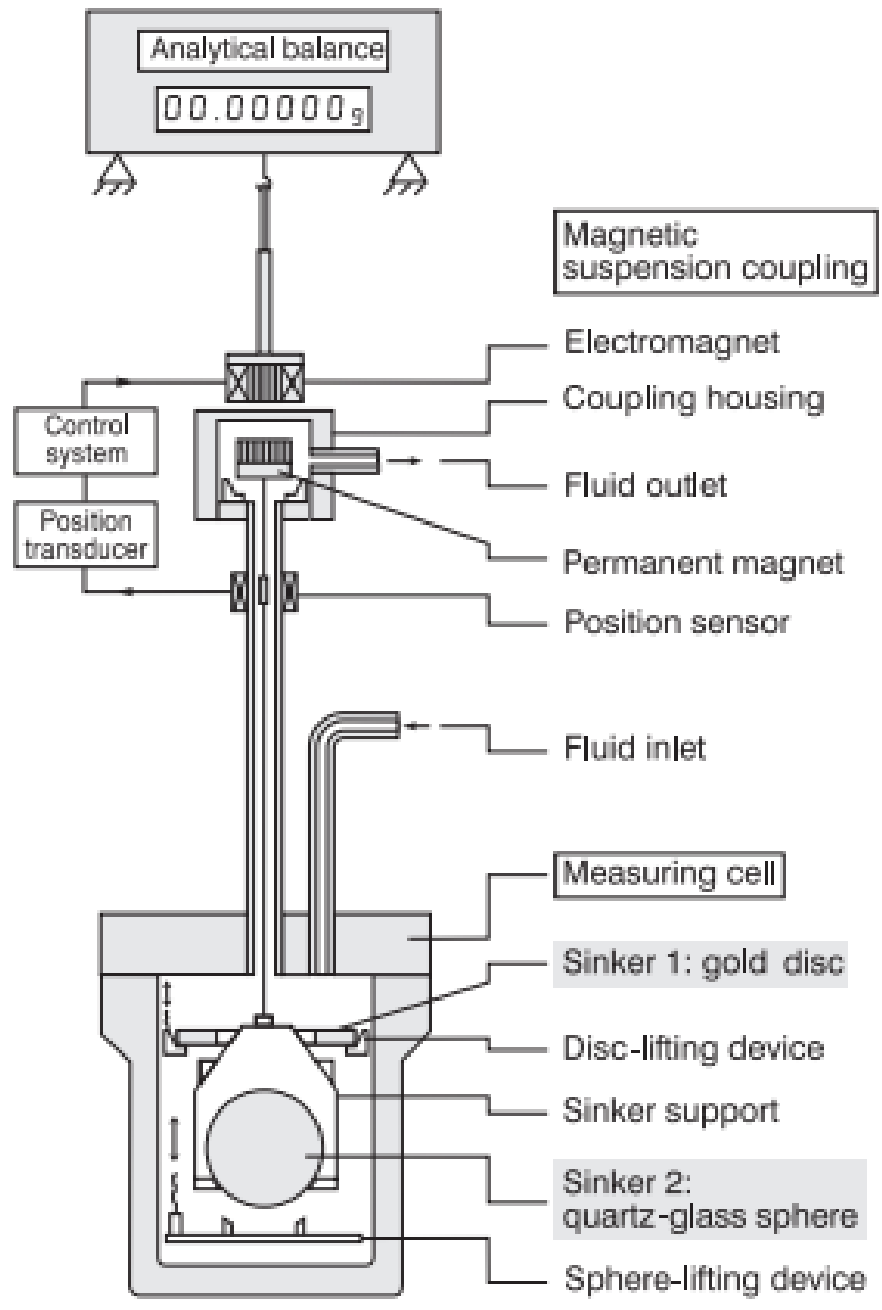


Figure 3. The two-sinker MSD developed by Kleinrahm and Wagner (modified from [21])

1.1.5.2. Single sinker densimeters

Two-sinker MSD are highly accurate over wide ranges of conditions, even at low densities. However, this comes with the complexities of manipulating two sinkers. These features are less important to many applications, for example measurement of mid-to-high density gases, so the apparatus was simplified. Brachthäuser *et al.* [27, 28] constructed a single sinker MSD for temperatures of 233-523 K and pressures up to 30 MPa. The operating principles and overall design are similar to that of a two sinker MSD with the communication between the EM and PM still being how the sinker is lifted and lowered but without a changing device as in the two sinker system. Figure 4 is a schematic of the system.

Single sinker MSD have been used successfully by multiple authors for gas and liquid density measurements, both saturated and supercritical, of pure fluids [29-33] and mixtures [34-36], as well as vapor-liquid equilibrium of refrigerants [37, 38]. Kleinrahm and Wagner [21] provide a detailed document with multiple examples of these apparatus.

This work focuses on the TAMU compact single sinker MSD constructed by Rubotherm Präzisionsmesstechnik GmbH in Germany and the redesign of its ancillary equipment for density measurements. The maximum operating pressure range for this MSD is up to 200 MPa at temperatures up to 400 K and declining to 173 MPa at 400-500 K. This operating pressure is unique among MSD.

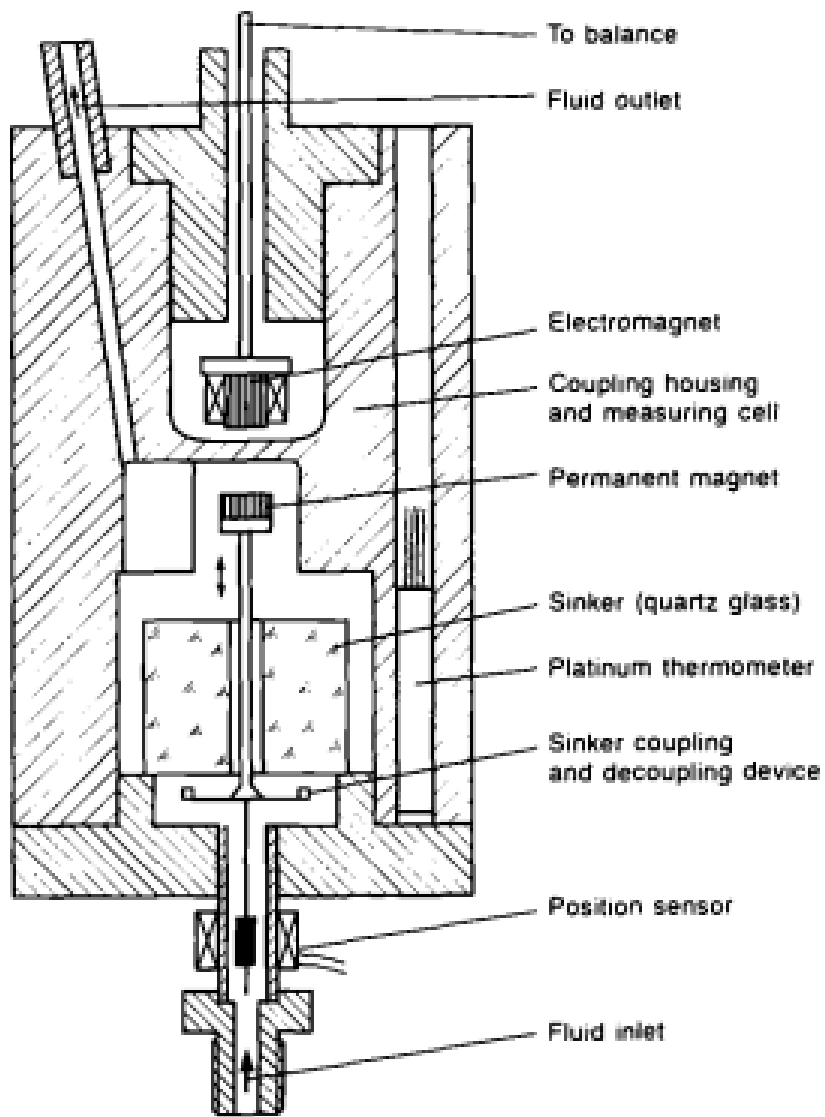


Figure 4. Compact single sinker MSD [28]

The nominal density range is 0-2,000 kg·m⁻³ however; this depends upon the type of sinker material that is used. More details of this limitation are provided in the next section. The accuracy of the apparatus as specified by Rubotherm [39] is 0.03% + 0.005 kg·m⁻³. Section 3 presents a detailed analysis of the total uncertainty for density measurements along with the experimental measurements. Drawings of our MSD and the different measurement sequences that are required for density measurements appear in Figure 5 and 6.

1.1.5.3. Density measurement cycles for the TAMU single sinker densimeter

Figure 6 and 7 show the three measurement positions used for density measurements. Point (a) is the “OFF” position and has the EM suspended from the balance, but not the PM or the sinker (the PM rests on the bottom of the cell). The “OFF” position is important for calibrating and aligning the balance.

Point (b) is the zero point position denoted as ZP. In this position, the PM is levitated, but the sinker is not. Also, shown in Figure 7 a tantalum compensation weight loaded on the balance pan. The purpose of the compensation weight is discussed in the following section.

Point (c) is the measurement point (MP) and is similar to the ZP; however, now the PM is lifts the sinker as well. The MP compensation weight is made of titanium.

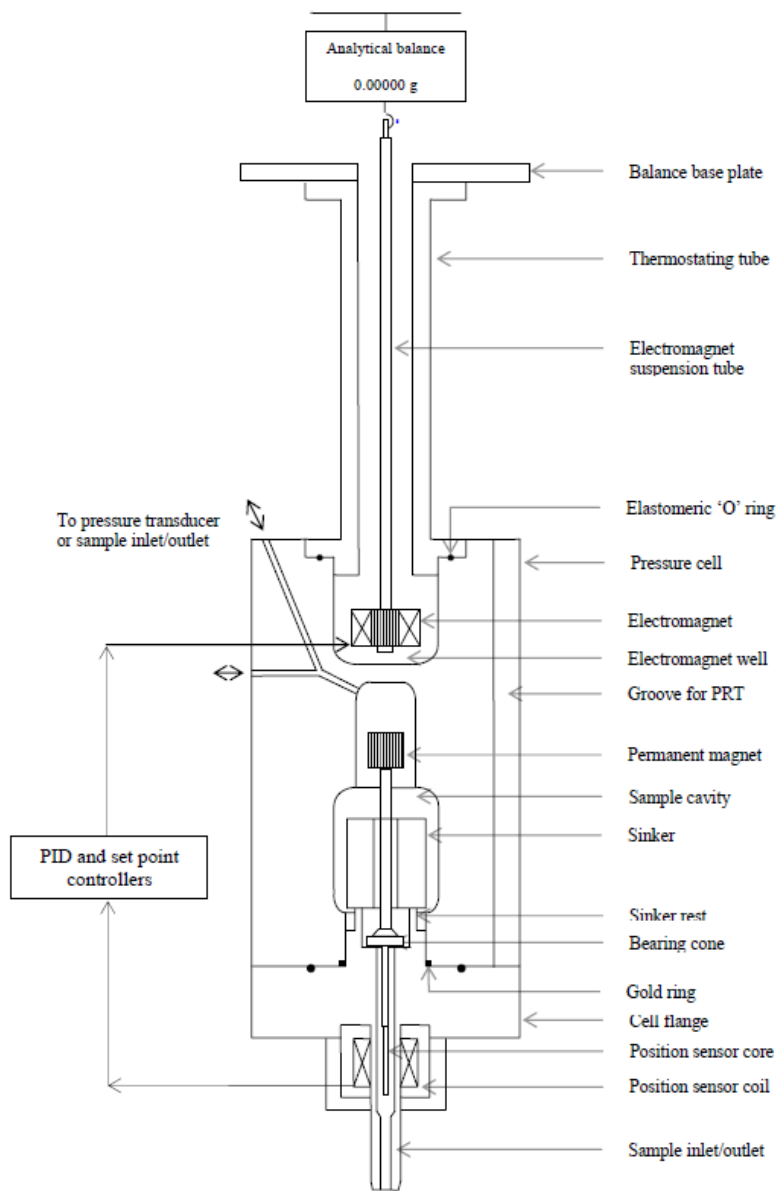
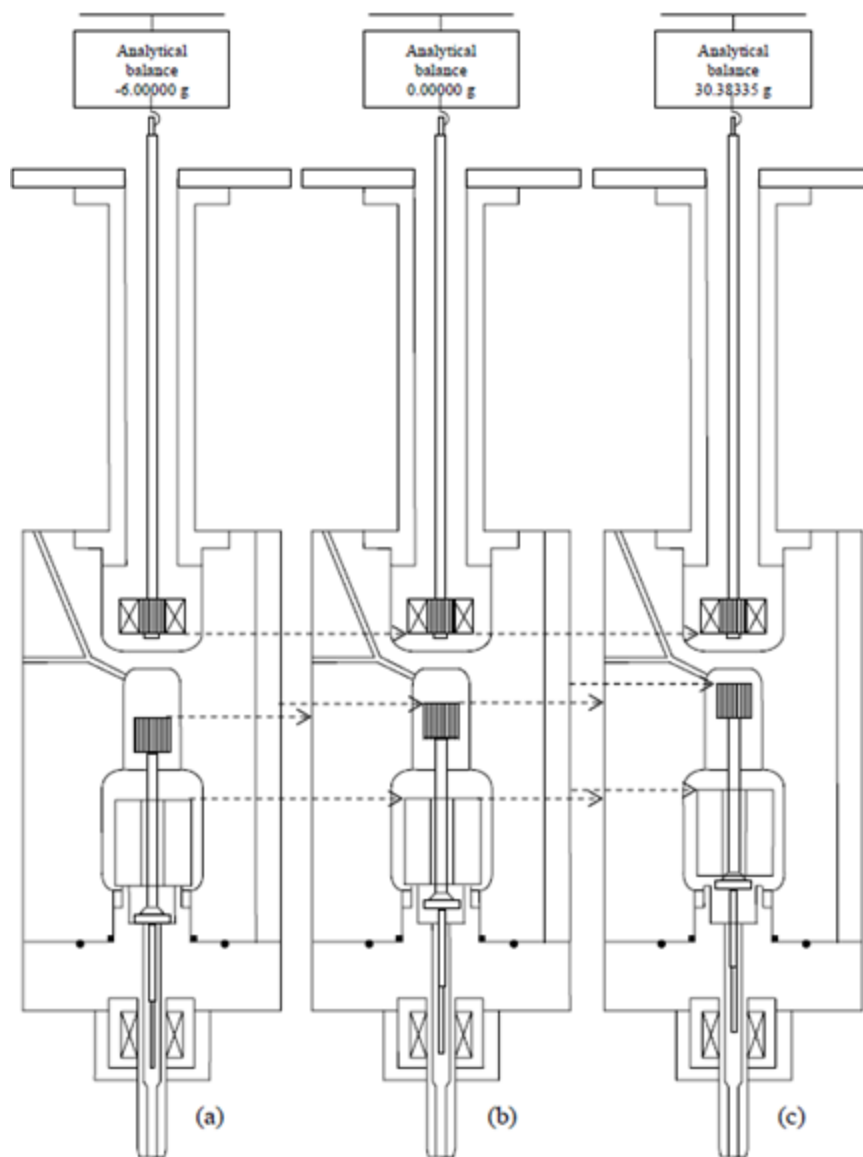


Figure 5. Overview of the TAMU MSD [22]



Operation of the MSA in Vacuum
 (a) Suspension Control 'off'
 (b) Suspension Control 'on'; Zero Point Position
 (c) Suspension Control 'on'; Measurement Point Position

Figure 6. The operations of the MSD (modified from Rubotherm Operating Instructions [39])

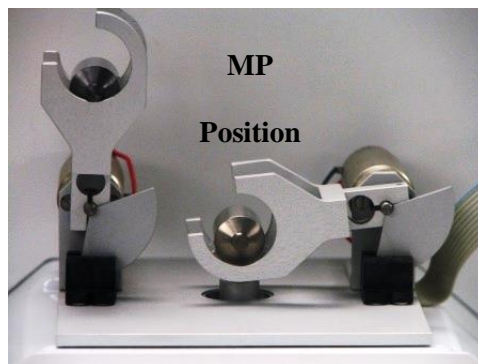
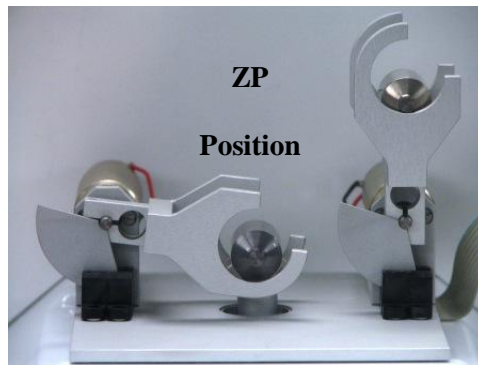
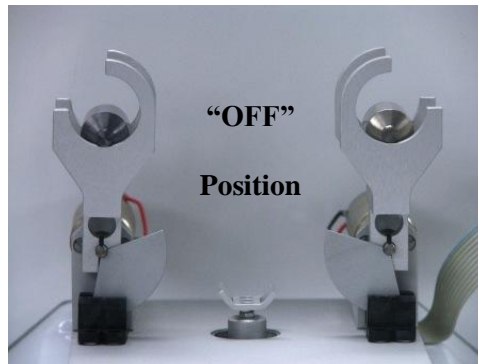


Figure 7. Weighing scheme and changing device with the Ta weight on the left and Ti weight on the right [40]

An additional point (not pictured) called the calibration point also was introduced to determine the balance calibration factor (α). The calibration point is discussed in the next section. The calibration factor typically is assumed to be 1.00015 for balances calibrated with S.S. weights.

Writing a force balance on ZP and MP leads to the following equations respectively;

$$W_{ZP} = \alpha[\phi(m_{PM} - \rho_f V_{PM}) + m_{EM} + m_{Ta} - \rho_{air}(V_{EM} + V_{Ta})] \quad (1.5)$$

$$W_{MP} = \alpha[\phi(m_{sinker} + m_{PM} - \rho_f V_{PM}) + m_{EM} + m_{Ti} - \rho_{air}(V_{EM} + V_{Ti})] \quad (1.6)$$

in which W_i is the weight read by the balance, α is the balance calibration factor, ϕ is the force transmission error and subscript f is for the fluid of interest.

Subtracting Eq 1.6 from Eq. 1.5 and solving for the fluid density yields the equation used to calculate the measured densities;

$$\rho_f = \frac{\phi m_{sinker} + (m_{Ti} - m_{Ta}) + (W_{MP} - W_{ZP}) / \alpha + \rho_{air}(V_{Ta} - V_{Ti})}{\phi V_s(T, p)} \quad (1.7)$$

To negate the buoyancy effects of the air, both the Ta weight and the Ti weight have the same volume, so the final term cancels out. The masses of the sinker and compensation weights, as calibrated by comparison with NIST calibrated external weights, are:

$$m_{sinker} = 30.39159g$$

$$m_{Ta} = 41.61804g$$

$$m_{Ti} = 11.23311g$$

The volume of the sinker was calibrated by NIST at 293.15 K and 0.1 MPa and found to be $6.74104 \pm 0.00013 \text{ cm}^3$ ($k=2$) [40]. As a function of temperature and pressure, the volume of the sinker is:

$$V_s(T, p) = V_{so}(T_o, p_o) \left[1 + 3 \left[\alpha_T (T - T_o) - \frac{p - p_o}{E(T)} (1 - 2\nu(T)) \right] \right] \quad (1.8)$$

Where α_T is the linear thermal coefficient of expansion ($8.8 \times 10^6 \text{ K}^{-1}$ over our operating temperature range of 193.15-523.15 K), E is the Young's modulus, and ν is the Poisson's ratio. Rubotherm [22, 40, 41] supplied all values.

1.1.5.4. Force transmission error for a single sinker densimeter

These errors are caused by the magnetism of the materials surrounding the system, stray magnetic fields, and the fluids. Although these effects can be reduced by careful system design, they cannot be eliminated completely. For the MSD, no “magnetic” material (defined as one attracted to a neodymium earth magnet) should be within 50 cm and no ferromagnetic material within 1 m of the permanent magnet and the electromagnet [42]. This consideration was taken into account when redesigning the system.

To maintain the accuracy of the measurements the force transmission error must be considered. McLinden *et al.* [42] developed an analysis to account for these uncertainties in which the FTE is dealt with by two different tests. In their approach, the FTE is split into two different effects, an apparatus effect and a fluid specific effect. The general empirical model to describe this is [42];

$$\phi = \phi_o + \varepsilon_p \frac{\chi_s}{\chi_{so}} \left(\frac{\rho_f}{\rho_o} \right) \quad (1.7)$$

where ϕ_o is the apparatus effect, ε_p is a fit constant for the specific apparatus and depends upon temperature and pressure, χ_s is the magnetic susceptibility of the fluid, $\rho_o=1000$ kg·m⁻³ and $\chi_{so}=10^{-8}$ m⁻³·kg⁻¹ are reducing constants. The apparatus effect is determined by a simple vacuum test ($\rho_f = 0$) as demonstrated by McLinden [42].

Cristancho *et al.* [43] have shown that for non-polar fluids in our MSD the fluid specific contribution is much smaller than the apparatus effect and hence can be neglected ($\phi = \phi_o$). Also, they determined using two different sinkers that the FTE does not depend upon temperature or pressure. These considerations along with the vacuum test leads to the FTE being calculated from:

$$\phi_o = \frac{(m_{Ta} - m_{Ti}) + (W_{ZP} - W_{MP}) / \alpha}{m_{\text{sinker}}} \quad (1.8)$$

The apparatus effect was determined to be 189±16 ppm by Cristancho *et al* [44]. Our FTE is larger than other reported values [42, 45, 46], which is to be expected because our cell requires more metal to contain the higher pressures.

After the redesign this value remained the same, however the value did shift after installation of the silicon sinker. This will be detailed more in the next section but was verified using an isotherm of nitrogen and argon with data sets matching within 0.03%.

1.2. Data sets for pure fluids and helium + methane mixtures

There have been many pure fluid density measurements for the construction of reference equations for nitrogen [47], carbon dioxide [48], argon [49], and helium [50], however, high pressure measurements are noticeably absent. Few apparatus are capable of reaching these pressures and even fewer can produce high accuracy measurements. Multiple pure components such as methane [30], ethane [31], nitrogen [32], and carbon dioxide [33] have been measured at high pressures using the TAMU MSD. In each of these cases, the respective reference equations were shown to be significantly more accurate than claimed at high pressures.

Other pure components such as helium and argon are the focus of this work because limited measurements exist at high pressures. Both are inert, spherical molecules that can be used as an inert atmosphere or as a calibration fluid. Because their densities are quite different, pairing the two components provides a safe, wide density range calibration for instruments such as high pressure vibrating tube densimeters.

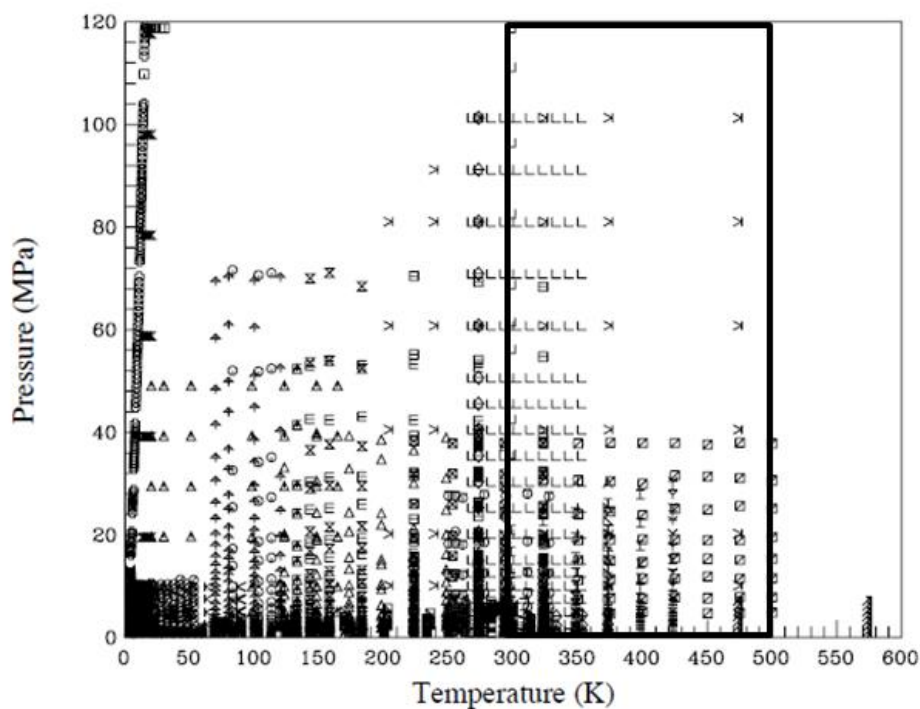
1.2.1. Argon data sets

In 1999, Tegeler *et al.* [49] provided a reference equation for argon from the melting line to 700 K up to 1000 MPa. Figure 8 depicts the compilation of the p - ρ - T data used to construct the reference equation with the rectangle representing the TAMU MSD range. The only measurements reported at pressures above 40 MPa are from Michels *et al.* [51]. Their measurements were at temperatures of 273-423 K at pressures up to 293 MPa with an estimated uncertainty in density of $\Delta\rho / \rho = \pm 0.1 - 0.15\%$. Tegeler *et al.*

used less than half of these data to build the reference equation. No other high pressure density measurements have been reported since the equation was published, although in 2005 Patil *et al.* [22] measured pure argon up to 34 MPa using the TAMU MSD with agreement with the reference equation of ($\Delta\rho / \rho = \pm 0.01\%$).

1.2.2. Helium data sets

Recently, Ortiz-Vega *et al.* [50] developed a reference equation for helium. The claimed uncertainty is $\Delta\rho / \rho = \pm 0.1\%$ at all temperatures above 200 K up to 20 MPa, and $\Delta\rho / \rho = \pm 1\%$ at pressures above 20 MPa. Figure 9 depicts the compilation of the p - ρ - T data used to construct the reference equation with the rectangle representing the TAMU MSD range. Note that the plot does not go up 200 MPa, which is our maximum pressure. Three data sets exist above 40 MPa within our operating range were reported by Blancett *et al.* [52], at pressures up to 70 MPa, Briggs [53], at pressures up to 80 MPa, and Wiebe *et al.* [54], at pressure up to 100 MPa. Only the Blancett *et al* [52] data were used in fitting the equation, with deviations within 0.02% [50]. Their data were measured in a Burnett apparatus at 323.15 K with a claimed uncertainty of 0.06% in compressibility factor for the high pressures.



- | | |
|-----------------------------|----------------------------|
| + Keesom and Walstra | × Louasmaa |
| □ Keller | ○ Miller <i>et al.</i> |
| * Kamerlingh Onnes | ◇ Hurly <i>et al.</i> |
| × Provine and Canfield | △ Tsederberg <i>et al.</i> |
| △ Tsiklis <i>et al.</i> | ▽ Tsiklis <i>et al.</i> |
| + Sullivan and Sonntag | × Suh and Storvick |
| † Stroud <i>et al.</i> | □ Nijhoff and Keesom |
| ○ Miller <i>et al.</i> | ◇ Dillard <i>et al.</i> |
| △ Roach | □ Cramer |
| ▽ Kamerlingh Onnes and Boks | ∇ White <i>et al.</i> |
| × Buchmann | □ McLinden |
| □ McLinden | ⊙ Louasmaa and Kaunisto |
| ○ Kamus | * El Hadi and Durieux |
| □ Glassford and Smith | ∓ Michels |
| □ Blancett <i>et al.</i> | ⊙ Brandt <i>et al.</i> |
| ◇ Briggs <i>et al.</i> | ∓ Briggs |
| □ Brown <i>et al.</i> | △ Canfield <i>et al.</i> |
| □ Canfield <i>et al.</i> | × Edeskuty and Sherman |
| ▽ Edwards and Woodbury | ▽ Edwards and Woodbury |
| ∧ El Hadi <i>et al.</i> | ∗ Evers <i>et al.</i> |
| ∇ GERG TM4 | ∓ Grilly and Mills |
| □ Grilly and Mills | ○ Hall and Canfield |
| ◇ Hamann and McManamey | ▽ Hill and Louasmaa |
| □ Jaeschke and Humphreys | ∧ Linshits <i>et al.</i> |
| ∓ Nathan | × Nijhoff <i>et al.</i> |
| □ Oguchi <i>et al.</i> | ⊙ Vogl and Hall |
| □ Vogl and Hall | ◇ Weems and Howard |
| ∓ Weems and Miller | × Wiebe <i>et al.</i> |

Figure 9. Distribution in pressure and temperature of the experimental data used to develop the helium reference EoS [50]

1.2.3. Helium + methane data sets

As seen in the above sections, there is a need for high-accuracy measurements on pure fluids, but the need is even greater in the case of mixtures, which have more practical applications. Mixture data can provide insight into molecular interactions, leading to better mixing and combining rules, and improved mixture predictions.

In 2016, Hernández-Gómez *et al* [55, 56] measured three methane + helium mixtures, with methane mole fractions of 0.95, 0.90 and 0.50, using a single-sinker MSD at temperatures of 250-400 K up to 20 MPa. Their claimed uncertainty ranges from 0.04% in density at the higher pressure, 1.0% in density at low pressures. These data deviated significantly, up to 6.0 %, in density compared to GERG 2008 [57] while being an order-of-magnitude better compared to AGA8-DC92 [58]. These appear to be the only density data available within our apparatus capabilities.

1.3. Fundamental equations of state and current reference equations

While p - ρ - T data are essential to build thermodynamic models, these models also must predict accurately other thermophysical properties, such as energies, that are important in process design. Because these energies cannot be measured directly, densities along with other data, such as speed of sound and calorific properties measurements, are required to accurately predict the fluid behavior.

Many equations of state have been proposed in the form of pressure as a function of temperature and density such as the commonly used cubic equations of state suggested by Soave [59] and Peng and Robinson [60]. These are relatively simple mathematical

models and can describe fluid behavior well for most process models as long as the conditions are within the data used to fit the model and removed from the fluid critical point. The inability to extrapolate limits the applicability of the cubic equations. Another disadvantage is that integration is required to calculate properties such as energies and entropies, which are important for process modeling. Integration causes numerical issues that do not occur for derivatives. Because of this numerical advantage, it is better to start with an equation that only requires differentiation to get to all other properties.

Fundamental equations describing Gibbs energy, Helmholtz energy, internal energy, and enthalpy have this ability. When choosing which equation to use, it is important to have observable independent variables, leading to the choice between Gibbs and Helmholtz energies. Although the Gibbs energy is used directly in phase equilibrium calculations and has convenient independent variables of pressure and temperature, it provides challenges when trying to create a mathematical model. These problems do not exist with the Helmholtz energy, which is a function of temperature and density. Typically, the variables are made dimensionless to remove any potential issues with units.

The first equation to be formulated in dimensionless Helmholtz energy was created by Keenan *et al.* [61] for water. It was written in the residual form as shown below;

$$\alpha(\rho, T) = \alpha^{IG}(\rho, T) + \alpha^r(\rho, T) \quad (1.9)$$

Multiple other equations were built of similar form and even introduced reducing parameters [62, 63]. The modern functional form for most reference equations was first developed by Schmidt and Wagner [64] for oxygen and further developed by Span and Wagner [48]. These models also use the form;

$$\alpha(\delta, \tau) = \alpha^{IG}(\delta, \tau) + \alpha^r(\delta, \tau) \quad (1.10)$$

in which

$$\tau = \frac{T_c}{T}$$

$$\delta = \frac{\rho}{\rho_c}$$

and the subscript c denotes the value at the critical point.

The ideal part is calculated from the ideal gas law and the ideal gas heat capacity while the residual term is an empirical model defined as;

$$\begin{aligned} \alpha^r(\delta, \tau) = & \sum_{k=1}^{I_{pol}} N_k \delta^{dk} \tau^{tk} + \sum_{k=I_{pol}+1}^{I_{pol}+I_{exp}} N_k \delta^{dk} \tau^{tk} \exp(-\delta^{dk}) \\ & + \sum_{k=I_{pol}+I_{exp}+1}^{I_{pol}+I_{exp}+I_{crit}} N_k \delta^{dk} \tau^{tk} \exp(-\eta_k (\delta - \varepsilon_k)^2 - \beta_k (\tau - \gamma_k)^2) \end{aligned} \quad (1.11)$$

The residual term is broken down into three different terms; a polynomial, polynomial with exponential, and Gaussian bell, which helps with the fit of critical region. These equations have incredible predictive capabilities, even outside the range where data is present. This model has been successfully applied to many pure fluids such as helium [50], nitrogen [47], and argon [49].

Expanding the concept of dimensionless Helmholtz energy defined by an ideal and residual part to mixtures, Kunz *et al* [65] introduced GERG in 2004 and Kunz and Wagner [57] further improved on the mixture model in 2008. This model contains 21 natural gas-like components and their mixtures. More details about the model and its mixing rules are described in section 4.

The equation has shown predictive capabilities describing methane rich mixtures within $Dr/r = \pm 0.25\%$ up to pressures of 150 MPa [34, 35, 66]. However, these models are fairly complex (over 50 parameters needed for methane + ethane interactions) and require a large amount of computational time making it difficult to apply in process design.

Recently, Gomez-Osorio *et al.* [20] proposed a new model for the residual Helmholtz energy for pure fluids based upon a polynomial (rational) form that addresses these issues with only a slight or even no decrease in accuracy. This work extends this model to describe interactions between unlike molecules and provide a basis to build new mixing rules.

1.4. Objectives

The objectives of this work fall into the following categories:

1. Redesign of the TAMU MSD for more stable measurements at temperatures up to 500 K. This includes installation of a high vacuum system able to reach pressures of the order of 10^{-5} Torr.
2. Implementation of a new measurement sequence, improving the rate at which data can be collected.
3. Calibration of a silicon sinker for use in density measurements and expose limitations of MSD when using this sinker.
4. Measurements of pure argon, pure helium, and a mixture of helium + methane at pressures up to 200 MPa.

5. Develop mixing rules based upon residual Helmholtz energy for multiple mixtures.

Section 2 describes the redesign of the MSD, along with the new measurement sequence. A silicon sinker calibration is also presented in the section.

Section 3 presents the experimental measurements of pure nitrogen, helium, and argon. Preparations of helium + methane mixtures are discussed along with experimental measurements at temperatures of 303-450 K at pressures up to 200 MPa. Experimental uncertainty of the measurements is also discussed.

Section 4 proposes a basis for new mixing rules. The form uses a rational polynomial to describe the interaction Helmholtz energy. This is applied to eleven binary mixtures.

2. SINGLE SINKER MAGNETIC SUSPENSION DENSIMETER APPARATUS

Originally, the supporting systems for the MSD consisted of two balance plates, a standard platinum resistance thermometer (SPRT), a 40 MPa pressure transducer, and a temperature jacket fed by a temperature bath surrounding the cell [22]. The upper temperature limit of the heating bath was 473 K, although heat transfer constrained the maximum measuring temperature to 450 K.

Next, a 200 MPa transducer was added into the system [41] followed by a redesign of the temperature system [40] using an inner shield and outer shield instead of a jacket. Dow-Corning 550 DC-550 phenyl methyl siloxane oil was the heating fluid.

Resistive heating tape was added to help improve the control of the shield temperatures. Even with these upgrades the SPRT oscillated more than 20 mK in the upper temperature range because the fluid lines were exposed to ambient conditions. An overview of the previous system is presented in Figure 10.

This section focuses upon the modification of the existing MSD to achieve a wider temperature range and increase the stability of the SPRT measurements. Additionally, the measurement process is improved by changing the measurement sequence and the leveling and alignment systems. The apparatus includes electrical heaters, a temperature control system, a high vacuum system, a leveling system, a compression system, and a data acquisition system. Finally, measurements for a well-known fluid (nitrogen) were used to verify the accuracy of the new design. Figure 11 gives an overview of the redesigned system.

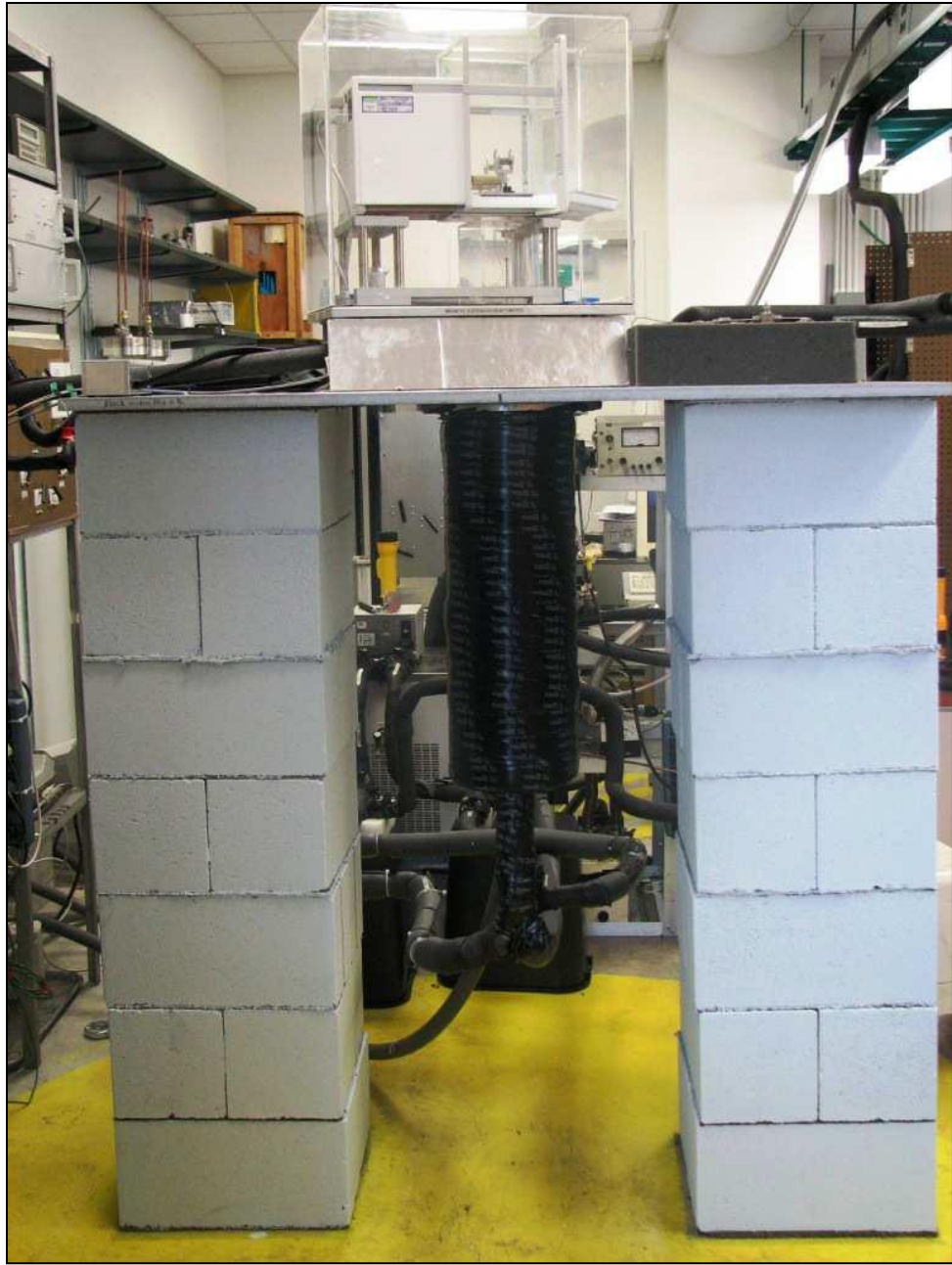


Figure 10. Previous MSD design [40]



Figure 11. MSD after the completed redesign

2.1. Apparatus description

2.1.1. High pressure measurement cell and balance

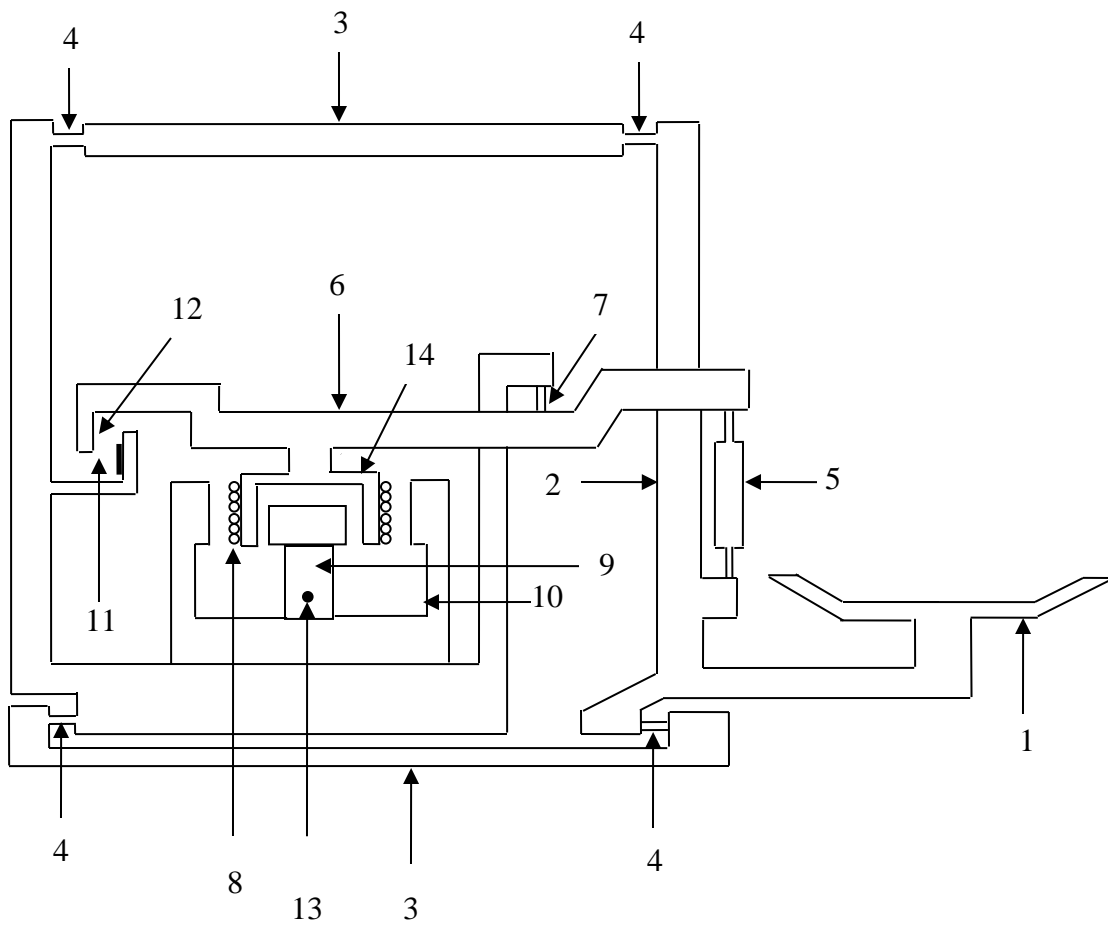
The MSD consists of the measuring cell, weighing balance, suspension and coupling system. Rubotherm Präzisionsmesstechnik GmbH in Germany manufactured the MSD cell, suspension and coupling system. The cell material is an unspecified alloy of beryllium copper that provides both good mechanical strength and high thermal conductivity. The maximum operating pressure of the cell is 200 MPa and it was hydrostatically pressure tested at 300 MPa by Rubotherm. Connecting the cell and balance is a circular stainless steel tube referred to as the electromagnet (EM) shaft that houses the EM. This shaft is bolted to bottom side of the balance plate using 6 ¼"-20 bolts and sealed with a PTFE round #120 O-ring (OD-1.193", ID 0.987", H- 0.100").

No standard sized O-ring exists for sealing around the bottom of electromagnet tube so a polyimide seal (Vespel® SP-1, 1.229" O.D. 0.989" I.D. 0.125" H) was created to withstand the higher temperature limits (500 K). Since Vespel® SP-1 has a small thermal expansion coefficient, copper back up rings (1.318" O.D. 1.230" I.D. 0.125" H) were also created. Copper matches the thermal expansion of the cell (CuBe) and ensures the integrity of the vacuum insulation. Both pieces were fabricated in the machine shop located in the Texas A&M Department of Chemistry. The design detail appears in Appendix A. Socket head cap screws securing the EM shaft to the cell (M4 L-10 mm, believed to be constructed of 303 S.S.) were replaced by titanium screws to decrease possible magnetic interactions.

The inlet at the top of the cell was plugged using a custom machined High Pressure Equipment Company (HiP) ¼” plug to reduce the dead volume and the total number of lines in the vacuum chamber.

At the bottom of the cell, a 316 S.S. flange that houses the position sensor used in the control system is attached to the cell using 10 mm threaded rods and nuts. Seals between the flange and cell (ID- 0.706”, OD- 0.775”, H-0.039”) are also Vespel® SP-1 to withstand the highest operating temperatures. The seals were fabricated in the machine shop located in the Texas A&M Department of Physics. A design drawing appears in Appendix B. The flange is tightened to 25 ft·lbf to create an adequate seal.

The balance (Mettler Toledo, model AT 261 serial no. 1117062570) has two ranges, 0-62 g and 0-200 g, with resolutions of 0.01 mg and 0.1 mg respectively. The shorter range of 0-62 g is used throughout our experiment to obtain the highest accuracy. A cross section of the balance appears in Figure 12 while an overview of both the balance and cell appears in Figure 13.



- | | |
|--|--|
| 1 Weighing Pan | 9 Permanent magnet of electrodynamic converter |
| 2 Hanger | 10 Magnetic circuit |
| 3 Guide of the parallel-motion mechanism | 11 Position sensor |
| 4 Flexible bearing | 12 Position indicator |
| 5 Link | 13 Sensor for temperature compensation |
| 6 Lever to transmit weight force | 14 Coil support |
| 7 Suspension of lever | |
| 8 Compensation coil | |

Figure 12. Cross section of weighing balance from Mettler Toledo [67]

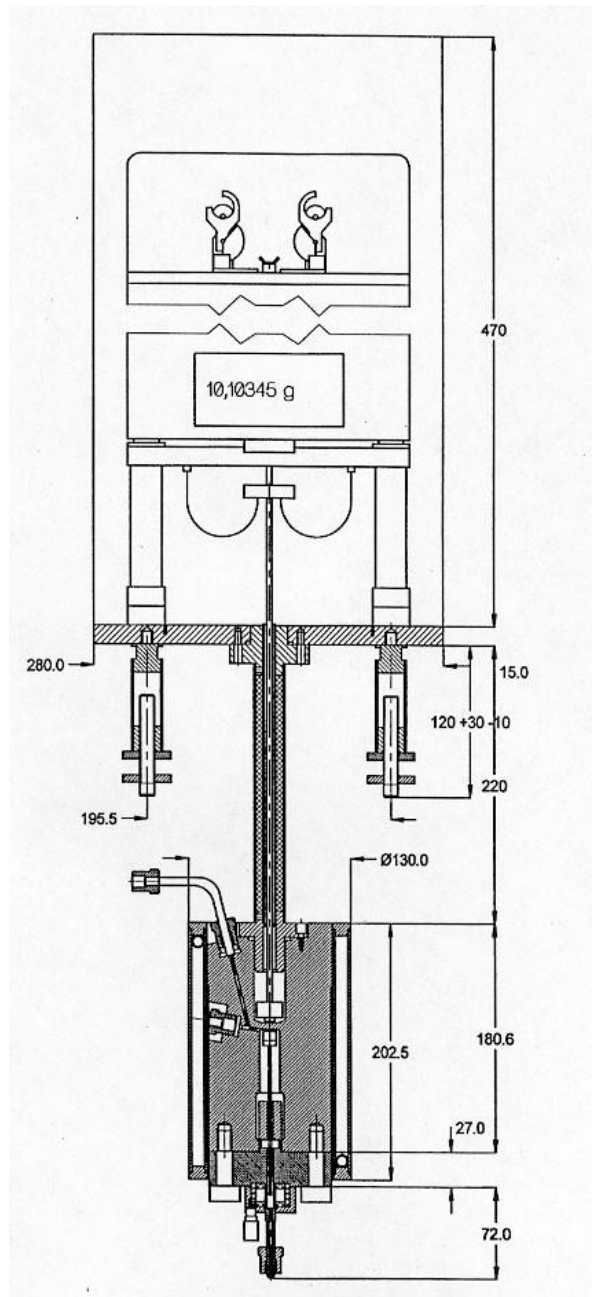


Figure 13. Overview of the MSD and dimensions in mm [39]

Because of the weighing balances non-linearity as values move away from zero, two compensation weights made of tantalum and titanium and a weight-changing device are necessary. These two materials were selected and constructed along with the sinker (titanium in our case) so that measurement values would be approximately zero [68]. Also, the weights are approximately the same volume ($\sim 4.29 \text{ cm}^3$) so air buoyancy effects are negligible. The tantalum and titanium weights have masses of approximately 40 g and 10 g and densities of $16.7 \text{ g}\cdot\text{cm}^{-3}$ and $4.5 \text{ g}\cdot\text{cm}^{-3}$ respectively.

The entire balance setup is encased in an acrylic box with various feed-throughs and is sealed to the balance plate using foam strips. This enclosure protect against sudden atmospheric changes that could cause instabilities in the mass measurements. A continuous feed of industrial grade nitrogen to the enclosure through a purge line prevents humid air from entering and purges moisture. Electrical feed-throughs were created by altering the original balance plate supplied by Rubotherm and sealing the plate to the acrylic box using #6-32 screws and foam lining. An image of this feed-through system can be seen in Figure 14. To further prevent instabilities, another acrylic box is placed around the EM [40].

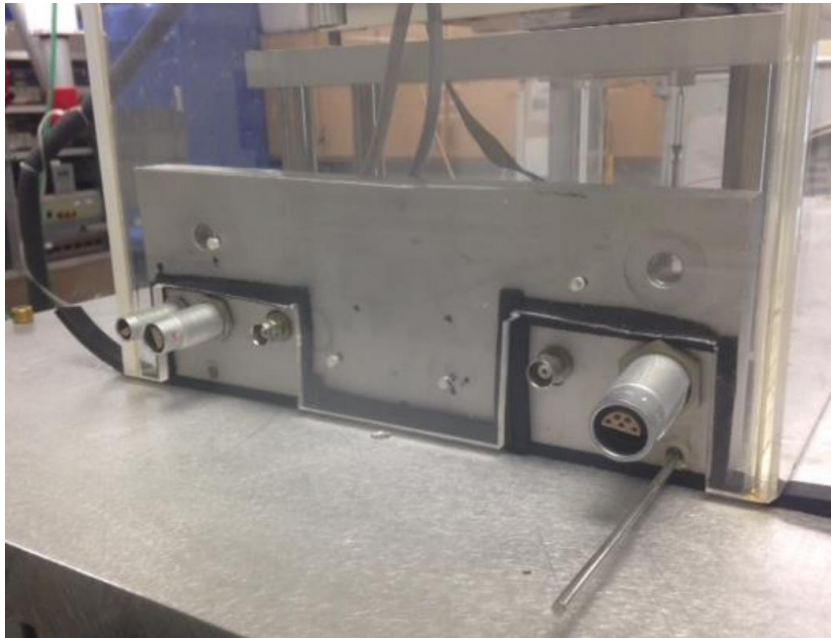


Figure 14. Electrical feed-through to the balance

2.1.2. Suspension and coupling system

The suspension and coupling system consists of a control box, an electromagnet (EM), a permanent magnet (PM) made from samarium cobalt, and a position sensor that suspends and controls levitation of the sinker. The EM, which has a soft iron core, hangs from a hook at the bottom of the balance and feeds up through the EM shaft. Leads from the EM feed out through the top and are plugged into sockets that lead back to the control box using BNC connectors. The output from the position sensor inside the cell feeds into a position sensor box (pictured in Figure 15) that leads back into the control box. To suspend the PM, the control box energizes the EM so the PM becomes “attracted” to it and rises. The amount of current is determined by the position detected by the position sensor, the desired measurement point, and a proprietary fast loop PID controller [68]. More details on the levitation and control appear in [22, 41].

Because the suspension and control system is sensitive to temperature changes within the apparatus, adjustments to the control system must be made to obtain stable measurements after changing temperature. In the “OFF” position, the U_a voltage, which corresponds to the position sensor inside the cell, should read ~ 5.6 V. If not, the adjustable resistors in position sensor box may be adjusted using the brass screws as seen in Figure 15 until this voltage is reached. This method replaces the previous temperature compensation box installed by Athilan [40]. It provides an advantage in that the expected voltage is known (5.4-5.6 V), hence the trial and error approach used previously is not required.

Another issue encountered with the control and suspension system occurs when removing and/or installing a sinker. When the PM is moved from the position sensor well, the computer control on the control box resets and does not suspend the PM again until it is reset. To test if this has occurred, the U_s voltage, which has a value of $-U_a$ (-5.6 V) in the “OFF” position, should be read using the black and red terminals and dial on the back of the control box. When the error occurs this value is ~ -14 V. To fix this issue a hard reset is necessary by unplugging the computer control lead at the back of the control box. If this does not work a hard reset of the control box is necessary. For additional details on other normal voltage readings, values are presented in the Rubotherm manual [39] and in Appendix C. Using these values are good starting points to help identify the possible issues.

2.1.3. Mounting and alignment system

For mass measurement stability and accuracy, alignment of the system is crucial. In the redesign, the balance was removed from the balance plate and mounted on a plate along with the rest of the system, thereby eliminating one of the extra surfaces making alignment simpler.

The new aluminum support plate (3' long x 2' wide x 1" thick) is mounted by three 5/16" brass screws to an aluminum strut frame (5' tall x 2' wide) that has vibration damping leveling feet. Aluminum was chosen because its small magnetic susceptibility does not disrupt the mass measurements/ suspension. A level with sensitivity of 0.0004 cm/m is installed close to the electromagnet to ensure this region is level.

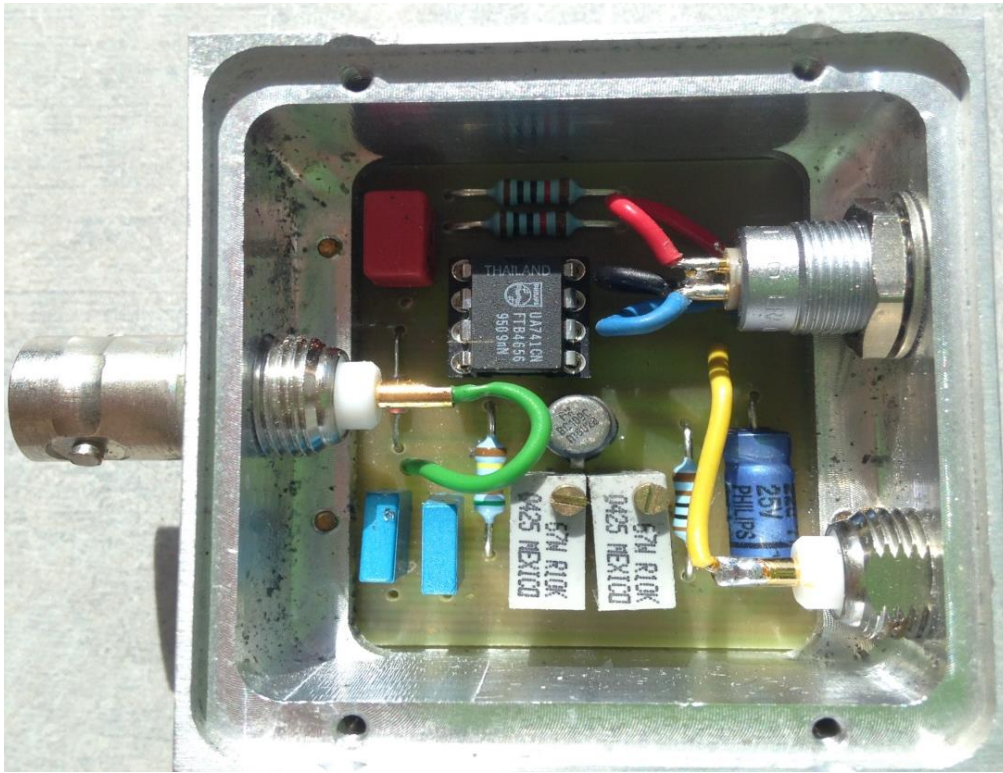


Figure 15. Position sensor box

Additionally, the pressure transducers, pressure relief devices, feed lines, electrical terminal boxes for the heaters, and thermometry leads are now housed on the balance plate to cut down on the amount of lines and leads that are exposed to ambient conditions. A plastic electrical raceway with multiple slots was mounted on the balance plate to allow for the separation of the high current leads (heater) and low voltage leads (thermometry) to reduce any possible interference.

2.1.3.1. Horizontal and vertical alignment of the electromagnet

Once the support plate is level, the alignment between the EM and PM must be adjusted. There are two components to this alignment, vertical (distance between the PM and EM) and horizontal placement of the EM within the shaft. Improper alignment could cause the sinker or EM to touch the wall, the suspension system to be unable to lift the sinker, or the PM to stick to the top of the cell, resulting in unstable or incorrect measurements.

For vertical alignment, 2 full turns up from bottom of the EM is the optimal height and has been confirmed by other authors as well [22, 40, 41]. To determine the bottom, the EM is lowered until the balance display shows dashes. Once at the desired height, the EM is locked in position using a lock nut.

After vertical alignment, horizontal alignment is achieved by moving the balance and checking the stability of all the measurement positions, “OFF”, ZP and MP in that order. The system is considered stable if the standard deviation of the measurement is within ± 0.05 mg over 3 minutes, which is expected during a single measurement cycle.

During these test, temperature stability within the system is necessary. Different possible causes of unstable measurements depend upon the measurement position.

For an unstable “OFF” position, the typical causes are unaligned balance, ambient or system condition changing or EM touching the shaft wall. An unstable ZP is potentially caused by either improper alignment between the PM and EM or possible signal interference, which is observed by spikes in the measurements. This interference occurs when the power to the suspension system is connected to the same outlet as the high current devices (the heaters). If the system is stable in the “OFF” and ZP position but not MP, then the cause is the sinker contacting the wall of the cell when being lifted. In this case, further horizontal alignment is required.

A horizontal alignment slightly to the left and back from a front view of the balance was optimal. This could be caused by the EM shaft not being completely straight as determined in the past from tests performed by the chemical engineering machine shop. Additionally, new supports are directly attached to the EM shaft and cell possibly pulling the parts askew. Figure 16 depicts the typical alignment of the EM for our measurements.

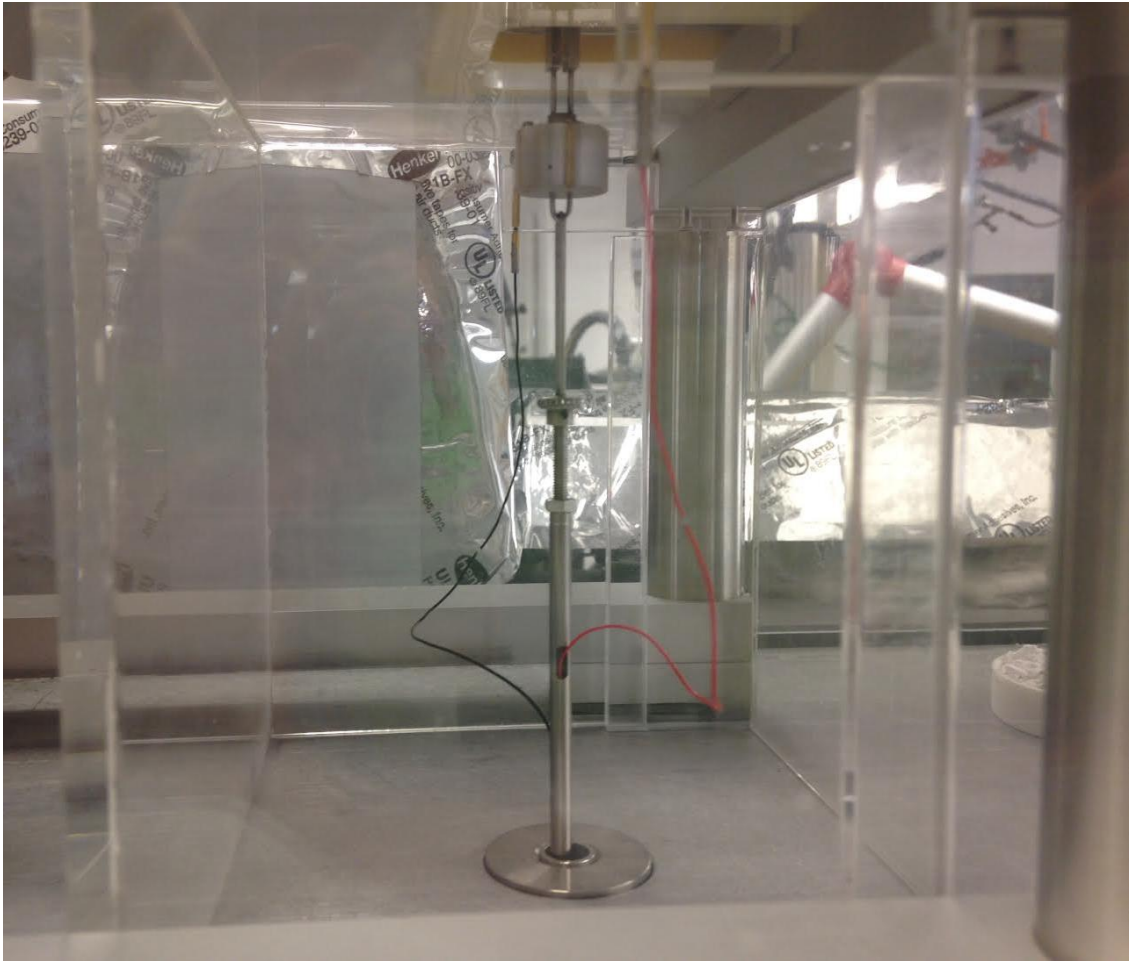


Figure 16. Electromagnet (EM) hanging from the balance

2.1.4. Measurement sequence

Another improvement to the system is a new measurement procedure. Previously, only the zero point (ZP), which includes the tantalum weight and the permanent magnet without the sinker, and the measurement point (MP), which includes the titanium weight along with the permanent magnet and sinker, were measured. With these two measurements the density of the fluid and the FTE can be determined, but only after assuming a balance calibration factor (α) that accounts for the balance effect. A typical value of $\alpha=1.00015$ as stated for a two sinker magnetic suspension densimeter has been used in the past [22, 40, 44].

The new sequence adds an additional measurement, called the calibration point (CP) that includes the titanium weight and the permanent magnet. The force balance for the CP and ZP yields:

$$ZP - W_{Ta} = \alpha \left[\phi \left(m_{PM} - \rho_f V_{PM} \right) + m_{EM} + m_{Ta} - \rho_{N_2} \left(V_{PM} - V_{Ta} \right) \right] \quad (2.1)$$

$$CP - W_{Ti} = \alpha \left[\phi \left(m_{PM} - \rho_f V_{PM} \right) + m_{EM} + m_{Ti} - \rho_{N_2} \left(V_{PM} - V_{Ti} \right) \right] \quad (2.2)$$

Subtracting 2.1 from 2.2 yields,

$$W_{Ta} - W_{Ti} = \alpha \left[m_{Ta} - m_{Ti} - \rho_{N_2} \left(V_{Ti} - V_{Ta} \right) \right] \quad (2.3)$$

Rearranging and solving for α with $V_{Ti} \approx V_{Ta}$

$$\alpha = \frac{W_{Ta} - W_{Ti}}{m_{Ta} - m_{Ti}} \quad (2.4)$$

Our measurement sequence follows the proposal of McLinden [29];

1. Zero Point

2. Measurement Point
3. Calibration Point
4. Repeat steps 2-3 for a predetermined number of cycles (typically 5)
5. Zero Point

The measurement time for each point is symmetric and found to be optimal at one minute per cycle with a minute and a half for stabilization time (delay time). The modified procedure reduces measurement time considerably, from an hour and twenty minutes previously to only about forty-five minutes, while also enabling us to account for drift in the balance by means of the balance effect for each cycle. Alpha values between 1.00010-1.00016 have been observed, typically varying with changes in the room conditions.

2.1.5. Temperature measurement

The primary temperature measurement utilizes a Minco® four-lead standard platinum resistance thermometer (SPRT model S1059-2, serial number 204) with a working range of 84.15 to 533.15 K. Temperature sensitivity is reported at 0.3925 $\Omega/^{\circ}\text{C}$ [40]. The SPRT was placed into a hole in a copper block that is attached to the groove along the side of the cell [22]. The original SPRT leads were extended using AWG 28 polyimide coated copper lead (MWS wire industries heavy polyimide). Mechanical connections between the leads were made by crimping thin-walled copper tubing etched in acid. A protective coating of solder (60/40 Sn/Pb) was added onto the copper tubing to minimize oxidization, and heat shrink tubing was added to provide electrical insulation

for the junctions. Resistance measurements before and after the addition of the connector verified that no significant changes resulted from the extensions.

Each shield and support temperature is measured using surface mount 4 wire 100 Ω resistance temperature detectors, (RTD, OMEGA[®] Model SA1-RTD-4W). Measurements were read and controlled using a PID controller from LabVIEW 2012.

The thermopile, which measures the vertical temperature gradient of the high pressure cell by the Seebeck effect (voltage differences), also was modified slightly from the previous setup [40] in that twelve nodes of AWG 28 copper wire/AWG 30 copper constantan thermocouples were made instead of the previous five nodes. Junctions were covered with Resbond[™] 920, a thermally conductive and electrically resistant adhesive compound to protect against shortages. An image of the thermopile can be seen in Figure 17.

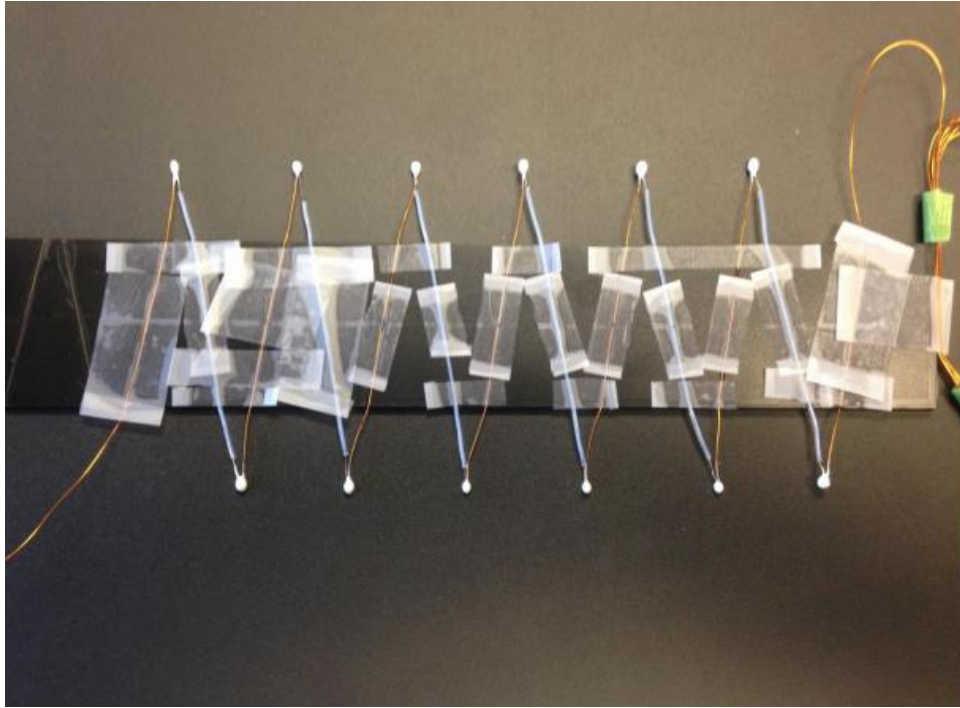


Figure 17. New thermopile

A new electrical terminal box was created to house all thermometry lead connections and the standard resistors. This box is presented in Figure 18. It is mounted directly to the balance plate reducing the lead length exposed to the ambient conditions. This lowers the potential for thermal EMF in the measurements as well as minimizing interference from external electrical signals. Gold-plated terminals were used inside the box as well as the lead tips of the SPRT were tinned with solder (60/40 Sn/Pb) to protect against oxidation. Oxidized leads caused slightly higher deviations in the previous SPRT measurements (~5-10 mK), making this a necessary step. A similar but separate box was created for the heaters to reduce any potential interaction between high voltage and low voltage signals.

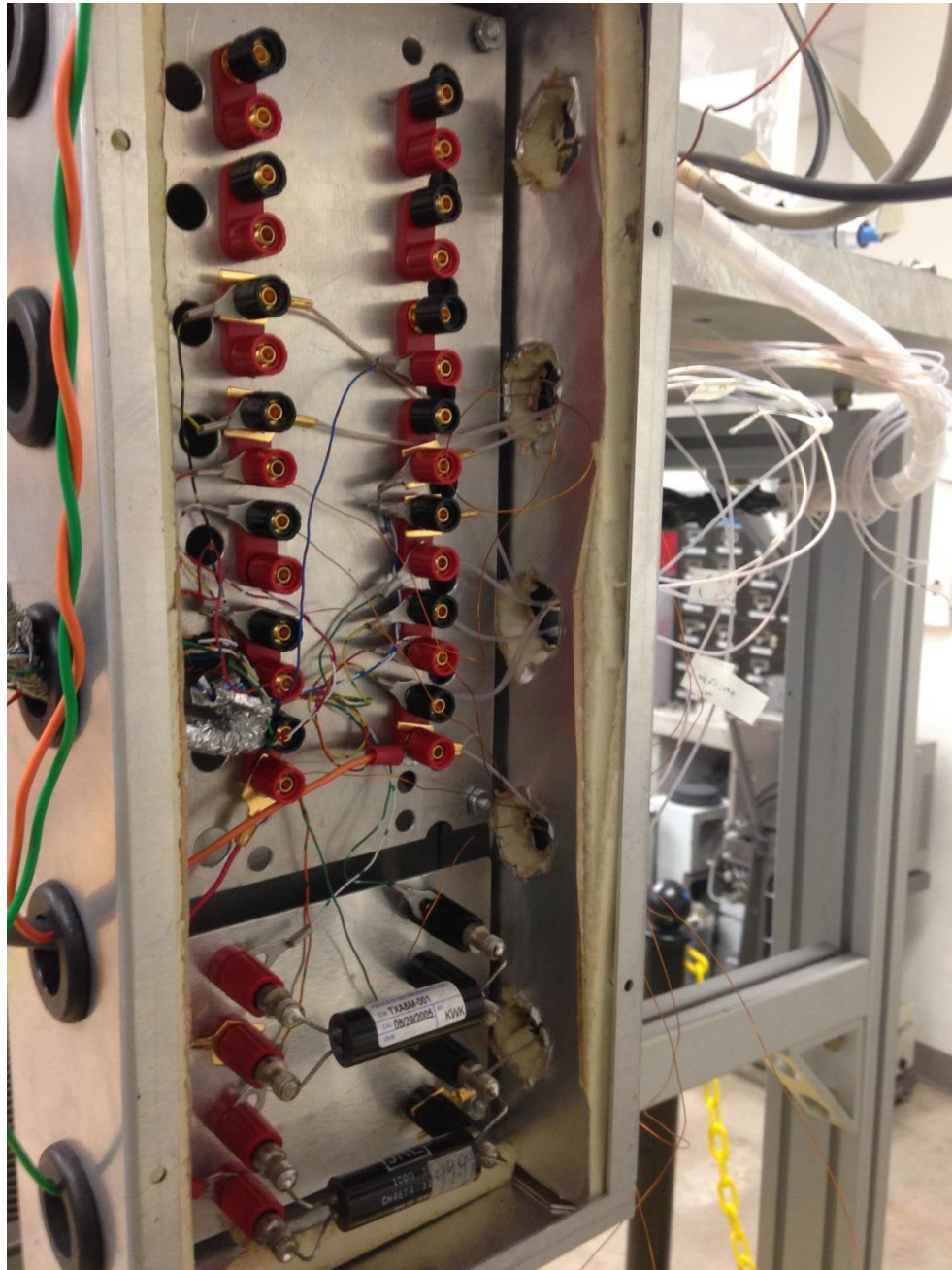


Figure 18. Electrical terminal box for the thermometry leads

2.1.6. Heaters and heating shields

A new heating system was constructed to eliminate limitations and effects present in the previous system that used a heated fluid bath [40]. An electrical heating system was chosen to improve isolation from ambient conditions.

Electrical heaters were constructed of 26-28 AWG NI80 OMEGA[®] heating wire, rated to 1033 K and OMEGATITE[®] 350 ceramic insulators with two holes. The wire is fed through the insulator in a U shape to reduce the electromagnetic effect produced when current passes through the wire. Leads connecting to the heater wire are made of polyimide coated copper wire (MWS wire industries Heavy polyimide 18 AWG) and are crimped together using either a tin copper butt splice or bare copper tubing. Heat shrink tubing is then applied to the joints to provide electrical isolation. Figure 19 depicts a typical heater without the external leads.

The maximum voltage supplied to each heater is adjusted using a variable AC power supply with a maximum voltage output of 140 V. The voltage values vary for different shields and set point temperatures. The operating conditions all were determined from operating experience.

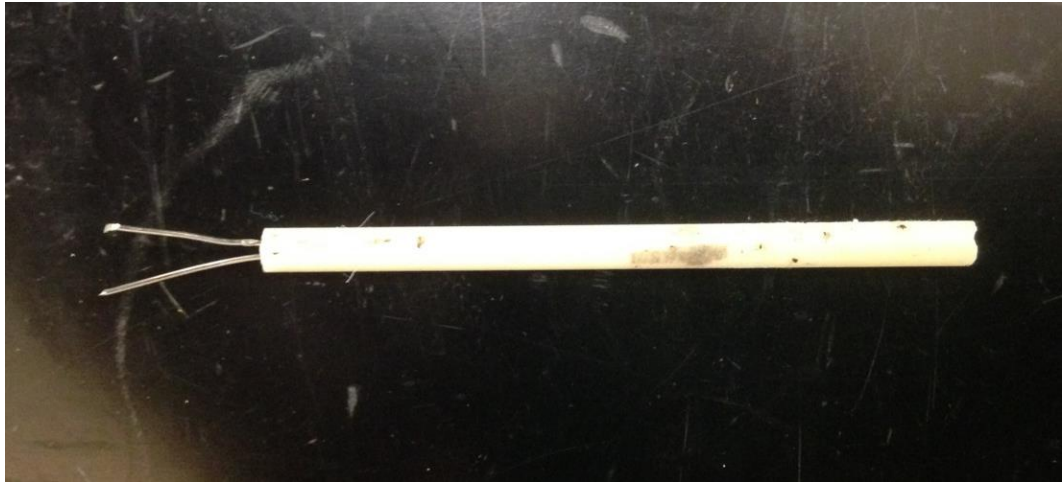


Figure 19. Example of a typical electrical heater that was used for the shield supports

Two new shields, constructed of 6" (inner shield) and 8" (outer shield) aluminum pipe, replaced the previous shields. Aluminum was chosen because of its relatively high thermal conductivity and availability. Each shield has vertical 3/32" channels engraved on the sides for the heaters along with aluminum shims and brass #6/32" screws to hold the heaters in place. Four heaters are placed on the inner shield while six heaters are on the outer shield. The inner shield has a 7/8" slit cut out of it along with tabs on each side of the slit. 1/4"-20 bronze screws passing through both sides of the tab and allow for tighten of the shield. An aluminum shim bridges the rest of the gap to maintain a uniform temperature. An aluminum 6" disk is welded to the bottom of the shield for closure. Figure 20 depicts the inner shield. A more detailed drawing appears in Appendix D Figure D.1

This shield is clamped onto a support that is clamped around the cell to create a direct conduction path. Also, vertical gradients are reduced without a direct connection to the balance plate. The cell heater support is a 6" O.D. aluminum disk with a machined 99 mm I.D. (the outer diameter of the top of the cell). The support is cut in half and two 5/16" brass screws tighten it together around the cell.

The upper end of the outer shield has six slots, cut to form tabs with 1/4" holes to provide firm physical contact when the shield is attached to the support. The bottom of the outer shield is held in place by three #6/32 brass screws. Figure 21 presents an image of the outer shield.



Figure 20. Inner Shield



Figure 21. Outer Shield

The outer shield support is constructed from an 8" aluminum disk and is suspended from the bottom of the balance plate using custom connectors. These connectors are built of a thin walled 1/4" stainless steel tube with 1/4" threaded brass stubs brazed into each end of the tube. The brass stubs have left-hand threads on the bottom of the support and right-hand threads for the connection to the balance plate. A hole in the tube wall allows for vacuum equilibration.

A clamp bolted to the top of the outer shield support provides a thermal anchor for the EM to minimize thermal gradients along the EM tube and is show in Figure 22. Other thermal anchors for the thermometer leads (a 1/2" threaded aluminum rod and 1/2" brass nuts) and fluid lines (called bulkheads) for both the cooling and feed lines are also installed on the support. Their purpose is to minimize thermal gradients with the system as well as to reduce the effects of thermal EMF's. Sketches of the outer shield and support appear in Appendix D Figure.D.2-5.



Figure 22. Outer shield support attached to EM clamp

Radiation shields are included between the outer shield and the external wall of the vacuum chamber to reduce radiative heat loss at higher temperatures. The lower radiation shield is composed of aluminum foil sheets (H~18" and 0.015" thick) and fiber glass sheet. The sheets are laid on top of each other and then one end of the aluminum sheet bolted to a 14" O.D. aluminum ring. The two sheets are then wrapped around the circumference of the aluminum ring three times. The fiber glass sheet causes separation between the foil layers making multiple floating shields, which are effective in reducing radiative heat effects. Ceramic spacers are inserted between each foil layer at the bolted joints to ensure separation of the foil layers around the ring. Three slightly larger ceramic spacers of ~1" long are bolted to the aluminum ring and rest on the bottom of the vacuum chamber. Aluminum 14"O.D. foil circles were bolted to the aluminum ring to reduce the vertical temperature gradient effects. An image of this radiation shield is shown in Figure 23.



Figure 23. Lower radiation shield

The upper radiation shield minimizes radiative heat transfer between the top support plate and the outer shield support. This shield is constructed of two aluminum rings (14" O.D. x 13" I.D. x 0.125" long) welded onto the outer diameter of another aluminum ring (14" O.D. x 0.50" long x 0.125" thick) creating a small lip similar to a rolled piece of angle iron. Two 5" long pieces of aluminum foil sheets are wrapped around the I.D. and O.D. of these rings and bolted onto the ring using #6-32 x 1/4" brass screws. This creates two separate layers, helping reduce the radiative heat loss at high temperatures. Two aluminum rings are bolted onto the top and bottom of each ring to create vertical shields as well. Multiple cut outs for instrumentation were made on the various shields. Three #6-32 x 1 1/2" brass screws are bolted onto tabs on the top ring and the bottom side of the balance plate, suspending the ring. A rough sketch and picture of the upper radiation shield are shown in Figures 24 and 25. More detailed drawings of both of the upper and lower shields appear in Appendix D Figure D.6-9

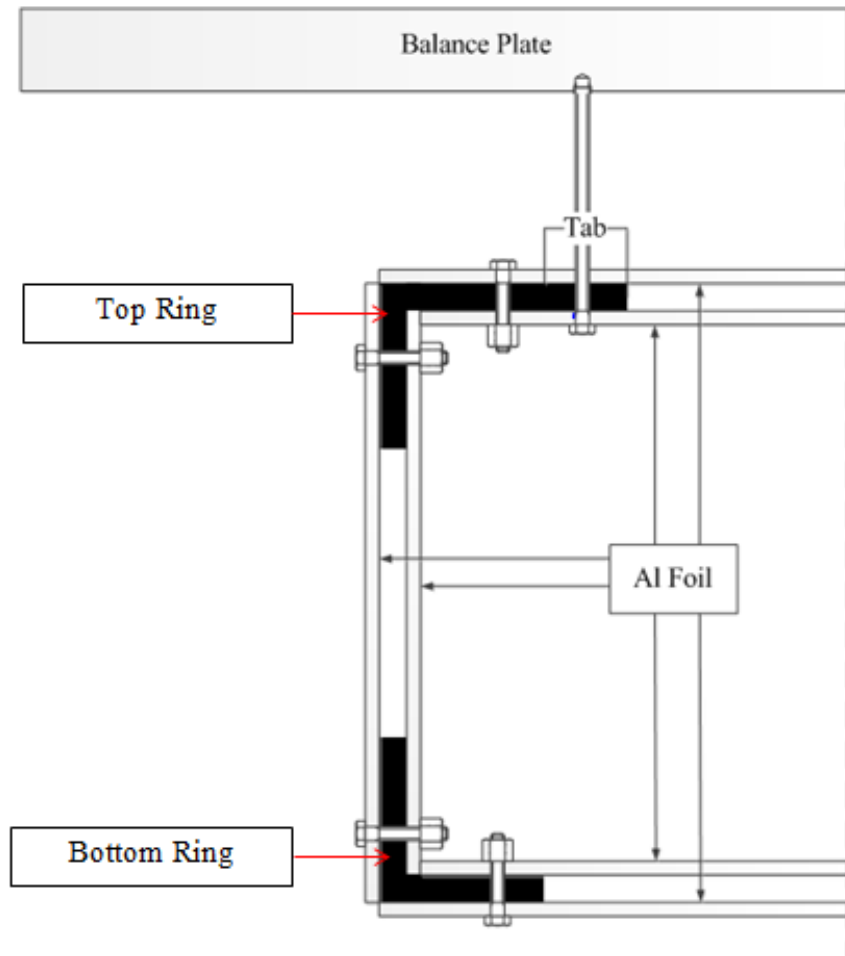


Figure 24. Cross section of the upper radiation shield (not drawn to scale)

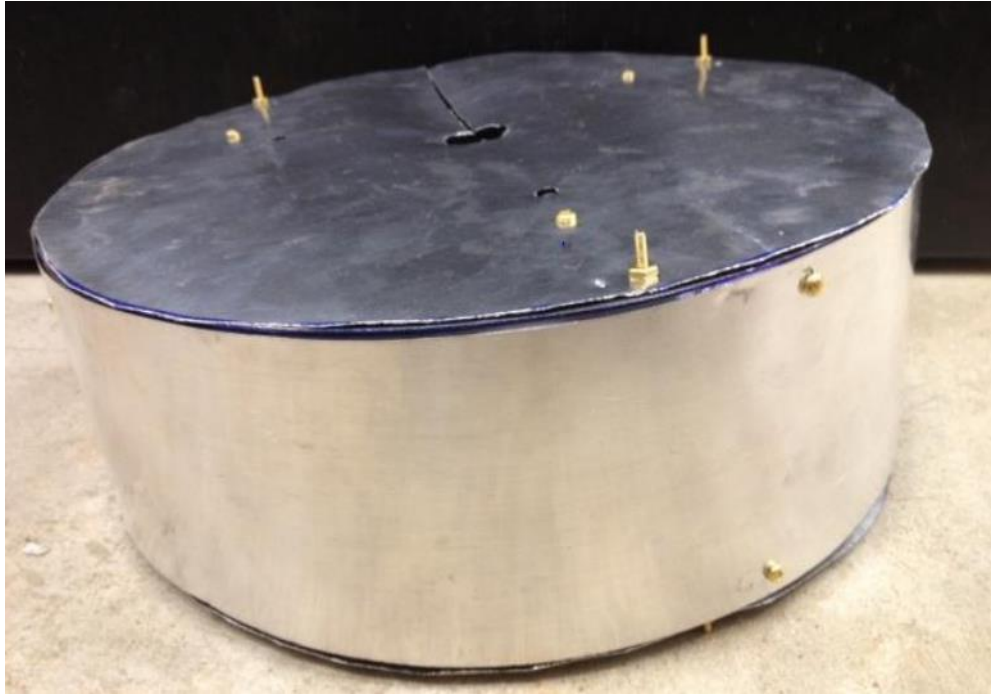


Figure 25. Upper radiation shield

2.1.7. Vacuum chamber and feedthroughs

The apparatus requires a feedthrough system to allow the many electrical leads and fluid supply tubes to pass from ambient pressure to high vacuum. The fittings for these systems, called Kwik Flange (KF or QF), are clamped together rather than bolted, soldered or welded allowing the easy assembly and disassembly. The construction material is aluminum because it has a smaller magnetic susceptibility than stainless steel. While most fittings such as tees, crosses, flanges are available from suppliers such as Kurt J. Lesker, McMaster Carr, or Ideal Vacuum, most feedthroughs must be special ordered or made in-house, including the feedthrough collar, feedthroughs for the SPRT, thermopile, and heater leads.

MDC Vacuum Products, LLC created an aluminum, 8 port, KF-40 feedthrough collar (SPEC# FTC0-K150-18-ALUMINUM) as shown in Figure 26. Each port is designated for a different type of instrumentation. These include the low voltage (thermometry) leads, high current (heater) leads, pressure readings (mentioned in the section above), feed line, and a two sided BNC connector (supplied from Kurt J. Lesker part # IFDBG012038) for the position sensor feedthrough.

The feedthrough collar was modified slightly by the Texas A&M Department of Chemistry machine shop for attachment to the balance plate and a vacuum chamber. An 18" O-ring groove, 8 through holes for 3/8" bolts and 8 through holes for 1/4" bolts were made on the top of the feedthrough collar for sealing against the balance plate.

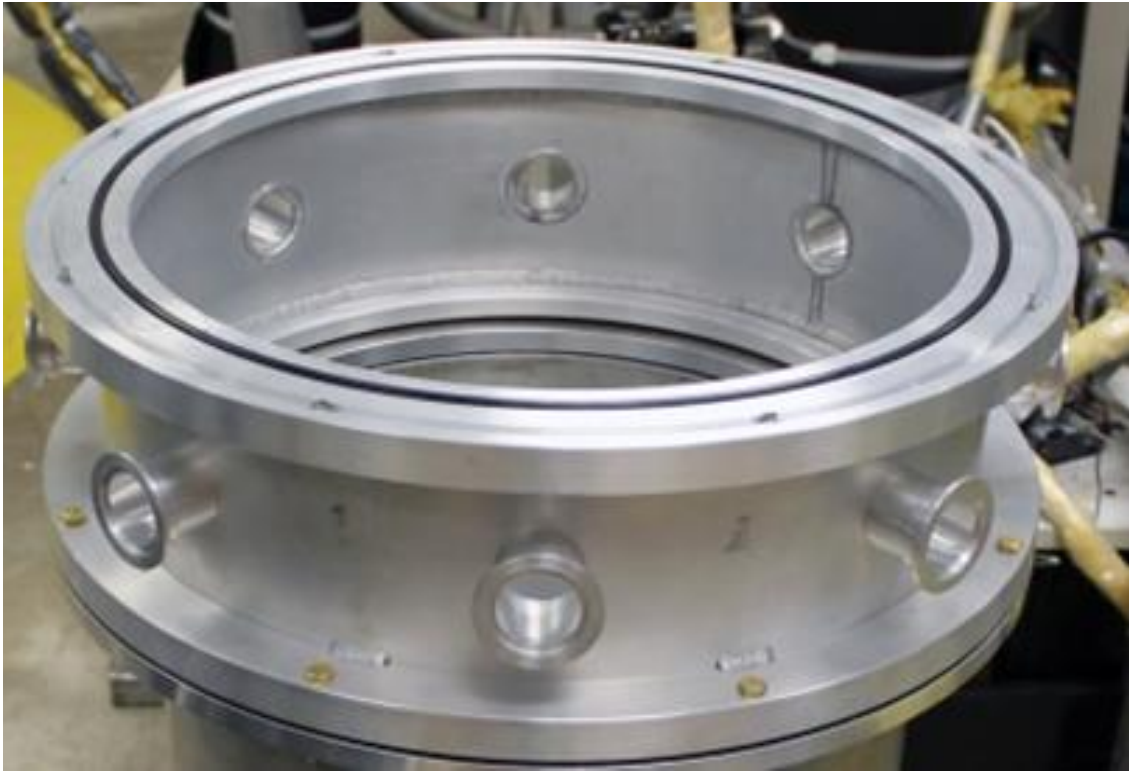


Figure 26. Feedthrough collar

A flange adapter made from a 20" aluminum circle with 16" and 17" O-ring grooves was created to match the slightly smaller seal diameter of the existing vacuum chamber. The flange adapter is bolted to the chamber by ¼"-20 brass socket head cap screws, and to the collar using hex head ¼"-20 screws and nuts. All seals are made with standard Buna-N O-rings.

All in-house feedthroughs consist of a blank flange (KF-40) with holes drilled and tapped completely through for ¼" NPT fittings. A Swagelok Ultratorr[®] fitting was tightened into the hole and the line/ lead fed through. For the feed line, the Ultratorr fitting was sufficient. For the thermometry leads, Apiezon Wax W (vacuum wax) was melted covered around the leads to fill all the empty spaces. Caution must be taken when coating the leads, as some material (such as Teflon) may prevent the wax from binding onto the surface.

LDC Vacuum Corporation created the RTD feedthrough system (WFT20-40-CC(26)10/16) that is composed of 20 copper buses (26 AWG copper wire) with Teflon sleeves. This system is pictured in Figure 27.

The vacuum line was attached to the same port as the thermometry leads due to limited vacuum hose length and proximity to where all electrical connections are made. All other ports contained blank flanges that could be used for other purposes such as lines for passing gases into the chamber or pressure relief devices.



Figure 27. RTD feedthrough flange

2.2. Auxiliary systems

2.2.1. Feed and compression system manifold

A specialized compression system is required to achieve the desired measurement pressures. Figure 28 shows the feed/compression system for the MSD. The main components of this system include:

- Mechanical vacuum pump capable of creating a vacuum of 10 mTorr inside the system (Varian Model SD-200)
- Piston type gas booster (Haskel[®] Model AG-303, minimum inlet pressure = 500 psi, maximum discharge pressure = 39,000 psi)
- Floating piston sampler (FPS), (Welker[®] Model CP-24GM, Maximum allowable working pressure (MAWP) = 1,800 psi)
- Mechanical hand pump (HiP Model 37-6-30, MAWP = 30,000 psi)
- Secondary vessel (HiP Model R1.5-10-30 MAWP = 30,000 psi)
- Fittings and valves (HiP with MAWP = 30,000 and 60,000 psi)
- Lamp heaters to keep the system temperature above the cricondentherm
- Compressing gas to power the Haskel[®] gas booster (Industrial grade nitrogen at 80-120 psi)

Gas cylinders are stored and preheated to around 60 °C in a thermostatted enclosure. The preheating ensures that the fluids are in a single phase and increases the pressure to assist with compression. 1/8" Swagelok[®] lines are run from the cylinder into the compression system. Then this is converted to 1/4" Swagelok[®] lines with a Swagelok[®] 2 micron in-line filter to prevent larger particles from entering the gas booster (Haskel[®]

AG 303). Then ¼” HiP lines and valves are used up to the inlet of the booster. Check valves are installed on both the inlet and outlet of the gas booster preventing any back flow of the fluid. At the outlet of the booster for the rest of the system 1/8” HiP valves and lines. All HiP equipment is rated for 30,000 or 60,000 psi. This entire setup is placed in a large box that is heated using heat lamps to make sure the fluid remains in a single phase.

There are three different types of compression schemes used for the MSD: primary compression, secondary stage compression, and compression via a floating piston sampler (FPS).

2.2.1.1. Primary compression

Primary compression is used when sample cylinder pressures are sufficiently high, typically > 1,500 psi, that a single pass through the Haskel® AG-303 booster provides the maximum pressure for the experiment. The pressure is increased using a pressurizing gas, nitrogen, fed through V-VFN to drive the booster. A 15 µm in-line filter (Swagelok®) is placed at the inlet of the drive side of the booster to prevent clogs. When the desired pressure is reached, the sample is fed slowly into the MSD through V-MSD. This process is repeated until the desired pressure has been reached within the cell. Care must be taken to close off the lower pressure transducer when going to higher pressure.

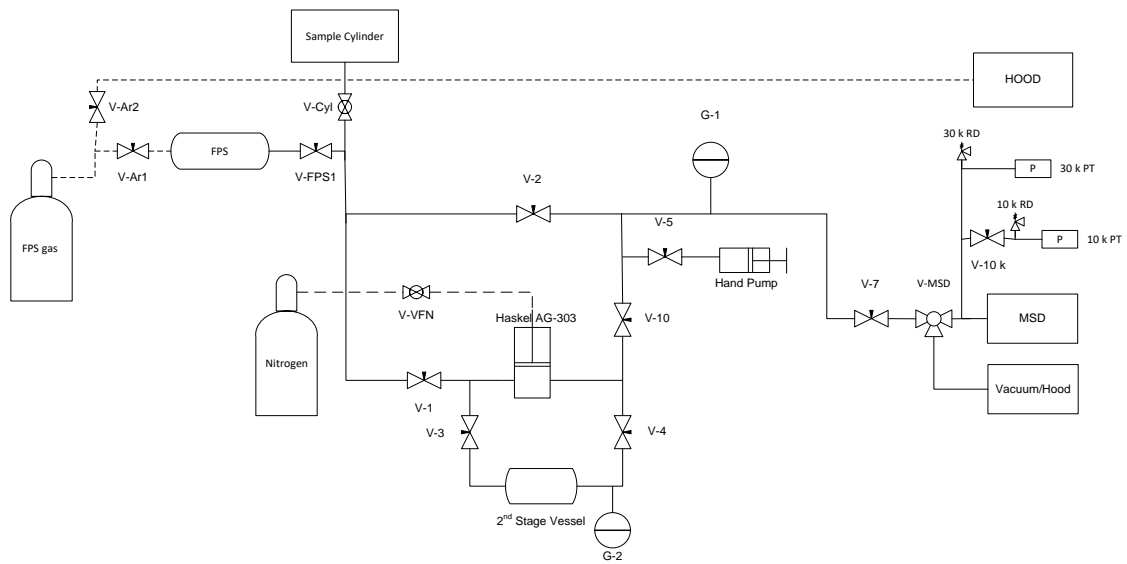


Figure 28. Compression system for the MSD with solid lines for the fluid of interest and dashed lines for compressing gases

2.2.1.2. Secondary compression

Secondary compression is used when primary compression is unable to reach the desired pressure for sample cylinder pressures above 500 psi. This uses compression from the sample cylinder into the 2nd stage vessel, then from the vessel into the lines. Compression into the vessel effectively increases the inlet pressure to the booster during the second stage, thereby overcoming the compression ratio limitations of the booster. The secondary compression setup is similar to primary compression (valve configuration: open; V-1, V-4, V-10; closed: V-3). Once the 2nd stage vessel is at the desired pressure (typically 2,000- 4,000 psi) secondary stage compression begins (valve configuration: open: V-3, V-10; closed: V-1, V-4) begins. The sample is fed into the cell using the process described in the previous section.

2.2.1.3. Floating piston sampler compression

If the pressure in the cylinder is < 500 psi or expected to drop below this pressure during the filling then the floating piston sampler (FPS) is required. For the compression side of the FPS, a cylinder of the same fluid or the major component in the sample with a higher pressure (maximum of 1,800 psi) and with a lower purity is required. This is done to minimize contamination in the case of leakage across the seal. To use FPS compression, the sample is admitted into the FPS through V-FPS1 with the other side of the FPS open to atmosphere. After the sample pressure in the FPS reaches that of the sample cylinder, V-FPS1 is closed and V-Ar1 is opened. Using the regulator on the compression cylinder, the pressure is increased until either the MAWP (1,800 psi), compression cylinder

pressure, or the sample side of the FPS is completely compressed (the piston is all the way to the end). This decreases the volume of the system, increasing the pressure in the lines and vessel.

Next, V-FPS1 is closed, and the FPS is depressurized on the compression side by releasing the fluid through the vent through V-Ar1 and V-Ar2. These steps can be repeated until the system reaches pressures where secondary stage compression can be used. Figure 29 shows an image of the FPS in the system.

2.2.2. High vacuum system

Vacuum insulation reduces significantly the heat loss caused by convection and conduction within the system for pressures below 10^{-4} Torr. Because a mechanical vacuum pump is not capable of achieving the required pressures, the high vacuum system includes both a mechanical (Welch model 1402) and a turbo pump (Varian Model-Turbo V-81-T).

An in-line liquid nitrogen trap protects the pumps and lowers the pressure by condensing any material that may be outgassing. Varian Model 0531 thermocouple gauges and a Bayard-Alpert dual tungsten filament glass ion gauge are used to measure the vacuum pressure. The flow diagram and an image are shown in Figure 30 and Figure 31. This system also facilitates calibration of the thermocouple gauges because the lowest pressures correspond to a reading of 0 mTorr.



Figure 29. FPS system used in the MSD

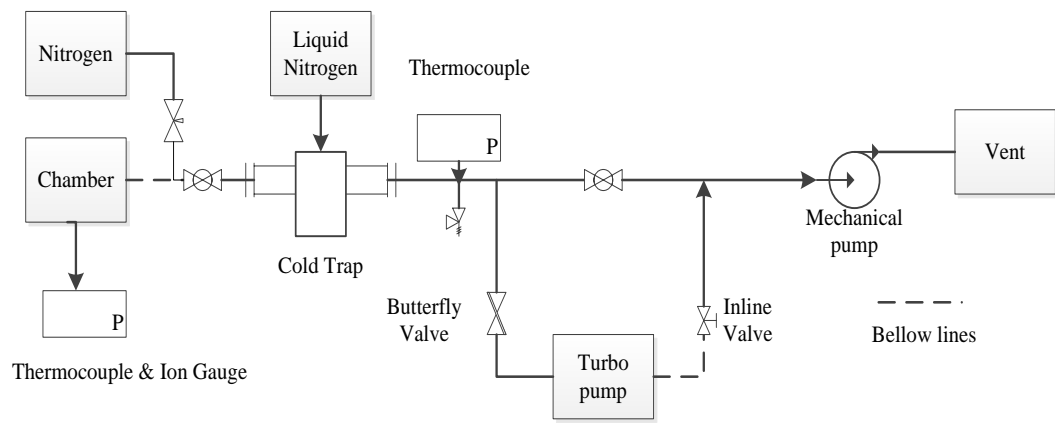


Figure 30. Schematic diagram of high vacuum pumping system for MSD



Figure 31. The high vacuum system (mechanical pump not shown)

2.3. Temperature measurement methodology and control

For the temperature measurements, two constant current sources (shown in Figure 32), each having current reversal abilities to minimize errors from electromotive forces (EMF), similar to the one used by Ejaz [41] and Athilan [40] were used. With two current sources, the SPRT and RTD measurement circuits were separated to reduce potential interference. Each current source had variable currents that were set at approximately 0.25 mA for all measurements. Grounded shields protect the thermometry leads from extraneous electrical signals.

To determine the current, a temperature stable JRL 100 Ω standard resistor (100.01753 Ω for the SPRT circuit and 99.99560 Ω for the RTD circuit) were placed in series with each thermometry system. Measurements of the forward and reverse voltages were recorded. These voltages were typically within 30-50 μV of each other for the SPRT and 20-30 μV for the standard resistors. Ohm's law gives the forward and reverse voltages as:

$$V_+ = IR_{PRT} + V_{EMF} \quad (2.5)$$

$$V_- = -IR_{PRT} + V_{EMF} \quad (2.6)$$

Taking the average of $|V_+|$ and $|V_-|$ eliminates the EMFs:

$$\frac{V_+ - V_-}{2} = IR_{PRT} \quad (2.7)$$



Figure 32. Current sources fabricated by the physics electronics shop at TAMU

The current is identical for the standard resistor and SPRT so the two can be equated together;

$$I = \frac{V_{+,PRT} - V_{-,PRT}}{2R_{PRT}} = \frac{V_{+,Std} - V_{-,Std}}{2R_{Std}} \quad (2.8)$$

$$R_{PRT} = R_{Std} \frac{V_{+,PRT} - V_{-,PRT}}{V_{+,Std} - V_{-,Std}} \quad (2.9)$$

Resistance is then converted to temperature using ITS-90 [69] using the ratio of resistances at the measuring temperature and at a standard temperature, the triple point of water in our case. This ratio is important to note because if measurements are made at the triple point of water using the same standard resistor as the experiments, the temperature measurement are unaffected by uncertainties in the standard resistor. A water triple point measurement made on January 27, 2017 to check the calibration of the SPRT after repairing the SPRT leads yielded a resistance of 100.4302 Ω . This result agrees value of 100.4293 Ω measured by Dr. Mark McLinden at NIST in 2005 indicating no major shifts in the calibration. The value of 100.4302 Ω was used to calculate temperatures. The original calibration completed by Minco appears in Appendix E [70].

For the RTD's, the same measurement approach as in equation 2.9 is used but values are converted to temperature using the Callendar-Van Dusen equation as recommended by the RTD supplier (OMEGA[®]). No measurement of the triple point of

water was made as the primary function of the RTD is for temperature control, not temperature measurement accuracy.

All voltage (thermometry) measurements were made with a 6½ digit multimeter (DMM) with a scanning card (Keithley 56 Instruments® model: 2000-20-SCAN, serial number 0832694) and 44-pin connector with twisted pairs (Model 2000-MTC-2 cable). Measurements were sent directly to the computer using a GPIB cable.

For temperature control, a custom-built heater power control box, shown in Figure 33, was created by the physics department at TAMU and is detailed in [40]. The system uses LabVIEW, a DAQ card, solid-state relays (SSR) and a variable voltage power supply (STACO, INC Type 3PN1010) to control the on/off action of the heater. The variable voltage power supply was set manually depending upon the desired temperature. An overview of the entire temperature measurement and control system is in Figure 34.

2.4. Pressure measurement

The pressure measuring devices are three Paroscientific® oil-free absolute pressure transducers (PT). The transducers have maximum pressures of 6,000 psi (41.7MPa) Model 46 K-101 (serial number 84267), 10,000 psi (68.9 MPa) Model 410 K-101 (serial number 106030), and 30,000 psi (206 MPa) Model 430 K-101 (serial number 80872) with uncertainties of ± 0.01 % full scale and NIST traceable calibrations. Although it is not advised, the transducers may be subjected to pressures about 20% above their MAWP without causing damage to the transducer. Only two transducers were used during measurements, one for the high pressure range, 30,000 psi PT and one for the low pressure

range, either the 6,000 or 10,000 psi PT. Initially, the 6,000 psi pressure transducer was used for the lower pressure measurements, however it was replaced by the 10,000 psi gauge to help reduce uncertainty over the intermediate portion of the pressure range.

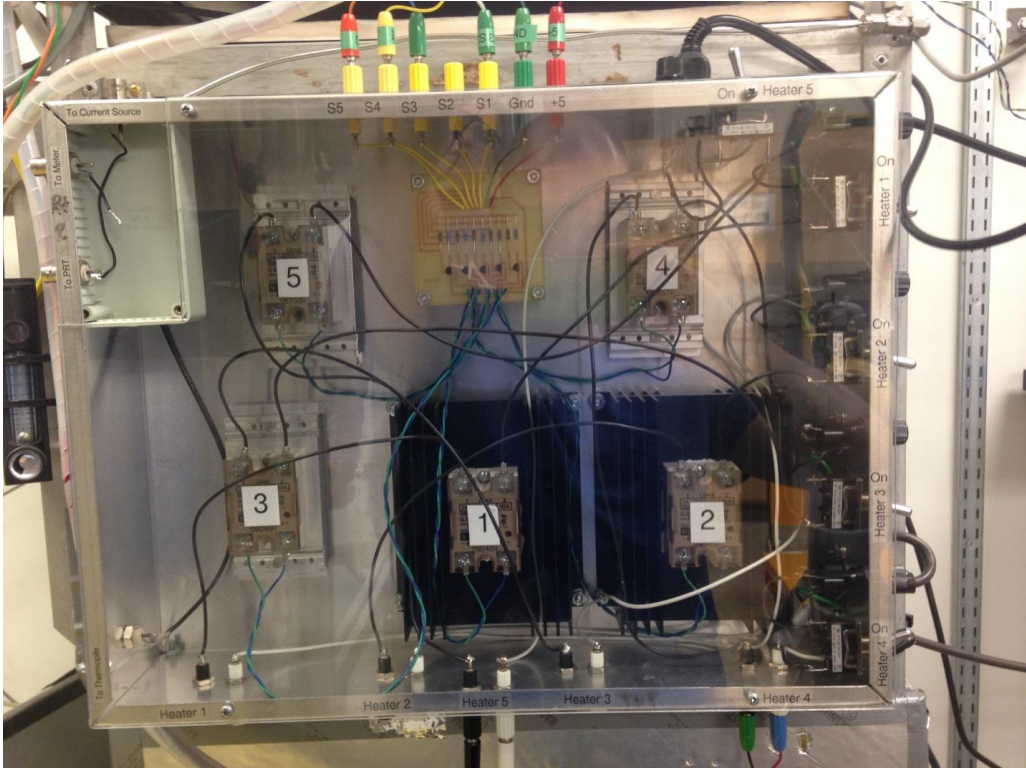


Figure 33. Heater power control box

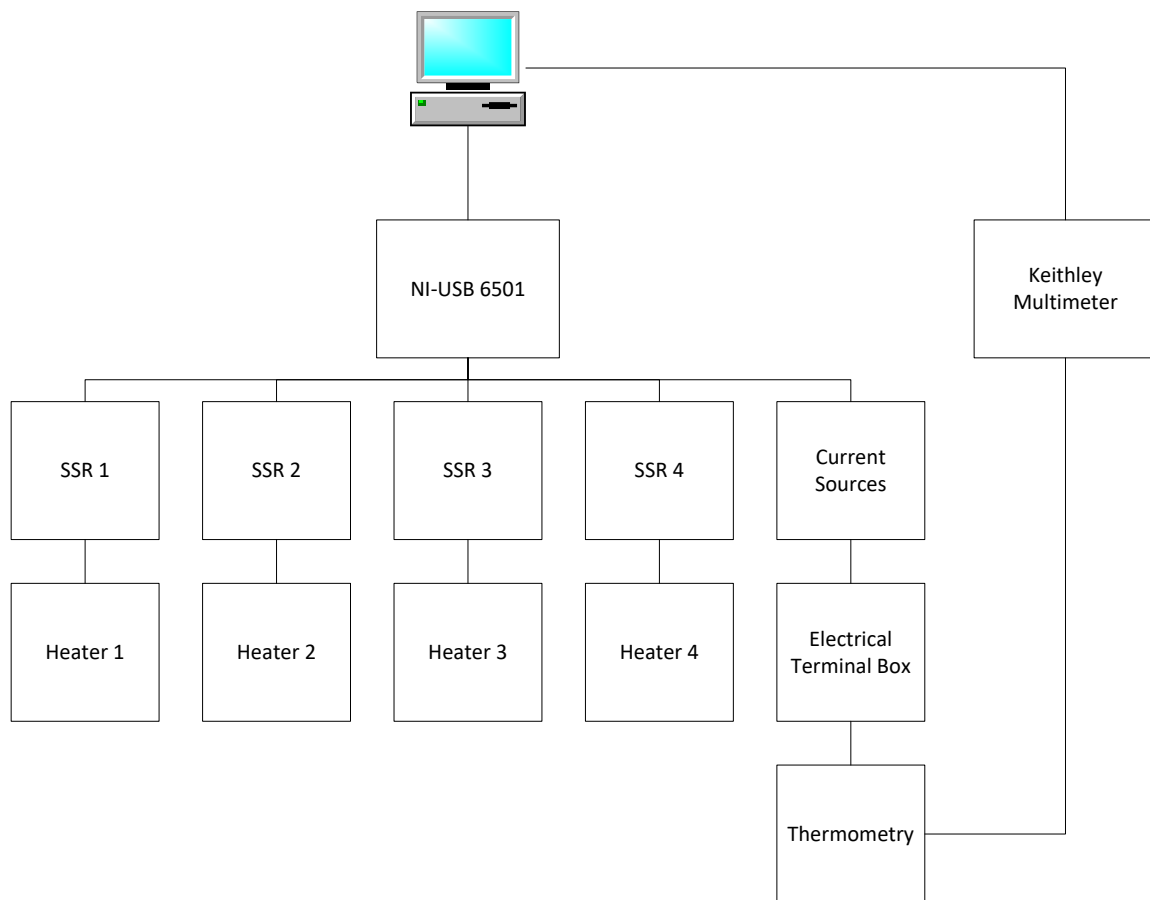


Figure 34. Overview of temperature measurement and control system

These transducers work using a quartz crystal oscillator whose resonant frequency of oscillation changes as stress (pressure) is applied to the system. The resonant frequency also varies with temperature, which is accounted for using an additional temperature-sensing quartz crystal. Both frequency outputs are sent to a Model 735 or 740 display for the 10k or 30k transducers respectively. These displays then calculate both the temperature and pressure using a predetermined calibration equation and coefficients. These calibration coefficients determined by Paroscientific® are Appendix F.

To ensure stable measurements, all transducers are kept above ambient temperatures at 36 °C in individual thermo-stated blocks. These blocks are composed of aluminum semi-cylindrical blocks (4” diameter, 9” long) with holes drilled out for the pressure transducer, a 3- lead 100 Ω RTD (OMEGA® Model:RTD-2-1PT100KN2528-108-T) and a cartridge heater [22]. PID controllers from OMEGA® (CNi series) provided temperature control. A schematic diagram of this setup is shown in Figure 35.

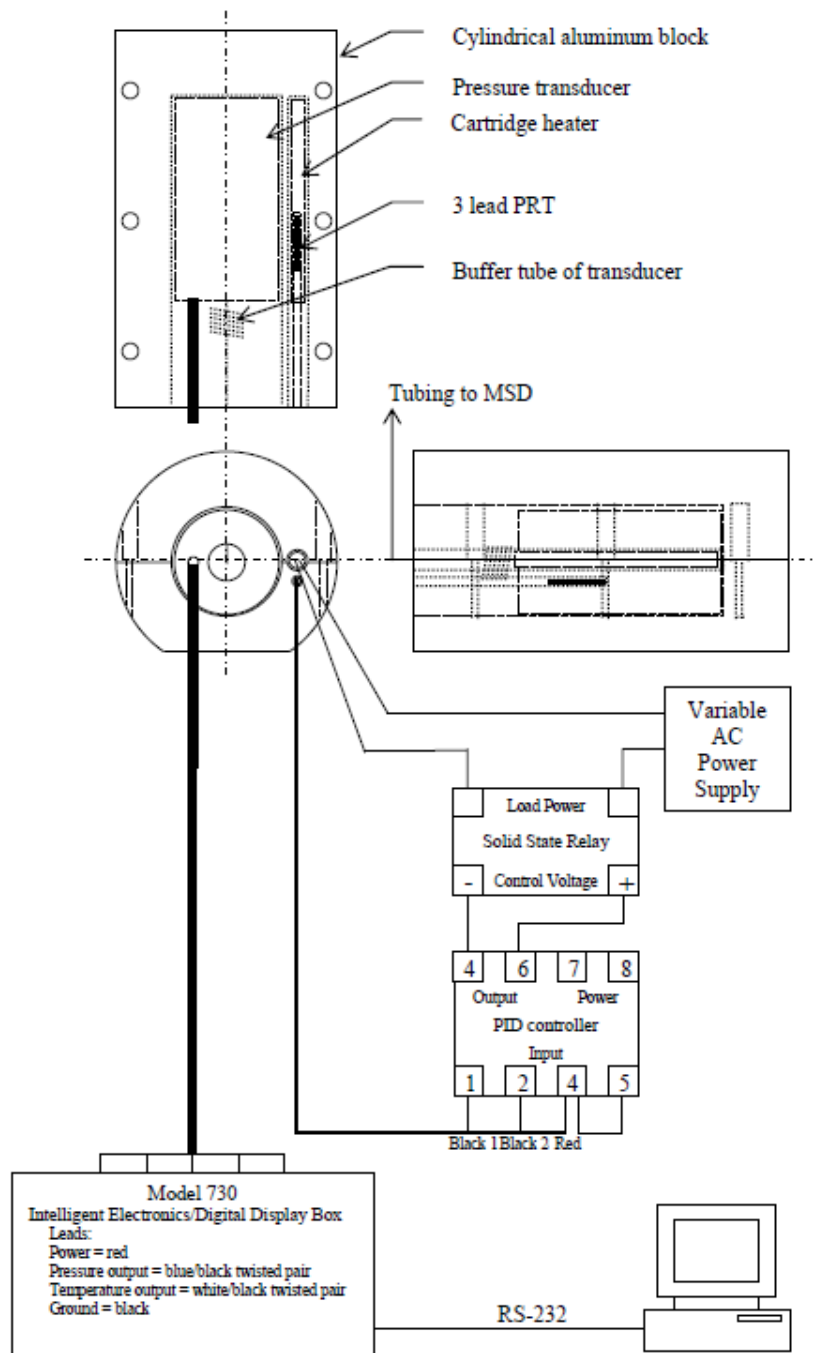


Figure 35. Pressure transducer setup [22]

The entire pressure measurement system is located on the balance plate to reduce dead volume and the amount of line exposed to ambient temperature. The thermo-stating blocks are wrapped in fiberglass insulation and placed in a Styrofoam box to minimize heat transfer to the balance plate. The entire setup is covered by fiberglass sheets for another layer of thermal protection.

2.5. LabVIEW data acquisition

The LabVIEW programs are similar to the programs described in [40] but were updated for the new equipment and methodology. Now, all communications with the instruments used a National Instruments™ USB-6501, while LabVIEW 2012 read and collected measured properties such as pressure, temperature, and mass.

Modifications for the temperature programs include: a new program to control the second current source, calculations and readouts for the additional thermometry and PID controllers for temperature control of the shields. Included in the updates is the sequence used by the temperature control. Previously, temperature measurement cycles and the control program ran sequentially. As a result, the PID controller action would be interrupted for as much as 30 seconds, resulting in problems with temperature stability. This is especially troublesome when measuring at higher temperatures.

Currently, temperature measurement cycles and the control program run in parallel, allowing constant temperature control. This was achieved by creating a local variable for the shield temperatures in which a data bank of temperature measurements were kept and updated constantly. This allowed the controller always to have a value for

comparison and control. Five seconds were chosen as the time for the controller to apply the on/off, although once this finished the control started again with the most recent temperature measurement (essentially allowing constant control).

The mass program was updated to a new measurement sequence as described in Section 2.1.4. To accomplish this task, the existing LabVIEW program was modified to activate the LPT port pins to provide the calibration point results. An overview of all the components used in the mass measurement process is Figure 36.

Izidro [71] determined the pin combinations for controlling both the weight changing device and suspension system, in which D0-D2 control the weight changing device and D4-D7 control the suspension. This created the calibration point by activating pins D1, D2, and D5 as shown in Figures 37 and 38. More information is available on pages 19-21 of Izidro [71].

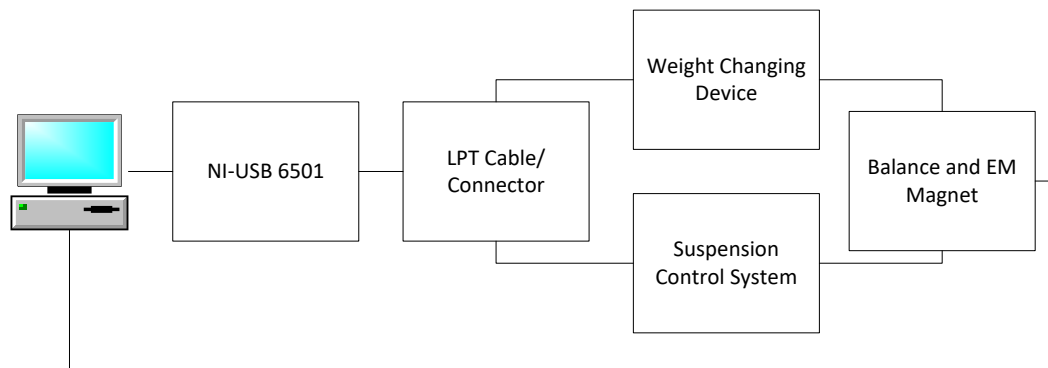


Figure 36. Overview of the communication between the equipment used in the mass measurements

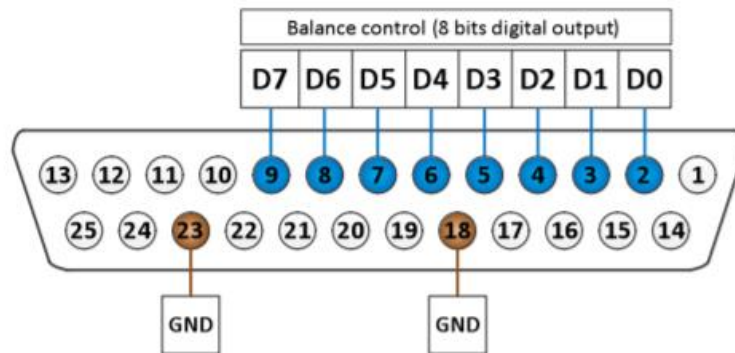


Figure 37. Illustrates the LPT port pin combination required for controlling the suspension coupling and weight changing device [71]

Balance control (8 bits digital output)								Balance state	Σ
2^0	2^1	2^2	2^3	2^4	2^5	2^6	2^7		
F 0	F 0	F 0	F 0	F 0	F 0	F 0	F 0	OFF ZP MP 1 MP 2	0
F 0	F 0	F 0	F 0	F 0	T 32	F 0	F 0	OFF ZP MP 1 MP 2	32
T 1	F 0	T 4	F 0	F 0	T 32	F 0	F 0	OFF ZP MP 1 MP 2	37
F 0	T 2	T 4	F 0	F 0	T 32	F 0	F 0	OFF ZP MP 1 MP 2	38
F 0	F 0	F 0	F 0	F 0	T 32	F 0	T 128	OFF ZP MP 1 MP 2	160
T 1	F 0	T 4	F 0	F 0	T 32	F 0	T 128	OFF ZP MP 1 MP 2	165
F 0	T 2	T 4	F 0	F 0	T 32	F 0	T 128	OFF ZP MP 1 MP 2	166
F 0	F 0	F 0	F 0	T 16	T 32	F 0	T 128	OFF ZP MP 1 MP 2	176

Figure 38. Image of the table for pin combination commands for the balance [71]

2.6. Silicon sinker

To reduce uncertainties and increase the sensitivity of the measurements, the sinker density should be relatively close to the density the fluids of interest. So silicon was explored as the sinker material as it has a density approximately half that of titanium, thus reducing our errors by approximately the same magnitude.

A silicon sinker was machined from a single crystal silicon supplied by Valley Design Corp. Additional machining was done by the physics machine shop at Texas A&M University by sanding the sinker down with silicon carbide wet or dry sandpaper. Sanding started with 60 grit paper for a rough finish up to 2000 grit for the final finish.

The density of the sinker was determined by Dr. Mark McLinden at NIST to be $\rho = 2.329096 \text{ g/cm}^3$ at $T = 20 \text{ }^\circ\text{C}$.

To determine the new silicon sinker mass the following force balance equation was used;

$$W_i = \alpha m_i - \rho_{air} \frac{m_i}{\rho_i} \quad (2.10)$$

With W_i as the mass observed by the balance in grams, the second term being the true mass of the object modified by the balance calibration factor (α), and the final term represents the buoyancy force acting on the object. Measurements were also performed on the titanium sinker to compensate for the balance calibration factor (α) rather than using the standard value of 1.00015. Sinkers were left for more than 24 hours near the balance to allow for thermal equilibration. Measurements of the room temperature and pressure were also recorded to estimate the density of the air. This was repeated multiple times over two days with consistent results.

The mass and volume were determined to be $m_{si} = 15.79148 \pm 0.00005$ g and $V_{si} = 6.78009$ cm³ at $T = 21$ °C and $p = 1$ atm. Helium and argon isotherms validate the silicon sinker properties at 305 K. The helium isotherm measurements using the silicon sinker are discussed further in Section 3.2.3.

Though silicon was explored as the sinker material, it exposed a limitation of the suspension and coupling system. While trying to measure argon, a fluid with approximately half the density of the sinker (~ 800 kg·m⁻³) at higher pressures the suspension and coupling system fail to control the lift of the sinker.

The control system is proprietary intellectual property, so we cannot confirm the exact reason. Our hypothesis is that at a certain mass the EM does not detect enough mass and resets the system. Accurate measurements could be obtained at densities below this point but once the threshold was passed the system failed. Additionally, observations of the voltage during the measurements were noted. The system could easily suspend the PM independently with the proper voltage however once the sinker was suspended differences were seen in the voltage output eventually leading to the system resting.

First, the voltage reaches the appropriate value and then slowly starts to decline from this value until it reaches the same voltage as observed in ZP. Once it reaches this value, the control system resets the system to read this as the “OFF” voltage and it requires a hard reset of the system to enable it to work again. Testing if this limitation was truly the case rather than another potential issue with the control system, the titanium sinker was reinstalled and argon measurements conducted at 305 K twice. Both resulted in no

failures of the suspension and control system and accurate measurements helping validate our hypothesis.

As fluids that would put us close or pass this threshold of density, especially at higher pressure were our main focus, the titanium sinker was reinstalled into the MSD. The silicon sinker only is useful for fluids with densities less than $800 \text{ kg}\cdot\text{m}^{-3}$.

During this process, masses of the compensations weights were also measured as some scratches were seen on the weights. Results showed that the weight difference between the weights decreased to $m_{Ta} - m_{Ti} = 30.38003 \text{ g}$. All measurements (helium, argon, nitrogen, methane + helium) used the previous reported value of $m_{Ta} - m_{Ti} = 30.38493 \text{ g}$ [22] but the change is noted for future work.

2.7. Re-commissioning and checking for bias errors

Once the system was assembled, the lines pressure tested to 200 MPa, the PID controllers tuned, vacuum integrity verified to $\sim 10^{-4}$ Torr, and balance aligned to achieve expected stability, nitrogen density measurements were used to verify system operation. Nitrogen has an accurate reference equation [47] and previous measurements at high pressures [32] allow multiple comparisons.

At higher temperatures (450-500 K) region, the maximum measured pressure must be reduced from 200 MPa to as low as 173 MPa because of declining material strength at these temperatures. This restriction is based upon the ASME boiler and vessel codes, assuming that we have a class 2 vessel [72]. The ASME equation calculates the maximum allowable working pressure (MAWP) based upon the ultimate tensile strength of the

material at test temperature divided by the ultimate tensile strength of the material at the design temperature, referred to as the LSR. Assuming that the hydrostatic test was done at ambient temperature, 293 K and the hydrostatic test pressure is 300 MPa [22]. The equation for MAWP is:

$$MAWP = \frac{P_{Test}}{1.3 * LSR} \quad (2.11)$$

Using data from Edwards [73] and Weggel [74], multiple ultimate tensile strengths were found. Because the process for forming the CuBe cell is unknown, the lowest MAWP calculated from all the data was used for the MAWP as a precaution.

3. DENSITY MEASUREMENTS

Densities for pure fluid nitrogen were measured at temperatures between 303 and 450 K up to 200 MPa to validate the redesign described in Section 2. Once validated, the MSD was used to measure two pure fluids, helium and argon and three binary mixtures of methane + helium with compositions of 75, 45, and 25 mol% methane. These were made gravimetrically using an in-house apparatus. A replicate of each of these mixtures was tested at one isotherm to ensure compositions of the mixtures were consistent. Gas purities and suppliers are provided in the Table 1.

The uncertainty analysis for the density measurements is discussed first, followed by the measurements of the pure fluids. Finally mixture preparation methods and mixture measurements are discussed.

3.1. Uncertainty analysis

Contributions to the uncertainty arise from the apparatus, thermometer, pressure sensors, and compositions of the mixtures. All these effects are independent, therefore, the overall expanded uncertainty (95% confidence limit) is

$$\begin{aligned} [U_c(r)]^2 = & [U^{app}(r)]^2 + \left[\left(\frac{\partial r}{\partial p} \right)_{T, x_i} U(p) \right]^2 + \left[\left(\frac{\partial r}{\partial T} \right)_{p, x_i} U(T) \right]^2 \\ & + \sum_{i=1}^N \left[\left(\frac{\partial r}{\partial x_i} \right)_{p, T, x_{j \neq i}} U(x_i) \right]^2 \end{aligned} \quad (3.1)$$

Table 1. Supply gas cylinder specifications

<i>Component</i>	<i>Supplier</i>	<i>Mole fraction purity</i>	<i>Purification method</i>
Methane	Airgas	0.99999	none
Helium	Airgas	0.999999	none
Argon	Matheson TriGas	0.999999	none
Nitrogen	Praxair	0.999997	none

Ortiz-Vega *et al.* [75] provide a full analysis of the uncertainty for our MSD. The main contribution to the apparatus effect is the force transmission error (FTE), which was determined by a vacuum test before and after each isotherm as described by McLinden *et al.*[42] and Cristancho *et al.*[43]. The SPRT has an uncertainty of 3 mK and stability of 5 mK. The pressure transducers have uncertainties of ± 0.01 % of full scale, 0.6 psi (0.004 MPa) and 3 psi (0.021 MPa) respectively. The sample purities shown in Table 1 indicate that compositional effects for pure fluids are negligible. For mixtures, the balance used to build the mixtures has a resolution of 0.1 g. The apparatus effect tends to dominate the overall uncertainties over most of the range, with pressure uncertainties also contributing significantly at the lower pressures for each transducer.

A separate analysis for each of the fluids will be presented in their respective sections because uncertainties reflect the differences in their derivatives and compositional effects.

3.2. Pure components density measurements

3.2.1. Nitrogen

Nitrogen measurements were compared to previous data from Mantilla *et al.* [32] on our MSD before the redesign. The results are shown for two isotherms in Figure 39 , which shows differences between the experimental measurements and the Span *et al.* [47] reference EoS. This includes the nitrogen isotherm at 303 K taken after a shift occurred in the FTE.

The uncertainty stated for the EoS is $\pm 0.0002 \cdot \rho$ at temperatures between 240 and 523 K up to 30 MPa and $\pm 0.006 \cdot \rho$ for higher pressures. In all cases, the agreement between the current measurements and those of Mantilla *et al.* [32] is within the combined uncertainties of the EoS and the experimental uncertainties. The experimental data is presented in Appendix G Table G.1.

3.2.2. Argon

Argon measurements were made at temperatures of 303 to 450 K at pressures to 200 MPa and compared to the Tegeler *et al.* reference EoS [49]. Figure 40 presents the results. The measurements are within $\pm 0.0005 \cdot \rho$ of the values predicted by the reference EoS, except for the lower pressures of the 400 K isotherm. These deviations are as high as $\pm 0.0015 \cdot \rho$, but still within the combined uncertainties of the EoS and our experimental uncertainties in Table 2. The EoS states a density uncertainty of $\pm 0.0010 \cdot \rho$ at pressures above 30 MPa, however it predicts densities well within $\pm 0.0005 \cdot \rho$.

The experimental results show that the uncertainty of the EoS actually is $\pm 0.0005 \cdot \rho$ for temperatures from 300 to 450 K at pressures below 200 MPa, which half of that estimated without experimental results. Gomez-Osorio *et al.* [19] took advantage of this to use argon as a calibration fluid for a vibrating tube densimeter. The experimental values for argon appear in Table G. 2 of Appendix G.

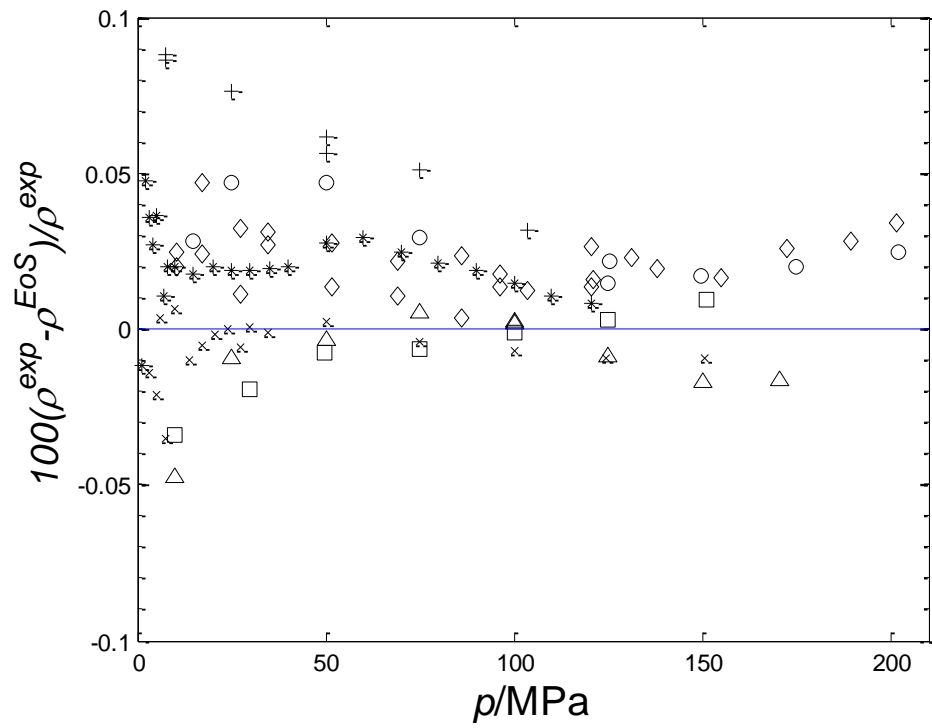


Figure 39. Relative deviations of measured nitrogen densities compared to Span *et al.* [47] reference EoS for this work * 303 K, + 398 K and Mantilla *et al.* [32] □ 298.15 K, △400 K

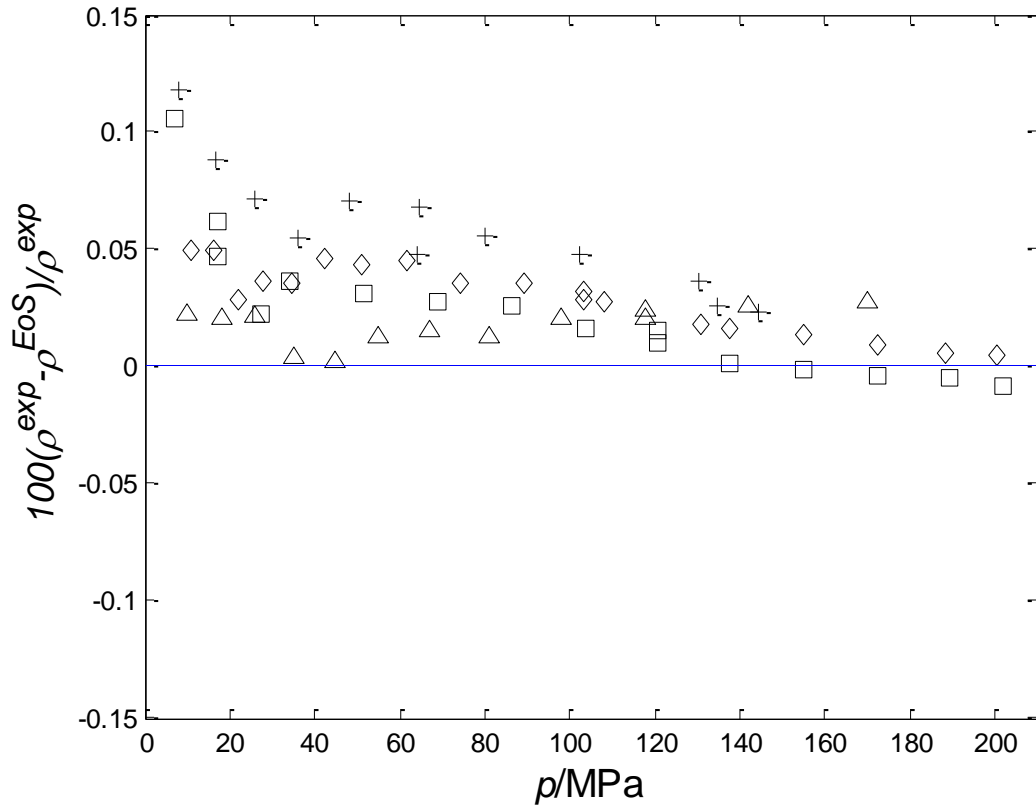


Figure 40. Relative deviations of measured argon densities compared to the Tegeler *et al.*

[49] reference EoS for this work \square 303 K, \diamond 350 K, $+$ 400 K, and \triangle 450 K

Table 2. Argon measurement uncertainties

term	<u>coefficients</u>			density equivalent kg·m ⁻³
	expanded uncertainty (95% confidence limit)	derivative	source	
apparatus, $U(\rho)^{\text{app}}$	0.07 kg/m ³			0.07
temperature, $U(T)$	10 mK	$\left(\frac{\partial \rho}{\partial T}\right)_{P,m_i}$	EoS	0.001
pressure, $U(p)$	0.0207 MPa (HPT) 0.004 MPa (LPT) ^a	$\left(\frac{\partial \rho}{\partial p}\right)_{T,m_i}$	EoS	0.002-0.036

^a The Paroscientific[®] transducer accuracies specified by the manufacturer is $\pm 0.0001 \cdot p_{\text{max}}$, in which p_{max} is 41.3 MPa and 206.8 MPa for the low (LPT) and high (HPT) pressure transducers, respectively

3.2.3. Helium

Helium measurements were made at temperatures between 303 and 450 K at pressures up to 200 MPa. The relative density deviations of the measurements from the Ortiz-Vega reference EoS [50] appear in Figure 41. Deviations trend upward, reaching a maximum of around $\Delta\rho / \rho = 0.60\%$ at pressure of 175 MPa. The new measurements can be used to improve the equation prediction capabilities at higher pressures and temperatures. The experimental values appear in Appendix G Table G. 3 and the experimental uncertainties in Table 3.

At pressures below 50 MPa, the low helium mass densities and limitations of our apparatus introduce considerable scatter into the measured densities. The uncertainty mainly comes from the apparatus effect, which is dominated by the FTE and the resolution of the balance. To reduce this effect, the silicon sinker discussed above, which has approximately half the density of the titanium sinker, was tested at 303 K. Once the silicon sinker was installed, both the uncertainty of the apparatus and the FTE dropped from approximately 0.09 to 0.05 kg m⁻³ and 200 to 50 ppm.

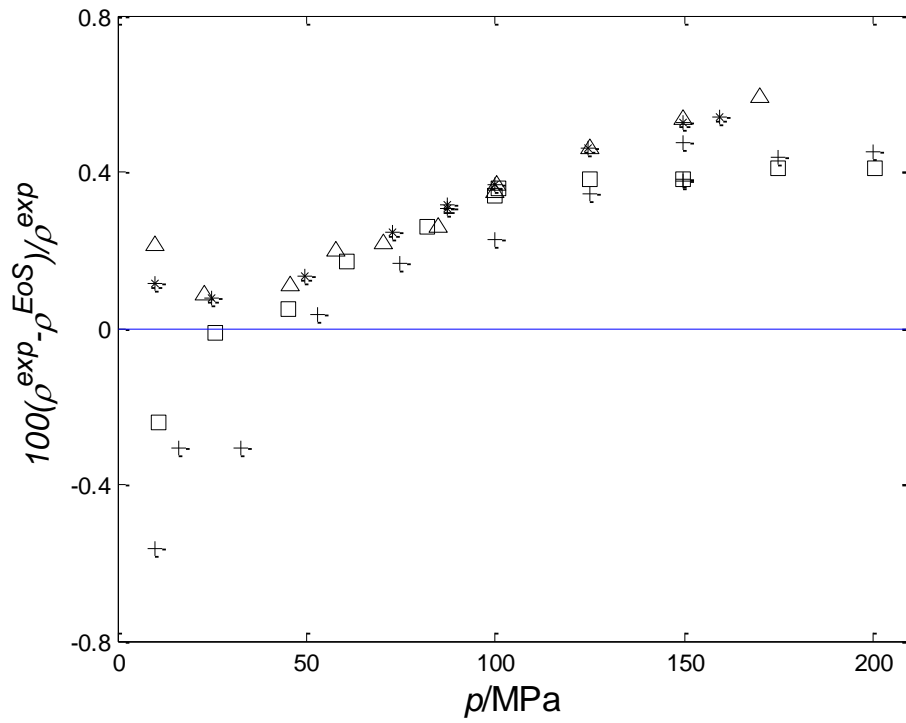


Figure 41. Relative deviations of measured helium densities compared to the Ortiz-Vega *et al.* [50] reference EoS for this work \square 303 K, $+$ 350 K, $*$ 399 K, and Δ 450 K

Table 3. Helium measurement uncertainties

term	<u>coefficients</u>			density equivalent kg·m ⁻³
	expanded uncertainty (95% confidence limit)	derivative	source	
apparatus, U(ρ) ^{app}	0.07 kg/m ³			0.09
temperature, U(T)	10 mK	$\left(\frac{\partial \rho}{\partial T}\right)_{p,m_i}$	EoS	0.001-0.007
pressure, U(p)	0.0207 MPa (HPT) 0.004 MPa (LPT) ^a	$\left(\frac{\partial \rho}{\partial p}\right)_{T,m_i}$	EoS	0.005-0.019

^a The Paroscientific[®] transducer accuracies specified by the manufacturer is $\pm 0.0001 \cdot p_{\max}$, in which p_{\max} is 41.3 MPa and 206.8 MPa for the low (LPT) and high (HPT) pressure transducers, respectively

To ensure the quality of the data, the titanium sinker was reinstalled and tested again. Figure 42 shows helium measurements with the silicon sinker and titanium sinker before and after the use of the silicon sinker. All three data sets match within their respective uncertainties. One important observation is that the silicon sinker values at lower density agree well with the reference EoS. This can be attributed to the lower uncertainty in the measurements as a result of the sinker and fluid being closer in density. At higher pressures, this effect diminishes and both sinkers have about the same precisions.

The silicon sinker improves the lower density measurements. However, when measurements of argon were attempted at 303 K, the control system failed at densities greater than 800 kg m^{-3} , as discussed in Section 2.6. This greatly limits the short-term versatility of the apparatus, by requiring that the sinkers be changed when alternating between high density and low density fluids. Because of this limitation, the titanium sinker was used for the remainder of the measurements.

3.3. Methane + helium mixtures

Binary mixtures data provide useful information, such as component interactions, which can improve predictions. Most compositions for previously measured binary mixtures have been chosen based upon their industrial applications. This choice is not optimal because it may not capture the desired compositional dependence. In 1990, Eubank and Hall [76] proposed that the optimal molar mixture compositions to determine the second and third cross virial coefficients are 0.50 for the second virial coefficient and 0.25 and 0.75 for the third virial coefficient.

Few measurements exist for methane + helium mixtures, with none at pressures greater than 20 MPa and compositions less than 0.50 of methane. New measurements can improve correlations for methane + helium, especially at higher pressures and higher helium compositions.

Three binary mixtures of methane + helium, at nominal compositions of 0.75, 0.50, 0.25 mole fraction of methane were prepared using an in-house mixing apparatus and measured in the MSD at temperatures of 303 to 450 K at pressures up to 200 MPa. Measurements were compared to both GERG 2008 [57] and AGA8-DC92 [58]. Our measurements agree with and compliment those of Hernández-Gómez *et al.* [55, 56], who measured mixtures with methane mole fractions of 0.95, 0.90, and 0.50 at temperatures from 240 to 400 K and pressures up to 20 MPa.

3.3.1. Sample preparation

Mixtures were prepared using an in-house gravimetric synthesis apparatus shown in Figure 43. Equipment descriptions are:

- Balance (Sartorius® IS64EDE-H balance (S/N 31506867) with a range of 64 kg with 0.1 g resolution)
- Mechanical vacuum pump (Varian SD-200)
- Turbo Pump (Pfeiffer Vacuum TPH-050)
- High vacuum gauge capable of reading pressures as low as 10^{-7} Torr (Varian 843 Vacuum Ionization gauge)
- Ion gauge capable of reading pressures below 10^{-3} Torr (Bayard-Alpert dual tungsten filament glass ion gauge)
- Temperature sensor denoted by TS (OMEGA® Dpi temperature monitor)
- Pressure sensor denoted by PS (Paroscientific® Model 740 digiquartz digital barometer)
- Acrylic box

The system has multiple ways to purify the sample gases, but these were not used in the construction of the mixtures detailed below because the typical purities ($x_i \geq 0.99999$) available from commercial suppliers provided negligible contributions to the overall uncertainty of the mixture composition. The balance is the principle source of mixture composition uncertainties.

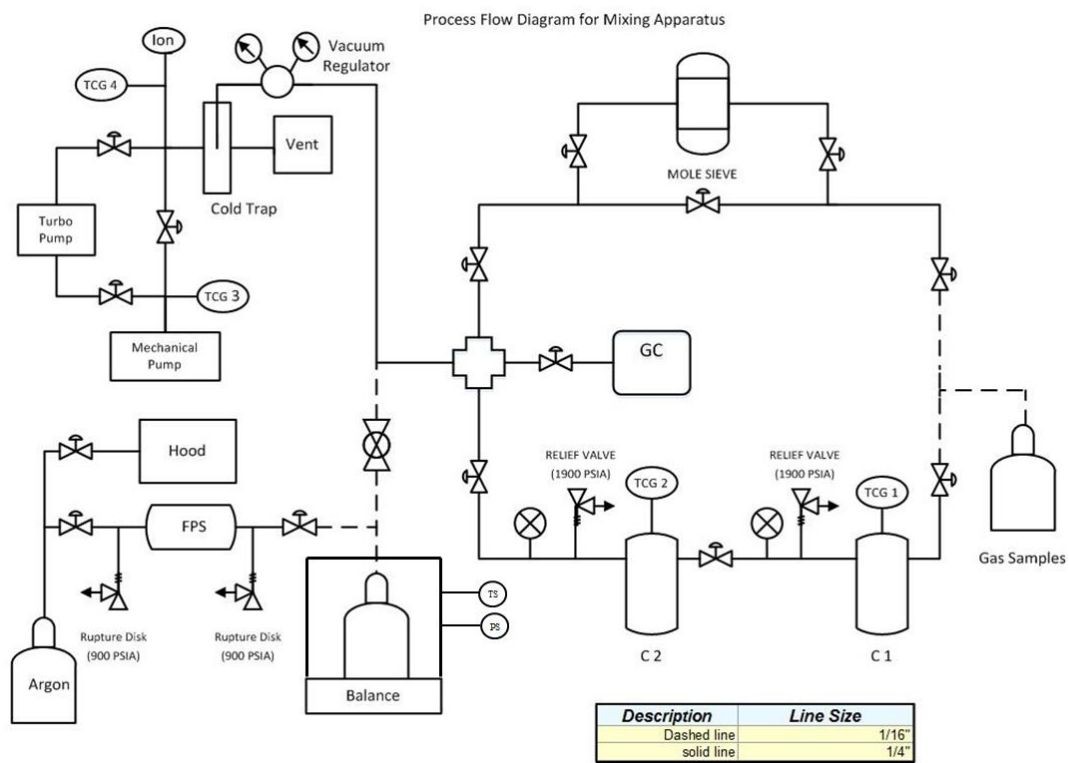


Figure 43. Process flow diagram of the in-house mixing apparatus

To create the mixtures, sample cylinders (Catalina I150 cylinder) were placed inside the acrylic box where temperature and pressure were monitored for compensation of air buoyancy effects. Next, the cylinders were evacuated with the mechanical pump for at least 24 hours, followed by evacuation using the turbo pump until pressures reached $\sim 10^{-4}$ - 10^{-5} Torr. The apparatus lines were purged at pressures of 300 psi and subsequently discharged to 50 psi using the component to be loaded. The lines were purged twice. The lighter component is loaded first followed by the heavier component to assist mixing for a uniform composition. Masses, compositions, and uncertainties of the mixtures are reported in Table 4.

Once the mixtures were made, the cylinder bottoms were heated with resistive tape while the top was cooled by placing a bag of ice around the top of the cylinder to induce mixing by convection. This process was repeated three times to ensure that the components mixed and that there was a uniform composition throughout the cylinder.

3.3.2. 75% Methane + 25% helium

Figure 44 shows the relative deviations of the measured densities from the EoS predictions of GERG 2008 [57] and AGA8-DC92 [58] for the 75% methane mixture at temperatures of 303, 350, 396 and 450 K. The measured p - ρ - T values appear in Table G.5 in Appendix G.

Table 4. Mixture masses, compositions and uncertainty

<i>sample</i>	m_{CH_4}/g	m_{He}/g	x_{CH_4}	x_{He}	$U(x)$
75% Methane - 25% Helium	957.1	77.6	0.75485	0.24515	0.00024
45% Methane - 55% Helium	981.8	294.6	0.45399	0.54601	0.00009
25% Methane - 75% Helium	409.4	302.7	0.25232	0.74768	0.00008

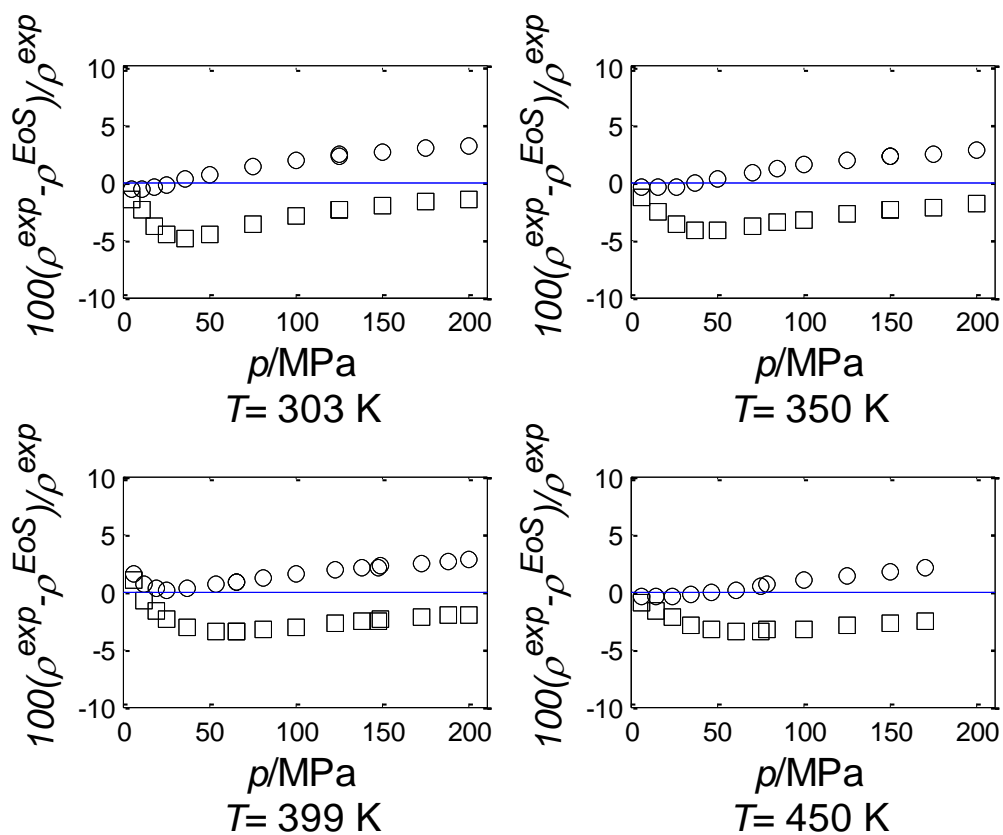


Figure 44. Relative deviations of measured densities from \square GERG-2008 [57] and \circ AGA8-DC92 [58] for methane ($x \approx 0.75$) + helium mixtures at 303 K, 350 K, 396 K and 450 K

3.3.3. 45% Methane + 55% helium

Figure 45 shows the relative deviations of the measured densities from the EoS predictions of GERG 2008 [57] and AGA8-DC92 [58] for the 45% methane mixture at temperatures of 303, 350, 398 and 450 K. The measured p - ρ - T values appear in Table G.6 in Appendix G.

3.3.4. 25% Methane + 75% helium

Figure 46 shows the relative deviations of the measured densities from the EoS predictions of GERG 2008 [57] and AGA8-DC92 [58] for the 25% methane mixture isotherms at temperatures of 303, 350, 397 and 450 K. The measured p - ρ - T values appear in Table G.7 in Appendix G.

The GERG 2008 EoS over-predicts the densities throughout the entire range peaking around 70 MPa then improving slightly. The largest deviation for all the mixtures was observed with the methane 50% + helium 50% mixture. The predictions improved with increasing temperatures.

At pressures up to 20 MPa, AGA8-DC92 predicts densities within 0.5 %, however larger deviations occur at high pressures. Deviations also increased as the helium content increased and as temperatures decreased. The uncertainty analysis for all the mixtures is presented below in Table 5.

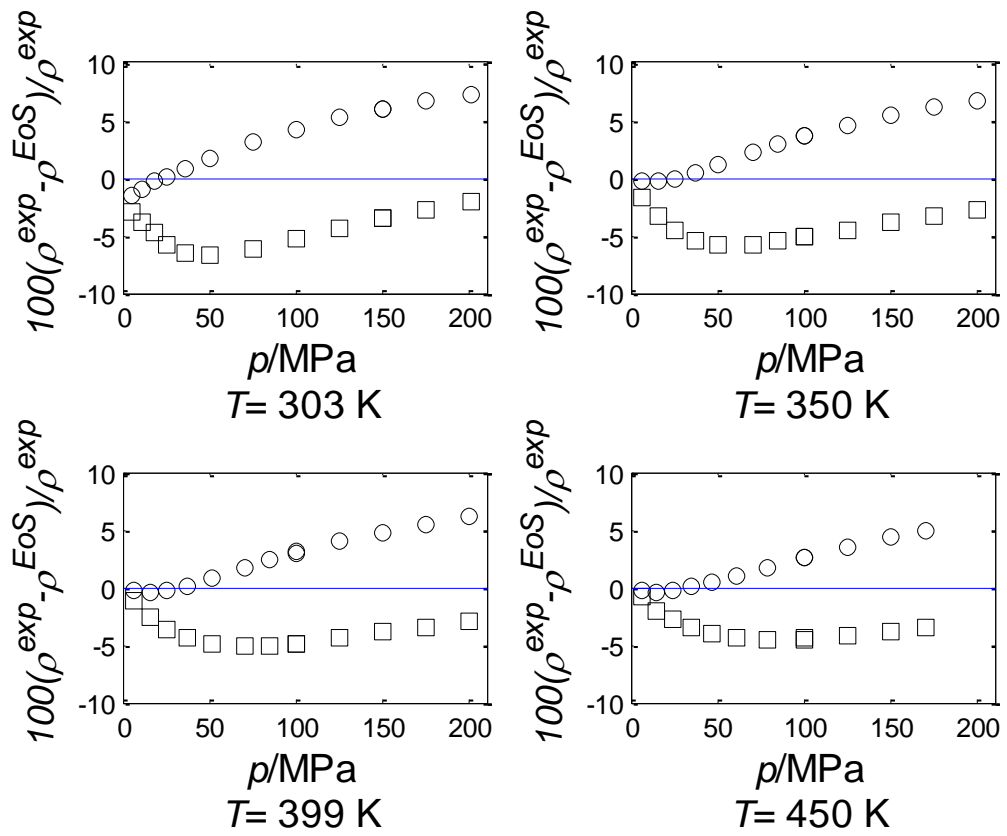


Figure 45. Relative deviations of measured densities from \square GERG-2008 [57] and \circ AGA8-DC92 [58] for methane ($x \approx 0.45$) + helium mixture at 303 K, 350 K, 398 K and 450 K

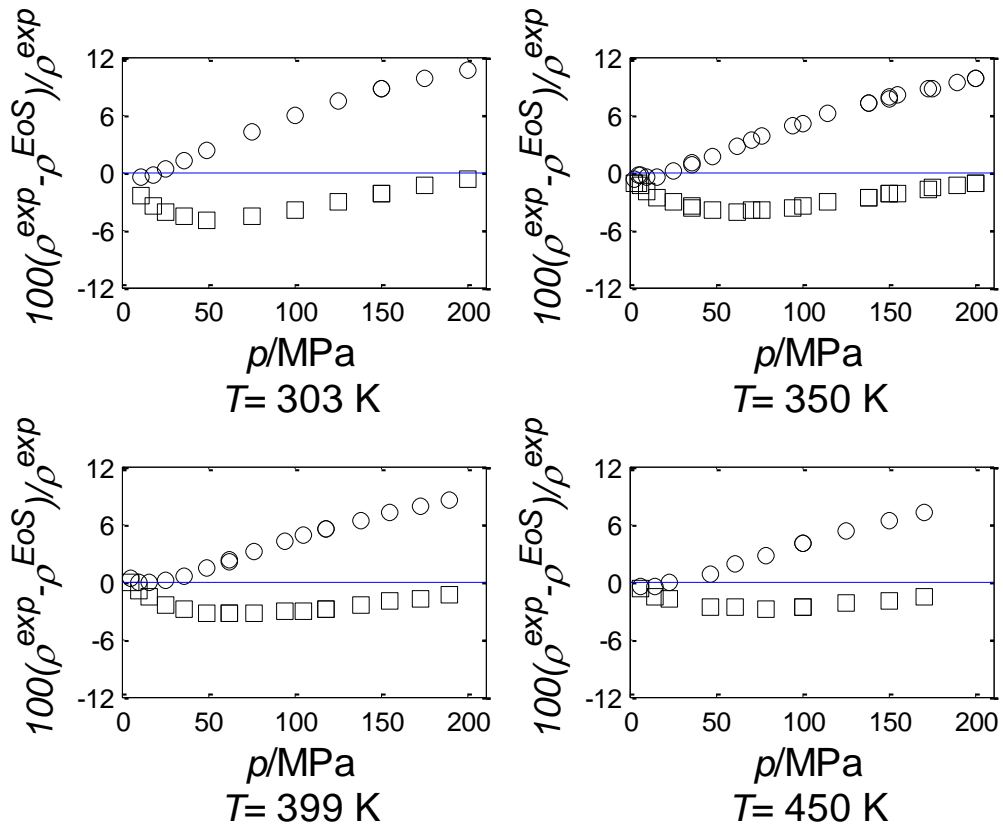


Figure 46. Relative deviations of measured densities from \square GERG-2008 [57] and \circ AGA8-DC92 [58] for methane ($x \approx 0.25$) + helium mixture at 303 K, 350 K, 397 K and 450 K

Table 5. Methane + helium measurement uncertainties

term	<u>coefficients</u>			density equivalent kg·m ⁻³
	expanded uncertainty (95% confidence limit)	derivative	source	
apparatus, $U(\rho)^{\text{app}}$	0.07 kg/m ³			0.07
temperature, $U(T)$	10 mK	$\left(\frac{\partial \rho}{\partial T}\right)_{P,m_i}$	EoS	0.001-0.019
pressure, $U(p)$	0.0207 MPa (HPT) 0.004 MPa (LPT) ^a	$\left(\frac{\partial \rho}{\partial p}\right)_{T,m_i}$	EoS	0.011-0.051
composition, $U(x)$	0.00008-0.00024	$\left(\frac{\partial \rho}{\partial x}\right)_{T,P}$	EoS	0.006-0.051

^a The Paroscientific[®] transducer accuracies specified by the manufacturer is $\pm 0.0001 \cdot p_{\text{max}}$, in which p_{max} is 41.3 MPa and 206.8 MPa for the low (LPT) and high (HPT) pressure transducers, respectively

3.3.5. Replicate mixtures

Replicate mixtures of similar composition were made and measured at 303 K to verify the reproducibility of the measurements. Sample compositions differed slightly because of limited helium supply during mixture construction but still provided a qualitative comparison. The masses, compositions, and uncertainties of the replicate mixtures appear in Table 6.

Figure 47-49 show the relative deviations of the densities measured for the replicate mixtures at 303 K from the EoS predictions of GERG 2008 [57] and AGA8-DC92 [58]. Mixtures and their respective replicates exhibit similar behavior validating the measurements and compositions. The measured p - ρ - T values appear in Tables G.8-10 in Appendix G.

Figure 50, which shows relative deviations of the measured densities from predictions of the AGA8-DC92 EoS, compares the current results with those reported by Hernández-Gómez *et al.* [55] for an approximately equimolar methane + helium mixture at 299 K. Their mixtures differ in mole fraction from the current equimolar mixture by 0.00068. AGA8-DC92 was chosen for the comparison because deviations are smaller than those for GERG 2008. The two sets agree within the combined experimental uncertainties.

Table 6. Replicate mixture masses, compositions and uncertainty

<i>Sample</i>	m_{CH_4}/g	m_{He}/g	x_{CH_4}	x_{He}	$U(x)$
73% Methane - 27% Helium	1395.7	129.3	0.72921	0.27079	0.00015
50% Methane – 50% Helium	973.9	243.5	0.49945	0.50055	0.00011
27% Methane - 73% Helium	414.3	287.3	0.26460	0.73540	0.00012

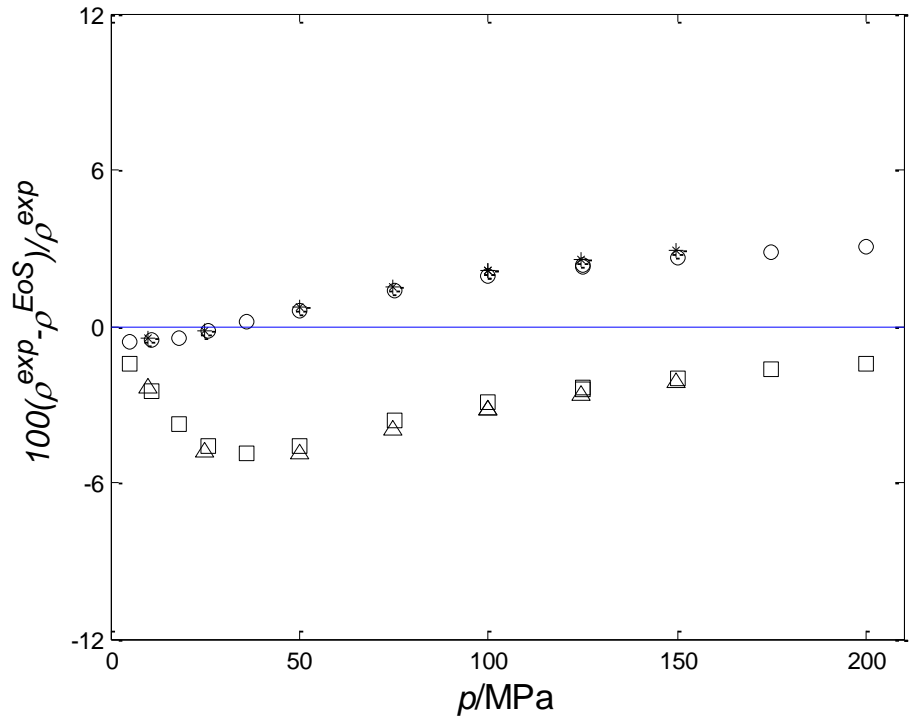


Figure 47. Relative deviations of measured densities from GERG-2008 [57] for □ methane ($x \approx 0.75$) + helium and Δ methane ($x \approx 0.73$) + helium and from AGA8-DC92 [58] for ○ methane ($x \approx 0.75$) + helium and * methane $x \approx 0.73$) + helium at 303 K

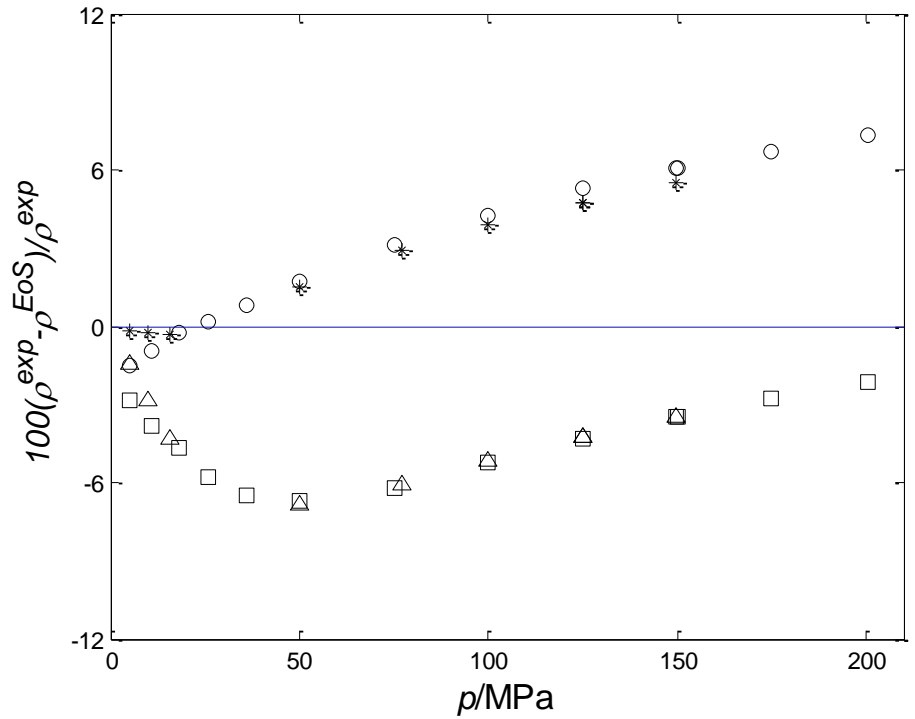


Figure 48. Relative deviations of measured densities from GERG-2008 [57] for □ methane ($x \approx 0.55$) + helium and Δ methane ($x \approx 0.50$) + helium and from AGA8-DC92 [58] for ○ methane ($x \approx 0.55$) + helium and * methane ($x \approx 0.50$) + helium at 303 K

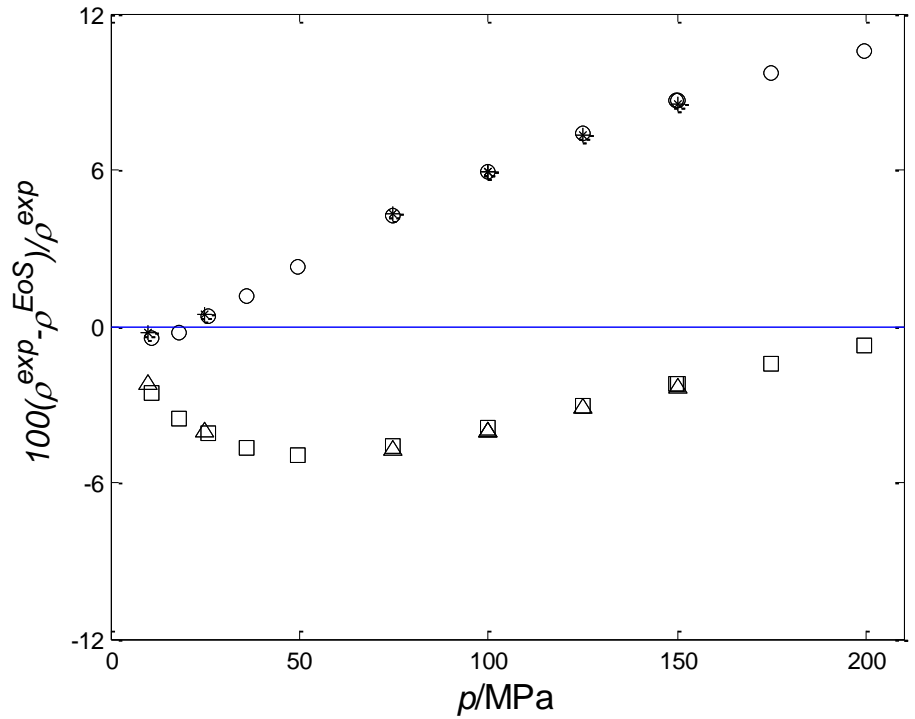


Figure 49. Relative deviations of measured densities from GERG-2008 [57] for \square methane ($x \approx 0.25$) + helium and Δ methane ($x \approx 0.26$) + helium and from AGA8-DC92 [58] for \circ methane ($x \approx 0.25$) + helium and $*$ methane ($x \approx 0.26$) + helium at 303 K

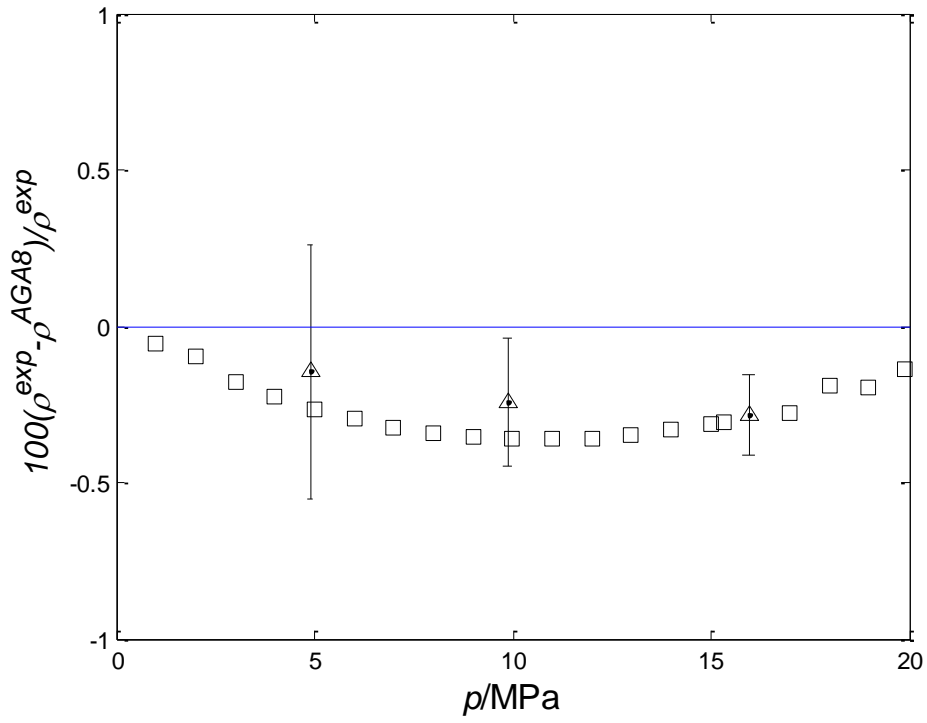


Figure 50. Relative deviations of measured densities from AGA8-DC92 for methane ($x \approx 0.50$) + helium sample for this work Δ 303 K and Hernández-Gómez *et al.* [55] \square 299 K

4. MIXING RULE BASED UPON RESIDUAL HELMHOLTZ ENERGY

There are many remarkably accurate EoS for pure fluids for a wide range of temperatures and pressures, but this is not the case for mixtures. Unlike the pure fluids, no statistical mechanics solution relating these thermophysical properties and their molecular interactions exists [77]. Empirical models do exist that try to relate these properties using a mixture of classical models, statistical mechanics, and observable variables.

In the following sections, the classical and statistical mechanical models in the form of the virial EoS will be discussed. An equation created by Groupe Européen de Recherches Gazières (GERG) [57, 65] will be described in detail because there are similarities to our approaches. Our method is based upon classic principles and the residual Helmholtz energy. Finally, fits of p - ρ - T data for multiple binary mixtures using our approach are discussed and compared to GERG.

4.1. Mixing rules of a virial equation

The virial EoS is defined as the compressibility factor expressed as a power series in terms of pressure or density with coefficients that are functions of only temperature and composition (in the case of mixtures). Typically for lower densities the series is truncated after the third virial coefficient term. The general model (4.1) and the truncated version (4.2) are:

$$Z = 1 + \sum_{i=2}^N B_i(x, T) \rho^i \quad (4.1)$$

$$Z = 1 + B\rho + C\rho^2 \quad (4.2)$$

in which the i^{th} coefficient (B_i) theoretically represents i -body interactions among molecules when the density/pressure is sufficiently large for those interactions to occur. For example, the second virial coefficient (B) represents all the pair-wise interactions, the third virial coefficient (C) represents all the ternary interactions, *etc.*

Each coefficient in Equation 4.1 is defined as the limit as the density goes to zero of the $(i-1)$ derivative of the compressibility factor with respect to density.

$$B_i = \frac{1}{(i-1)!} \left[\frac{\partial^{i-1} Z}{\partial \rho^{i-1}} \right]_{\rho=0} \quad (4.3)$$

Statistical mechanics shows that the compositional and temperature dependencies of the second and third virial coefficients in can be separated. The form for the second virial is

$$B = \sum_i^N \sum_j^N x_i x_j B_{ij} \quad (4.4)$$

An alternate form is:

$$B = \sum_j^N x_i B_{ii} + \sum_i^N \sum_{j=i+1}^N x_i x_j (2B_{ij} - B_{ii} - B_{jj}) = \sum_j^N x_i B_{ii} + \sum_i^N \sum_{j=i+1}^N x_i x_j \delta B_{ij} \quad (4.5)$$

in which the first term represents the ideal solution contribution (molar average of the pure fluid values) and the second term, the deviation from ideality caused by interactions between unlike molecules.

The form for the third virial coefficient is

$$C = \sum_i^N \sum_j^N \sum_k^N x_i x_j x_k C_{ijk} \quad (4.6)$$

McGregor *et al.* [78] proposed a simple approximation that yields a quadratic form similar to equation 4.5:

$$C = \sum_j^N x_j C_{jjj} + \sum_i^N \sum_{j=i+1}^N x_i x_j \delta C_{ij} \quad (4.6)$$

With

$$\delta C_{ij} = 3C_{ijj} - 2C_{iii} - C_{jjj} = 3C_{ijj} - 2C_{jjj} - C_{iii}$$

The approximation is the assumption that

$$3C_{ijj} - 2C_{iii} - C_{jjj} \cong 3C_{ijj} - 2C_{jjj} - C_{iii}$$

This approximation described the experimental third virial coefficient for the mixtures considered by McGregor *et al.* [78] within the experimental uncertainty.

Current modified versions of the virial form do exist in EoS as AGA8-DC92 [58], Benedict-Webb-Rubin (BWR) and modified BWR [79], although they lack some of the benefits and extrapolation capabilities of the fundamental equations such as Helmholtz energy-based models.

4.2. Mixing rule based upon residual Helmholtz free energy

EoS using temperature and density as independent variables are much more convenient for describing fluid physics than are EoS with other choices of independent variables. The fundamental function which has these as the natural independent variables

is the Helmholtz energy. This section describes mixing rules based upon classical rules such as the virial EoS and their extension to empirical models based upon the residual Helmholtz energy.

Finally, a model based upon a rational/polynomial form of the binary interaction Helmholtz energy is explored for mixtures containing nitrogen, methane, ethane, carbon dioxide, helium, argon and krypton using p - ρ - T data. These components were chosen to provide a first step in building mixing rules and to identify the form of the interaction function for simple nonpolar fluids. All fits use a least square regression (Levenberg-Marquardt) routine available in MATLAB R2013b.

4.2.1. GERG mixing rules

Because the second virial coefficient is the leading term in the residual Helmholtz energy for the virial EoS from, quadratic mixing has been extended to the residual Helmholtz energy for models such as the one proposed by GERG. This equation was created in 2004 by Kunz *et al.* [65] and then improved by adding additional mixtures in 2008 [57]. The EoS is one of the most accurate for natural gas-like mixtures and contains 21 components in the model. GERG is defined in terms of dimensionless Helmholtz energy with ideal gas and residual terms:

$$\frac{A_m(\rho, T, x)}{RT} = \alpha_m(\rho, T, x) = \alpha_m^o(\rho, T, x) + \alpha_m^r(\delta, \tau, x) \quad (4.7)$$

With the reducing parameters defined as follows;

$$\delta = \frac{\rho}{\rho_r(x)}$$

$$\tau = \frac{T_r(x)}{T}$$

These reducing parameters are a combination between a Lorentz/Berthelot combining rules and the excess Gibbs energy function described by van Laar [80].

$$\frac{1}{\rho_r(x)} = \sum_{i=1}^N \sum_{j=1}^N x_i x_j \beta_{v,ij} \gamma_{v,ij} \frac{x_i + x_j}{\beta_{v,ij}^2 x_i + x_j} \frac{1}{8} \left(\frac{1}{\rho_{c,i}^{1/3}} + \frac{1}{\rho_{c,j}^{1/3}} \right)^3 \quad (4.8)$$

$$T_r(x) = \sum_{i=1}^N \sum_{j=1}^N x_i x_j \beta_{T,ij} \gamma_{T,ij} \frac{x_i + x_j}{\beta_{T,ij}^2 x_i + x_j} (T_{c,i} \cdot T_{c,j})^{1/2}$$

These were proposed by Tillner-Roth and Klimeck and contain four fit parameters. The ideal gas contribution is:

$$\alpha_m^o(\rho, T, x) = \sum_{i=1}^N x_i \left[\alpha_{oi}^o(\rho, T) + \ln x_i \right] \quad (4.9)$$

in which α_{oi}^o is calculated from the ideal-gas heat capacity.

The residual term, (α_m^r) is defined with quadratic composition dependence similar to the second virial coefficient;

$$\alpha_m^r(\delta, \tau, x) = \sum_{i=1}^N x_i \alpha_{oi}^r(\delta, \tau) + \sum_{i=1}^{N-1} \sum_{j=i+1}^N x_i x_j F_{ij} \alpha_{ij}^r(\delta, \tau) \quad (4.10)$$

in which the first term describes the “idea solution” contribution using the residual Helmholtz energy of the pure substance (α_{oi}^r) and the second term, or the departure function, accounts for the departure from ideality.

The parameter F_{ij} is determined by fitting specific binary mixture data, or set equal to zero in the absence of reliable data. For the interaction parameter (α_{ij}^r), the form is either that of equation 4.11 for a specific binary system or in a general form (equation 4.12) as determined by Lemmon and Jacobsen [81] for mixtures insufficient data.

$$\alpha_{ij}^r(\delta, \tau) = \sum_{k=1}^M n_k \delta^{dk} \tau^{tk} + \sum_{k=1}^M n_k \delta^{dk} \tau^{tk} \exp\left[-(\delta - \varepsilon_k)^2 - (\delta - \gamma_k)\right] \quad (4.11)$$

$$\alpha_{gen}^r(\delta, \tau) = \sum_{k=1}^{10} n_k \delta^{dk} \tau^{tk} \quad (4.12)$$

where n_k , dk , tk , γ_k , and ε_k are numerical parameters.

GERG fit binary specific equations in the form of equation 4.11 for seven mixtures and defined eight other mixtures using the general form as shown in equation 4.12. For all other mixtures only the first terms in equation 4.10, (α_{oi}^r) are used. Figure 51 provides an overview of various mixtures and the types of rules used to describe them in GERG.

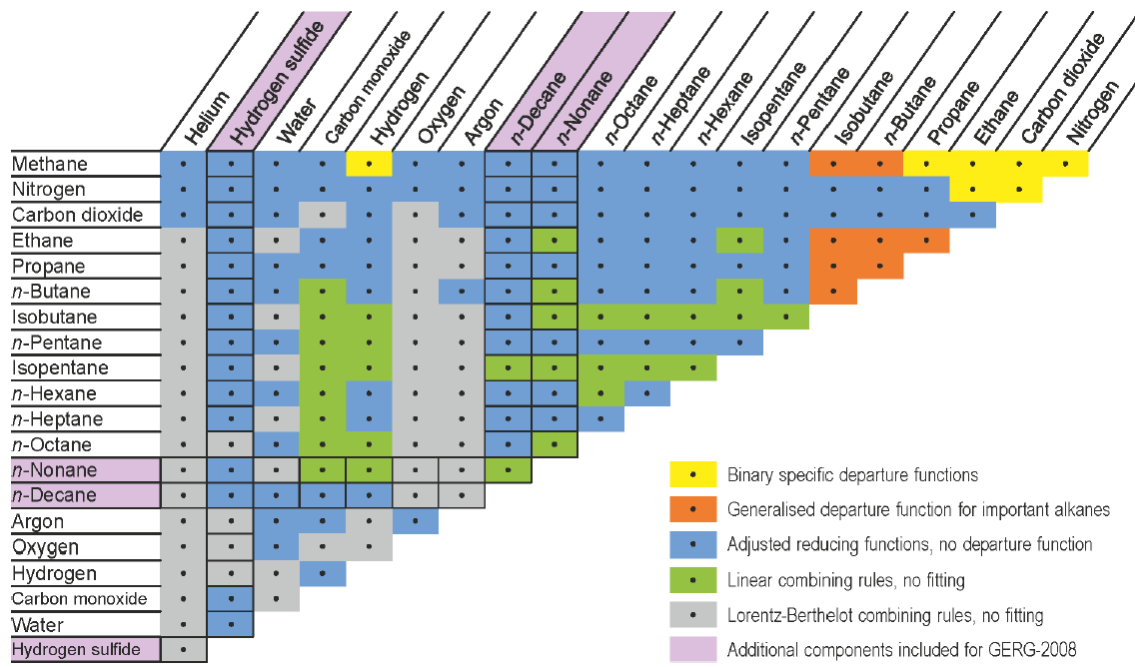


Figure 51. Overview of the mixtures included in GERG [57]

These models have great predictive capabilities, typically within $\Delta\rho/\rho = \pm 0.1\%$ at pressures up to 30 MPa for substances experimental binary mixture data exist. However, there is cause for concern because the pure terms in the residual (α_{oi}^r) appear to be calculated at the reduced temperature and pressure of the mixtures rather than at their respective reduced parameters. As a result, these functions are evaluated at molar densities and temperatures different from the mixtures. An added complication is that the critical temperature and density of the mixture are required, but they usually are not known and must be approximated.

4.2.2. Interaction residual Helmholtz energy based upon a polynomial (rational) form

This work considered two approaches to the mixing rules, excess property and residual function. This document focuses on the residual function approach because it has fewer limitations than the excess property. Only “simple”, non-polar molecules in the vapor/gas phase or supercritical region above either component’s pure critical temperature were investigated. This was done to start building a base model for the residual interaction Helmholtz energy. Future work should build upon the base model and add terms to describe other states such as compressed liquid, super-critical fluid and more complex fluids such as polar molecules.

The excess property is appealing because its overall contribution is smaller than that of the residual functions. Because it is a smaller contribution, the fit can tolerate slightly higher uncertainties without affecting the property calculation greatly. An excess

property is defined as the difference between the real mixture property and the same property of an ideal solution at the same values of the independent variables. If we choose a property, θ with independent variables of temperature, density and composition (can also be done with pressure instead of density), the excess of the property will be [80]:

$$\theta^e(T, \rho, x) = \theta_m(T, \rho, x) - \theta_m^{IS}(T, \rho, x) \quad (4.13)$$

Here, subscript m denotes a real mixture property, superscript e denotes the excess property when density is the independent variable, and superscript IS denotes an ideal solution property. Using the residual function definition, we can replace the real mixture property by:

$$\theta_m(T, \rho, x) = \theta_m^r(T, \rho, x) + \theta_m^{IG}(T, \rho, x) \quad (4.14)$$

Here superscript IG denotes an ideal gas property. The excess property becomes:

$$\theta^e(T, \rho, x) = \theta_m^r(T, \rho, x) + \theta_m^{IG}(T, \rho, x) - \theta_m^{IS}(T, \rho, x) \quad (4.15)$$

Combining the ideal solution and ideal gas terms yields:

$$\theta^e(T, \rho, x) = \theta_m^r(T, \rho, x) - \sum_i x_i \theta_i^r(T, \rho) \quad (4.16)$$

Or for Helmholtz energy

$$A^e(T, \rho, x) = A_m^r(T, \rho, x) - \sum_i x_i A_i^r(T, \rho) \quad (4.17)$$

However, an issue arises with how to approach the residual property of the mixture since it is lacking observable variables and would require a fit. For this reason, we recommend using the residual Helmholtz energy, although the relationship between the excess and residual properties is useful for choosing model forms.

For the residual Helmholtz energy, this work builds a model based upon quadratic mixing of the residual Helmholtz energy, which can be broken down into an ideal and departure part similarly to McGregor *et al.* [78]

$$\begin{aligned}\alpha_m^r(\rho, T, x) &= \sum_i^K \sum_j^K x_i x_j \alpha_{ij}^r(\rho, T) \\ &= \sum_i^K x_i \alpha_{ii}^r(\rho, T) + \sum_i^K \sum_{j=i+1}^K x_i x_j (2\alpha_{ij}^r(\rho, T, x) - \alpha_{ii}^r(\rho, T) - \alpha_{jj}^r(\rho, T))\end{aligned}\quad (4.18)$$

Here n is the number of components in the mixture, the pure fluid values, α_{ii}^r , are calculated using the respective pure fluid reference equations, and the interaction residual Helmholtz energy (α_{ij}^r) is defined empirically.

A rational polynomial functional form has been used successfully by multiple authors to describe pure fluid behavior and interactions based upon pressure EoS [82-84], and more recently for residual Helmholtz energy [20], so the interaction residual Helmholtz energy is defined as

$$\alpha_{ij}^r(\rho, T, x) = \frac{n_1 \rho + n_2 \rho^2 + \dots + n_N \rho^N}{1 + n_{N+1} \rho + n_{N+2} \rho^2 + \dots + n_{N+L} \rho^L}\quad (4.19)$$

The coefficients contain temperature and compositional dependence:

$$n_i = f(T, x) = f(T) + f(x)$$

The temperature dependent term is a polynomial in inverse temperature. The composition dependence is required describe most of the mixtures at high, “liquid-like” densities. Because the interaction term is the only one that is a function of composition, this dependence must be added to the coefficients for our model. Forms similar to the

excess Gibbs energy models were used because they are related to the residual Helmholtz energy as already explained.

Because experimental values of the residual Helmholtz energy cannot be calculated directly from p - ρ - T measurements, the following relationship between the derivative of residual Helmholtz energy and the compressibility factor was used

$$\frac{1}{RT} \frac{\partial A_i^r}{\partial \rho} = \alpha_{\rho,i}^r = \frac{Z_i - 1}{\rho} \quad (4.20)$$

Here, $a_{r,i}^r$ denotes the partial derivative of a^r with respect to density at constant temperature and composition for substance. Applying this to equation 4.18 for a binary mixture yields:

$$a_{r,m}^r(r, T, x) = x_1 a_{r,11}^r(r, T) + x_2 a_{r,22}^r(r, T) + x_1 x_2 \left[2a_{r,12}^r(r, T, x) - a_{r,11}^r(r, T) - a_{r,22}^r(r, T) \right] \quad (4.21)$$

or

$$\frac{Z_m - 1}{r} = x_1 \frac{Z_1 - 1}{r} + x_2 \frac{Z_2 - 1}{r} + x_1 x_2 \left[2a_{r,12}^r(r, T, x) - \frac{Z_1 - 1}{r} - \frac{Z_2 - 1}{r} \right]$$

Rearranging for the interaction residual Helmholtz energy yields:

$$2\alpha_{\rho,12}^r(\rho, T, x) = \frac{\frac{Z_m - 1}{\rho} - x_1 \frac{Z_1 - 1}{\rho} - x_2 \frac{Z_2 - 1}{\rho}}{x_1 x_2} + \frac{Z_1 - 1}{\rho} + \frac{Z_2 - 1}{\rho} \quad (4.22)$$

in which

$$\alpha_{\rho,12}^r(\rho, T, x) = \frac{(1 + n_{N+1}\rho + \dots + n_{N+L}\rho^L)(n_1 + \dots + N \cdot n_N \rho^{N-1}) - (n_1 \rho + \dots + n_N \rho^N)(n_{N+1} + \dots + L \cdot n_{N+L} \rho^L)}{(1 + n_{N+1}\rho + \dots + n_{N+L}\rho^L)^2}$$

Pure species properties were estimated using their respective reference equations for methane [85], ethane [86], nitrogen [47], carbon dioxide [48], argon [49], helium [50],

hydrogen [87], and krypton [88]. The reference equations for methane [30], ethane [31], nitrogen [32], carbon dioxide [33], and argon (section 3) have been shown to be accurate within at worst $\Delta\rho / \rho = \pm 0.05\%$.

For helium, the EoS deviations from the experimental densities were larger (shown in section 3); however, the impact on the derivative of the residual Helmholtz energy term is minimal. A correction technique was tested however its impact on the fits was lower than the overall uncertainties so the reference equation was used directly. For hydrogen and krypton, there is no experimental verification of their respective reference equations, so these fits results should be taken with some caution.

The boundary condition for the second virial coefficient (4.3) was applied to equation 4.18. This gives physical meaning to the coefficients and anchors the low-density region. This boundary condition leads to the first coefficient being the interaction second virial coefficient (*i.e.*, $n_1 = B_{12}$) Values for B_{12} were estimated from REFPROP [89] over the entire experimental temperature range for the specific data set. Calculated values were compared to experimental values to test the equation validity. If the two did not match, the parameter was left as a fitted parameter. Remaining coefficients were found by least squares regression of binary p - ρ - T data.

Data sets considered in GERG [65] plus the following three sets [19, 84, 90] were considered in the fitting procedures. A special thanks to Dr. Eric Lemmon at NIST Boulder for accumulating and sharing these data. For data selection, the following criteria were applied to determine if the data set was to be included in the fit or not:

- Comparison of prediction using GERG/inclusion in the GERG model

- The interaction term (α_{ij}^r) was similar to others in the specific binary set and smooth when using the quadratic assumption
 - Uncertainty of the experimental values was not too large ($\Delta\rho/\rho = \pm 1.00\%$)
 - Measured temperatures were above either pure component's critical temperature
- The mixture data sets as a whole should span most of the compositional range,

however, such data are rare.

4.2.3. Fit results

The general form of the interaction residual Helmholtz energy used for most unlike pair interactions is

$$\frac{A_{12}^r(\rho, T)}{RT} = \frac{n_1\rho + n_2\rho^2 + n_3\rho^3}{1 + n_4\rho} \quad (4.23)$$

with

$$n_1 = B_{12}$$

$$n_{k+1} = c_{0,k} + c_{1,k}/T + c_{2,k}/T^2 + c_{3,k}x_1x_2(c_{4,k}x_1 + x_2)$$

Some unlike interactions required more complex composition dependence.

Density powers up to sixth order were tested because of systematic density deviations for some mixtures, however these did not improve the fit. The systematic trends most likely come from inaccuracies in the reference equations and experimental measurements.

For the temperature dependence in the coefficients, a quadratic form of the inverse of temperature was sufficient for most mixtures tested, although higher powers were tested.

The parameters in equation 4.23 do not vary with composition for methane + nitrogen, nitrogen + carbon dioxide, and methane + ethane mixtures. For the other mixtures, the following forms were tested: van Laar, Redlich/Kister expansion [80], and Margules power series expansion [91]. All of these models yield similar results. The Margules form performs slightly better, so it was chosen for the model..

In most cases, the composition dependence appears only in n_2 . For interactions involving helium, n_4 also shows the same dependence.

The following sections present the results for the mixtures starting with the cases which have no composition dependence in the coefficients. Then, mixtures composition dependences will be discussed. Finally the most complex cases, helium mixtures, will be presented. The general model in equation 4.23 is used as the basis for these discussions, although some mixtures models were simpler while others were more complex. For each binary mixture, the full model and coefficients values appear in Appendix H.

4.2.3.1 No composition dependence of interaction residual Helmholtz energy

For some mixtures, the coefficients n_i in equation 4.23 are independent of composition, so that $c_{3,k} = c_{4,k} = 0$ for all k . Of the binary systems investigated in this work, this occurs for methane + nitrogen, methane + ethane, and nitrogen + carbon dioxide.

Methane + nitrogen

Table 7 displays the temperature, pressure and composition ranges used for the fits, while Figure 52 shows the results of the fit. Most of the deviations are within $\Delta Z/Z = \pm 0.1\%$, except for those of Achtermann *et al.* [92]. Their data exhibit systematic tendencies, but the reported uncertainty of these results is as high as $\Delta Z/Z = \pm 0.4\%$. As a result, the systematic tendencies are not statistically significant.

Attempts to eliminate the systematic tendencies by adding higher order density terms were unsuccessful. Because the fit is within the experimental uncertainties, major efforts were not spent trying to correct this. One possible explanation is that these errors could be coming from the reference equations themselves, which are included in the fitting procedures.

Figure 53 compares equation 4.23 with GERG. Both equations predict the data well with GERG doing slightly better at lower densities. Note that GERG has many more parameters (more than 25 compared to 8) and a more complex form that contains exponential terms in density. It also shows a systematic trend for the Achtermann *et al.* [92] data, reinforcing the possibility that this trend is due to experimental errors.

Table 7. Methane + nitrogen mixture data used in the fit

Source	Symbol	Composition (mol CH ₄)	Temperature Range (K)	Pressure Range (MPa)
Gomez-Osorio <i>et al.</i> [19]	x	0.25-0.75	303-470 K	Up to 120 MPa
Chamorro <i>et al.</i> [36]	◇	0.80-0.90	240-400 K	Up to 20 MPa
Achtermann <i>et al.</i> [92]	□	0.13-0.90	323 K	Up to 10 MPa
Jaeschke <i>et al.</i> *	+	0.25-0.80	270-350 K	Up to 14 MPa
Brugge <i>et al.</i> *	* (red)	0.50	280-300 K	Up to 10 MPa
Distrigaz <i>et al.</i> *	□ (red)	0.50	283-293 K	Up to 7 MPa

*Full biographic details are available in GERG [65]

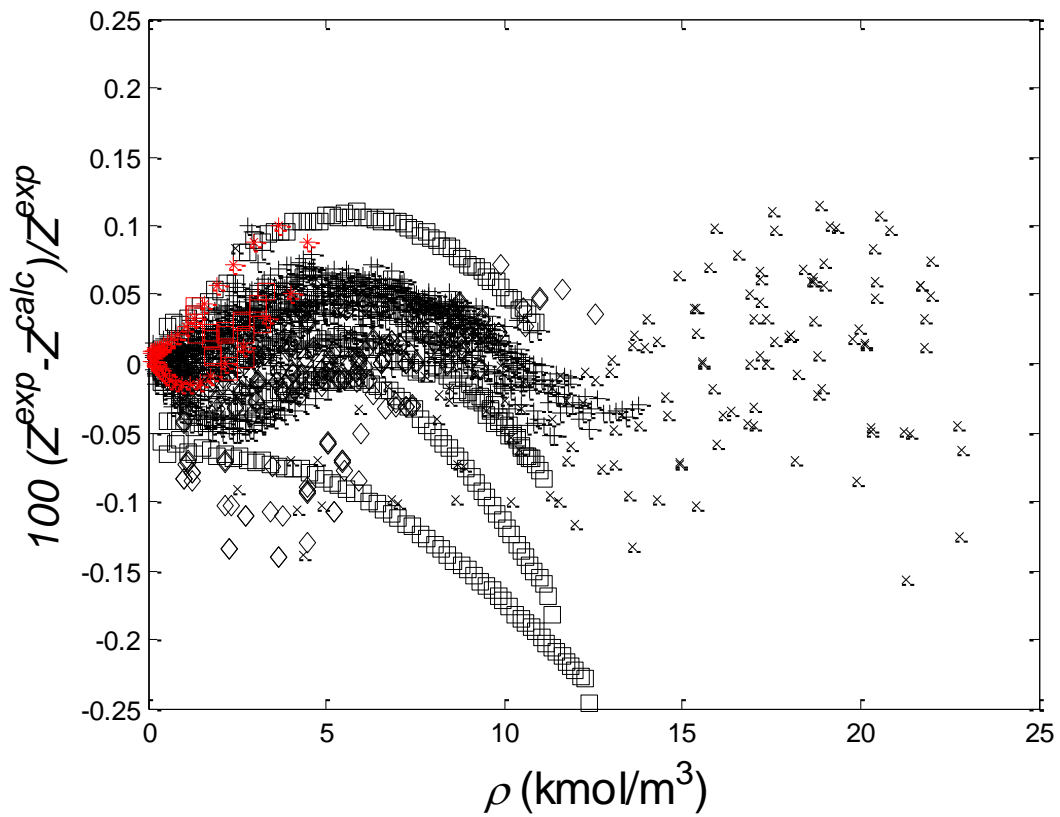


Figure 52. Relative deviation of the measured compressibility factors from the EoS predictions for methane + nitrogen mixtures

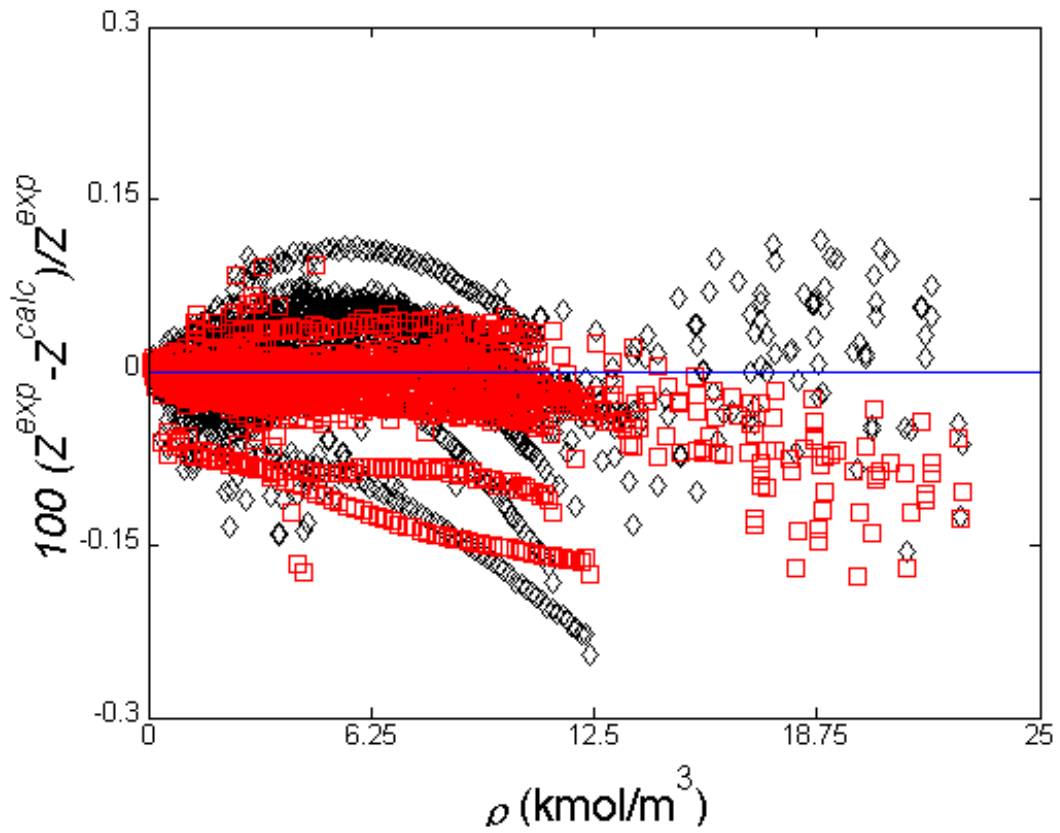


Figure 53. Relative deviation of the measured compressibility factors from the EoS predictions for methane + nitrogen mixtures: this work (\diamond), GERG (\square)

Methane + ethane

The data sets for the methane + ethane mixtures that were included in the fit are shown in Table 8, and the results of the fit in Figure 54. Most of the data fall within $\Delta Z/Z = \pm 0.1\%$ except for those of McElroy *et al.* [90], which have higher experimental uncertainties than the others ($\Delta Z/Z = \pm 0.2-0.6\%$). Because there appears to be no significant bias in the McElroy data, and because of its wider compositional range, these data were included in the fit. GERG excluded these data because their goal was to get the most accurate equation possible while ours is to develop a general model. Figure 55 compares equation 4.23 with GERG. Both equations have similar predictive capabilities, however, GERG requires more than 30 parameters.

Table 8. Methane + ethane mixture data used in the fit

Source	Symbol	Composition (mol CH ₄)	Temperature Range (K)	Pressure Range (MPa)
McElroy <i>et al.</i> [90]	x	0.27-0.70	313-343 K	Up to 10 MPa
Blanke <i>et al.</i> *	◇	0.75-0.95	312-333 K	Up to 7 MPa
Hou <i>et al.</i> *	□	0.30-0.70	320 K	Up to 7 MPa
Gasunie <i>et al.</i> *	+	0.80-0.95	308 K	Up to 6 MPa
Ruhrgas *	*	0.70-0.96	310-330 K	Up to 12 MPa

*Full biographic details are available in GERG [65]

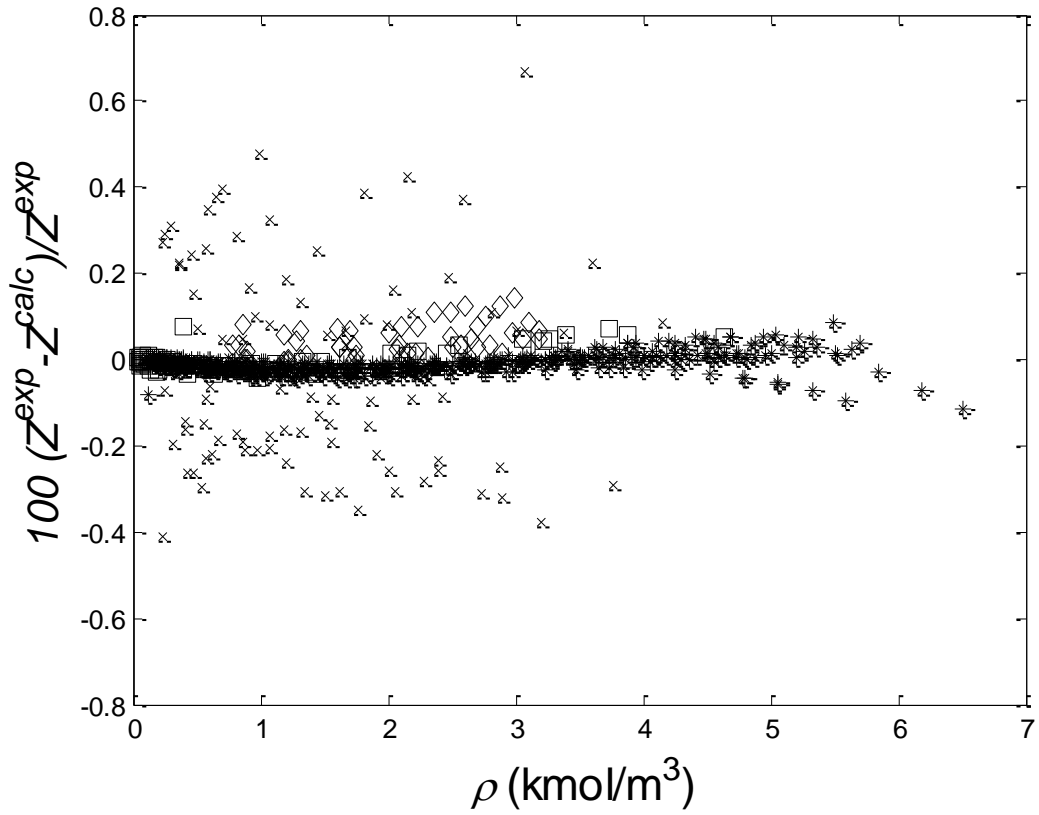


Figure 54. Relative deviation of the measured compressibility factors from the EoS predictions for methane + ethane mixtures

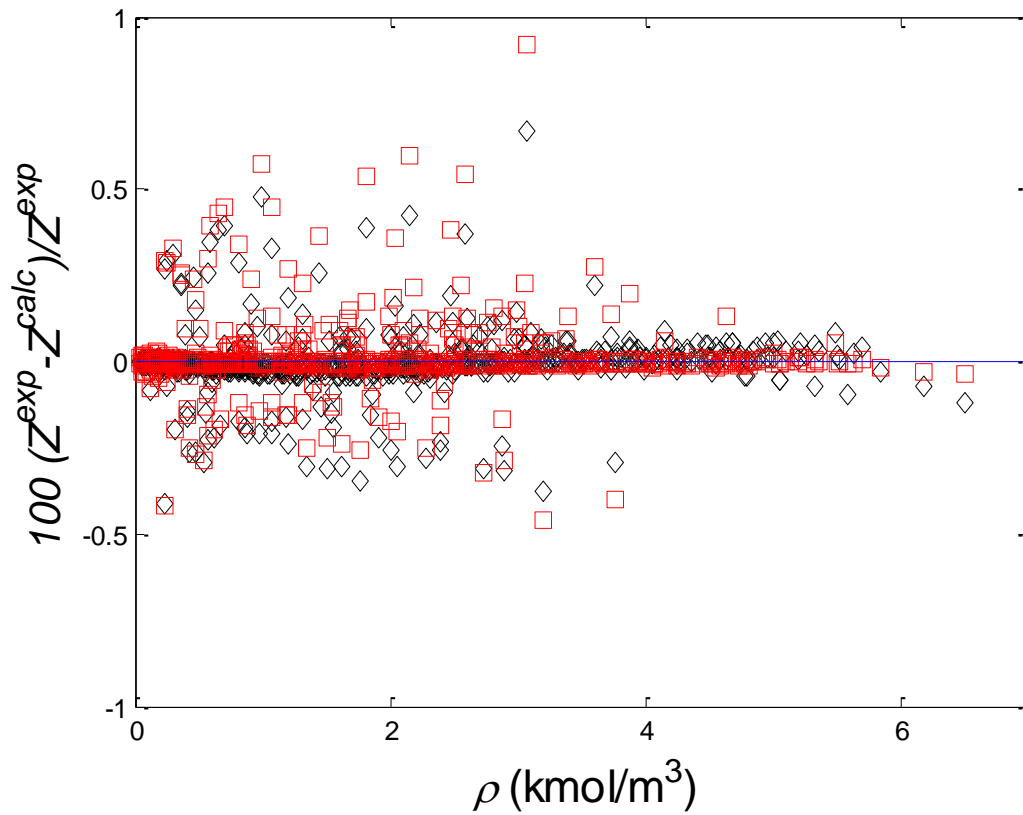


Figure 55. Relative deviation of the measured compressibility factors from the EoS predictions for methane + ethane mixtures: this work (\diamond), GERG (\square)

Nitrogen + carbon dioxide

The data sets for the nitrogen + carbon dioxide mixtures that were included in the fit are shown in Table 9, and the results of the fit in Figure 56. Most data can be predicted within $\Delta Z/Z = \pm 0.4\%$ except data near the critical temperature of carbon dioxide and at higher carbon dioxide compositions. There is some scatter at low-density values; however, this could be caused by lower experimental equipment resolution at lower densities causing larger deviations. Investigating the boundary condition of densities approaching zero, the interaction Helmholtz energy must equal the cross second virial coefficient. These points have similar scatter around the expected value, further giving proof that this could be an experimental effect rather than the fit.

Figure 57 compares equation 4.23 with the GERG model. GERG has a binary specific mixture model with more than 20 parameters for this binary system. GERG also shows systematic trends in the deviations near the critical point but theirs seems to be more off-center. This is somewhat surprising because the GERG model usually provides good results in this region.

Table 9. Nitrogen + carbon dioxide mixture data used in the fit

Source	Symbol	Composition (mol CO ₂)	Temperature Range (K)	Pressure Range (MPa)
Brugge <i>et al.</i> *	◇	0.11-0.91	320-450 K	Up to 70 MPa
Brugge <i>et al.</i> *	x	0.10-0.90	320 K	Up to 10 MPa
Esper <i>et al.</i> *	□	0.55	320 K	Up to 45 MPa

*Full biographic details are available in GERG [65]

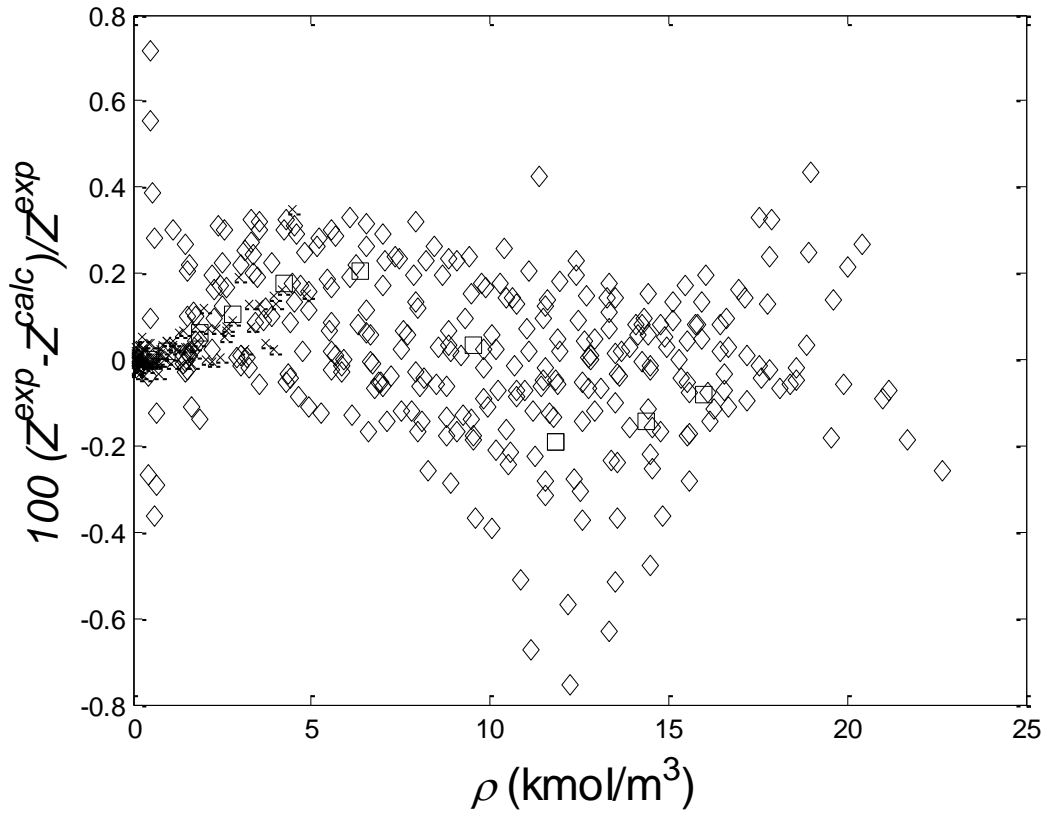


Figure 56. Relative deviation of the measured compressibility factors from the EoS predictions for nitrogen + carbon dioxide mixtures

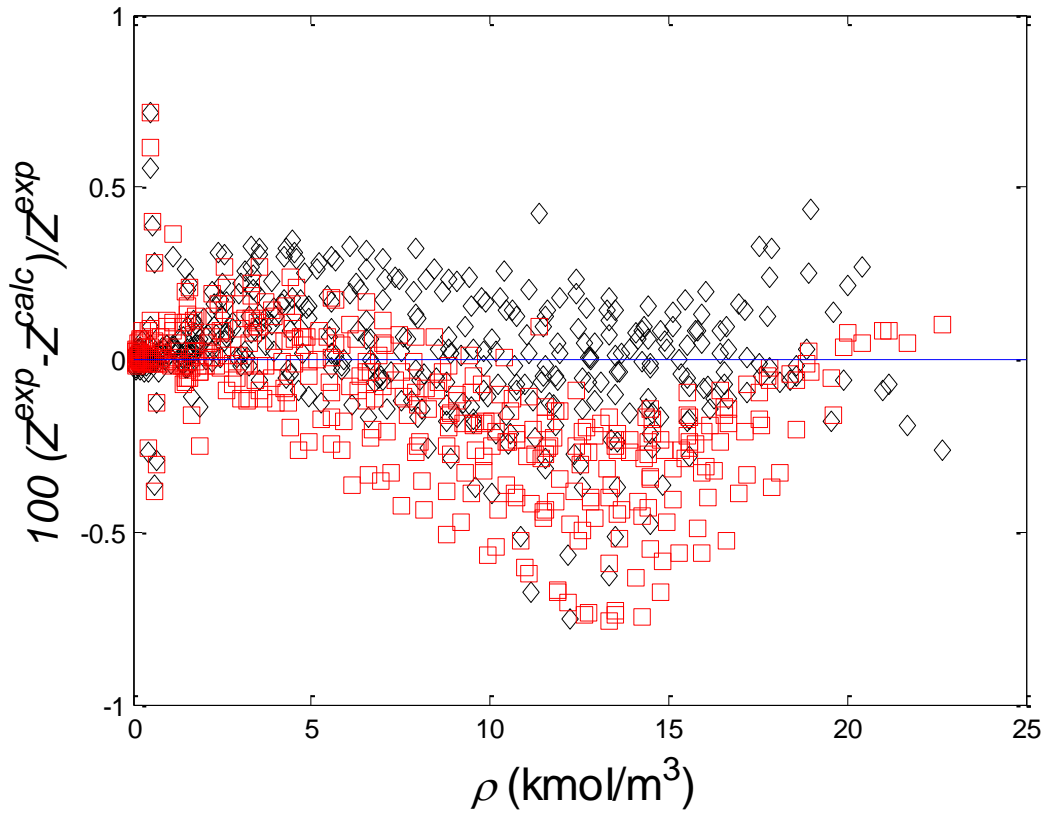


Figure 57. Relative deviation of the measured compressibility factors from the EoS predictions for nitrogen + carbon dioxide mixtures: this work (\diamond), GERG (\square)

4.2.3.2 Interaction residual Helmholtz energies with composition dependence

This section describes binary systems for which one or more of the coefficients in equation 4.23 vary with composition. Of the binary systems investigated in this work, this occurs for carbon dioxide + methane, carbon dioxide + ethane, nitrogen + argon, and nitrogen + hydrogen.

Methane + carbon dioxide

The data sets for the methane + carbon dioxide mixtures that were included in the fit are shown in Table 10, and the results of the fit in Figure 58. For this mixture, the model fits most of the data within $\Delta Z/Z = \pm 0.5\%$. Larger deviations do occur at the lower temperatures, 344 to 350 K. One possible explanation for this is that the fluid is still relatively near the critical region of the mixture making the behavior harder to predict.

Equation 4.23 has lower deviations than GERG (shown in Figure 59) at densities up to $12 \text{ kmol}\cdot\text{m}^{-3}$, but the opposite is true at higher densities. The improved description at higher densities is accomplished by including Gaussian bell terms in the model. Such terms have not been included in equation 4.23 because the improved accuracy does not compensate for their increased computational burden. This work has about half as many parameters (<10) as GERG (> 20).

Table 10. Methane + carbon dioxide mixture data used in the fit

Source	Symbol	Composition (mol CH ₄)	Temperature Range (K)	Pressure Range (MPa)
Hwang <i>et al.</i> *	x	0.10-0.90	350 K	Up to 40 MPa
Reamer <i>et al.</i> *	◇	0.20-0.85	344-478 K	Up to 70 MPa

*Full biographic details are available in GERG [65]

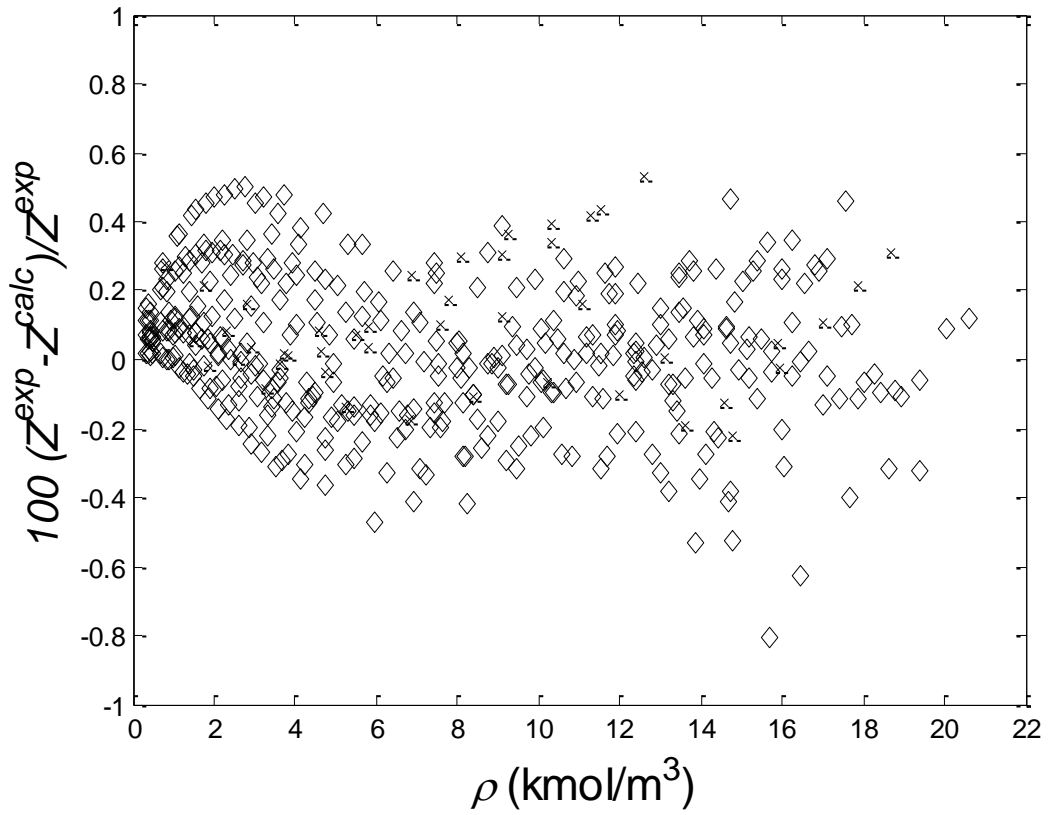


Figure 58. Relative deviation of the measured compressibility factors from the EoS predictions for methane + carbon dioxide mixtures

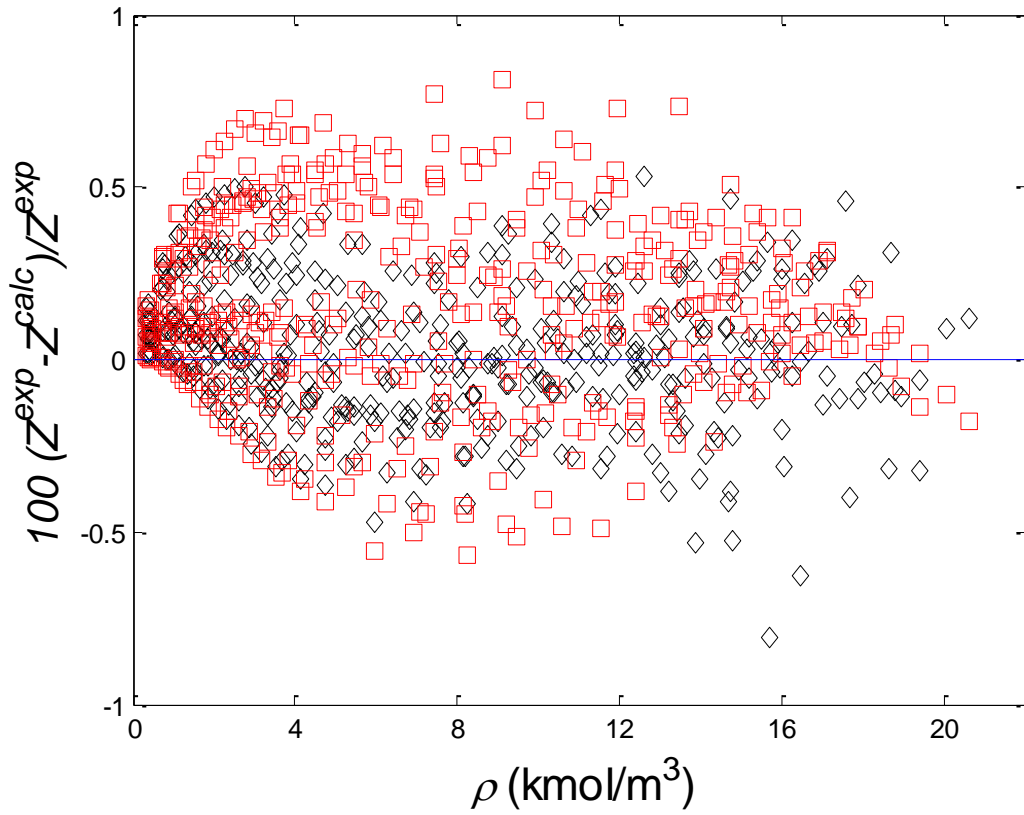


Figure 59. Relative deviation of the measured compressibility factors from the EoS predictions for methane + carbon dioxide mixtures: this work (\diamond), GERG (\square)

Ethane + carbon dioxide

Ethane + carbon dioxide mixture data sets that were included in the fit are shown in Table 11, and the results of the fit in Figure 60. Most data can be predicted within $\Delta Z/Z = \pm 0.4\%$. Ethane + carbon dioxide mixtures do require an additional compositional term for the second coefficient n_2 than stated in equation 4.23 in the form of equation 4.24.

$$n_2 = c_{0,2} + c_{1,2}/T + c_{2,2}/T^2 + c_{3,2}x_1x_2(c_{4,2}x_1 + x_2) + c_{5,2}x_1^2x_2^2(c_{5,2}x_1 + x_2) \quad (4.24)$$

GERG did not create a binary, specific departure function for this mixture but rather used the general form (equation 4.11) and fit the reducing parameter (only four parameters). Their predictions (shown in Figure 61) match the experimental values well at the low densities, but there is a systematic bias at higher densities. The higher densities were not included in their fit.

Table 11. Ethane + carbon dioxide mixture data used in the fit

Source	Symbol	Composition (mol CO ₂)	Temperature Range (K)	Pressure Range (MPa)
Brugge <i>et al.</i> *	x	0.10-0.90	320 K	Up to 7 MPa
Lemming <i>et al.</i> *	◇	0.10-0.90	320 K	Up to 7 MPa
McElroy <i>et al.</i> *	□	0.23-0.64	313-333 K	Up to 14 MPa
Reamer <i>et al.</i> *	+	0.18-0.83	410-477 K	Up to 70 MPa
Rurhgas*	*	0.23-0.70	310-320 K	Up to 14 MPa

*Full biographic details are available in GERG [65]

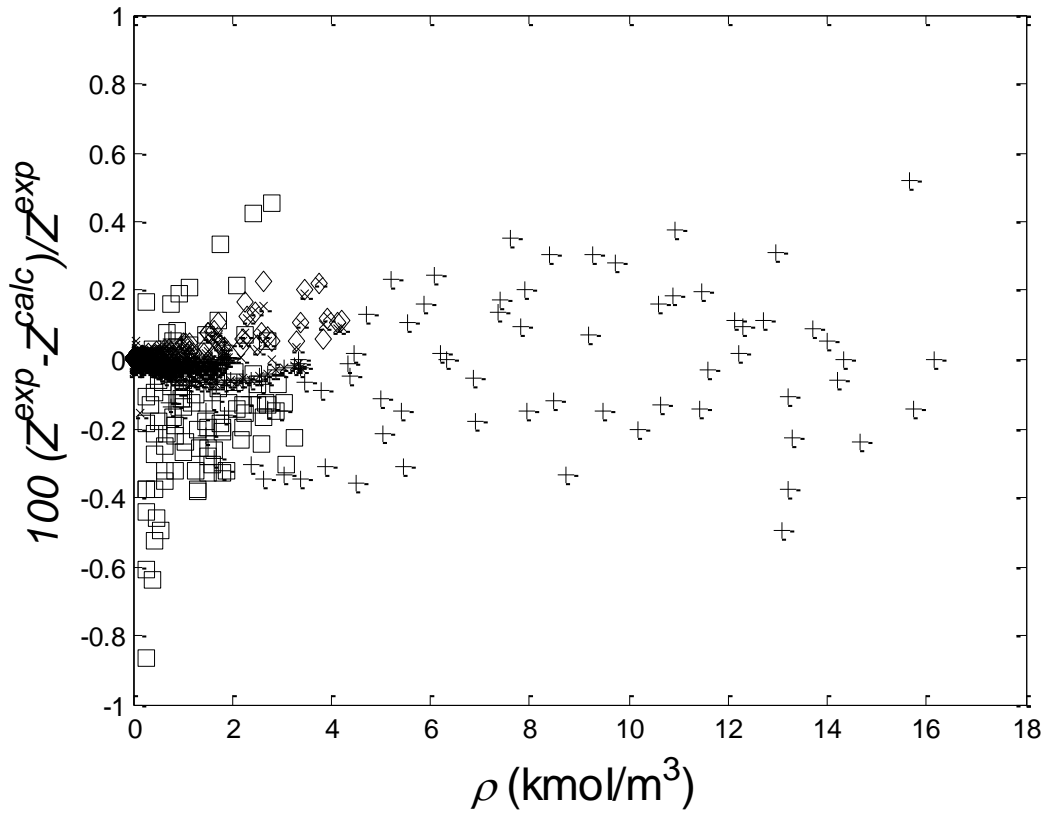


Figure 60. Relative deviation of the measured compressibility factors from the EoS predictions for ethane + carbon dioxide mixtures

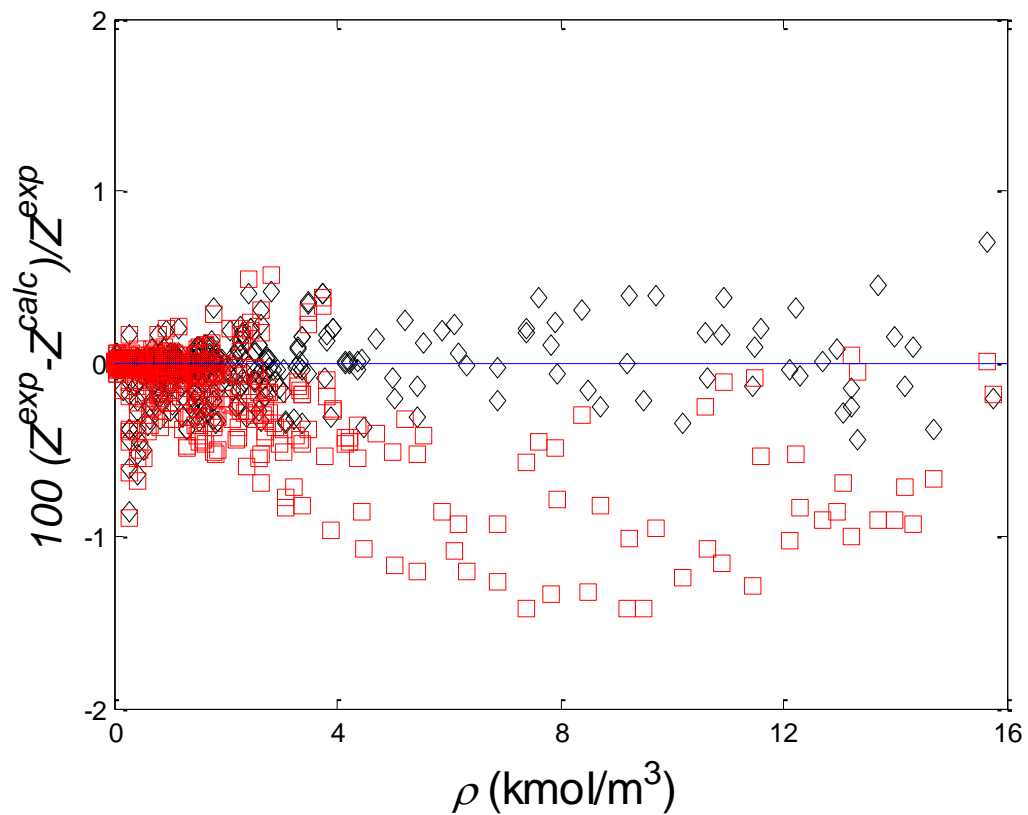


Figure 61. Relative deviation of the measured compressibility factors from the EoS predictions for ethane + carbon dioxide mixtures: this work (\diamond), GERG (\square)

Argon + nitrogen

The data sets for the argon + nitrogen mixtures that were included in the fit are shown in Table 12, and the results of the fit in Figure 62. Both molecules in the argon + nitrogen binary system are relatively simple, but composition dependence is required to bring most of the data for these mixtures within $\Delta Z/Z = \pm 0.3\%$. Townsend [93] data show a systematic trend although the model describes these data within their reported experimental uncertainty of $\Delta Z/Z = \pm 0.5\%$.

Figure 63 compares the current and GERG models. Both models have similar predicative capabilities, but GERG does have a slight positive systematic bias. This is not surprising because this binary system was not a primary focus in their work, so the general model with four reducing parameter were used.

Table 12. Argon + nitrogen mixture data used in the fit

Source	Symbol	Composition (mol Ar)	Temperature Range (K)	Pressure Range (MPa)
Kosov <i>et al.</i> [84]	x	0.16-0.81	293-353 K	Up to 70 MPa
Crain <i>et al.</i> *	◇	0.003-0.80	273 K	Up to 53 MPa
Townsend [93]	□	0.16-0.84	298-323 K	Up to 14 MPa

*Full biographic details are available in GERG [65]

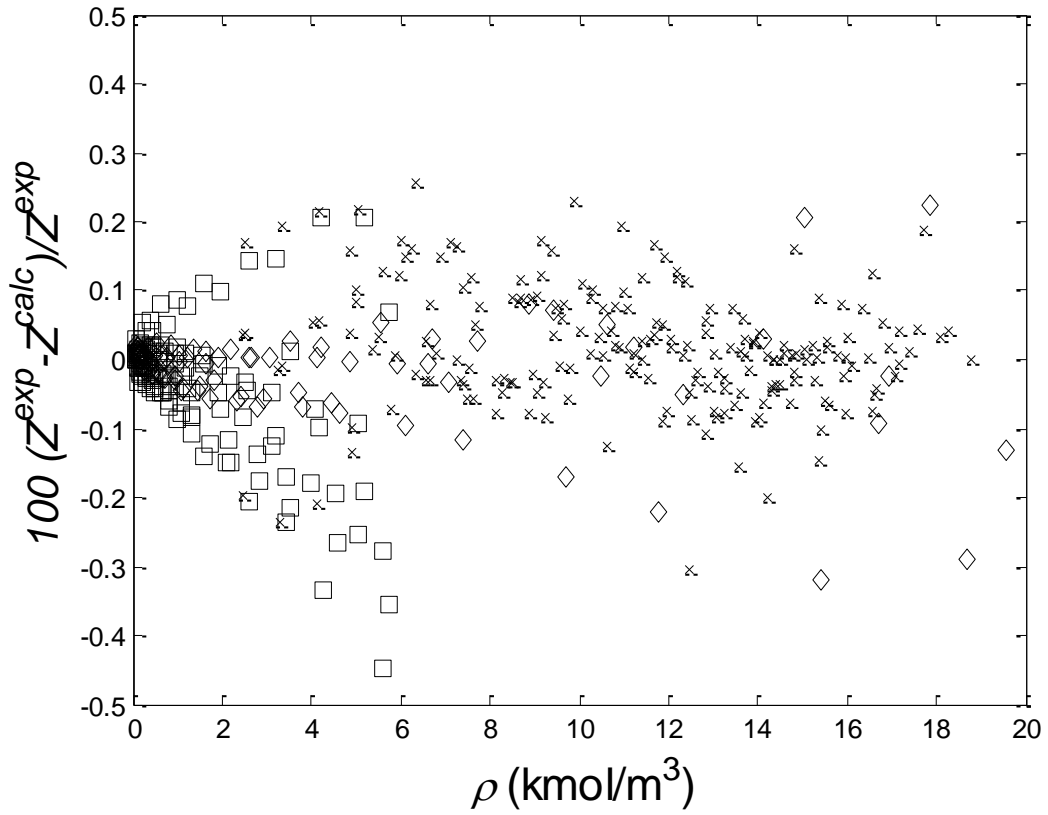


Figure 62. Relative deviation of the measured compressibility factors from the EoS predictions for argon + nitrogen mixtures

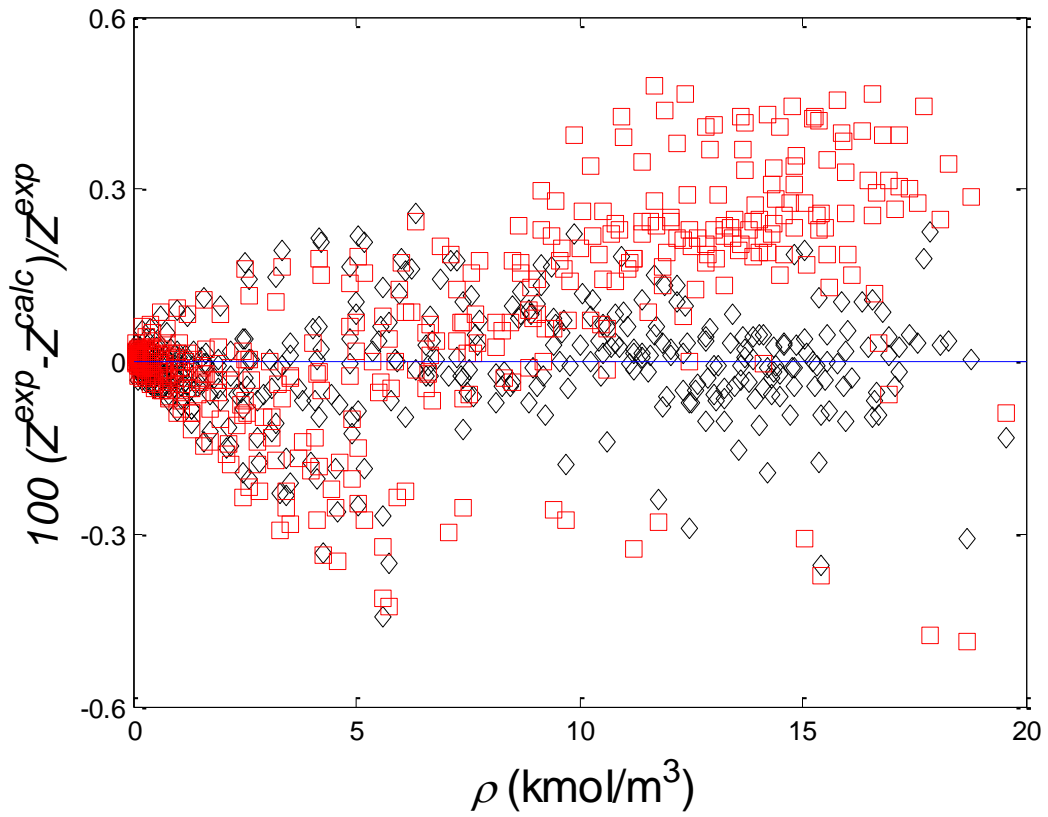


Figure 63. Relative deviation of the measured compressibility factors from the EoS predictions for argon + nitrogen mixtures: this work (\diamond), GERG (\square)

Hydrogen + nitrogen

The data sets for the hydrogen + nitrogen mixtures that were included in the fit are shown in Table 13, and the results of the fit in Figure 64. Attempts were made to fit hydrogen + nitrogen mixtures with relatively good results. The hydrogen reference EoS [87] claims low uncertainties in densities of $\Delta\rho/\rho = \pm 0.04\%$ from 250-450 K and up to 300 MPa. At temperatures above 450 K the uncertainty rises sharply to $\Delta\rho/\rho = \pm 1.0\%$.

Results are shown in Figure 64. Most of the deviations are within $\Delta Z/Z = \pm 0.5\%$, with the exception of the Lialine *et al.* [94] data. The Deming *et al.* [95] data show a systematic trend of positive deviations that increase with increasing temperature. Additional temperature powers of up to sixth order were tested with no improvement of the fits. This trend also is seen in the GERG predictions, implying that this may be an artifact of the experimental data, or of limitations of the hydrogen reference EoS.

The overall comparison of GERG and the fit can be seen in Figure 65 compares the current and GERG models. The two models have similar order of magnitude predictive capabilities, but they have opposite behavior at higher densities with GERG over predicting and our fit under predicting. This could be caused by using different hydrogen reference EoS: the current fit uses 2009 reference EoS, while GERG used the general model of equation 4.11 in their mixture calculations. This again demonstrates the need not only for mixture data but also for accurate pure fluid data.

Table 13. Hydrogen + nitrogen mixture data used in the fit

Source	Symbol	Composition (mol N ₂)	Temperature Range (K)	Pressure Range (MPa)
Wieber <i>et al.</i> *	x	0.13-0.74	273-573 K	Up to 101 MPa
Lialine <i>et al.</i> [94]	+	0.27	322-446 K	Up to 156 MPa
Deming <i>et al.</i> [95]	◇	0.25	203-573 K	Up to 148 MPa
Jaeschke <i>et al.</i> *	□	0.25-0.85	270-353 K	Up to 30 MPa

*Full biographic details are available in GERG [65]

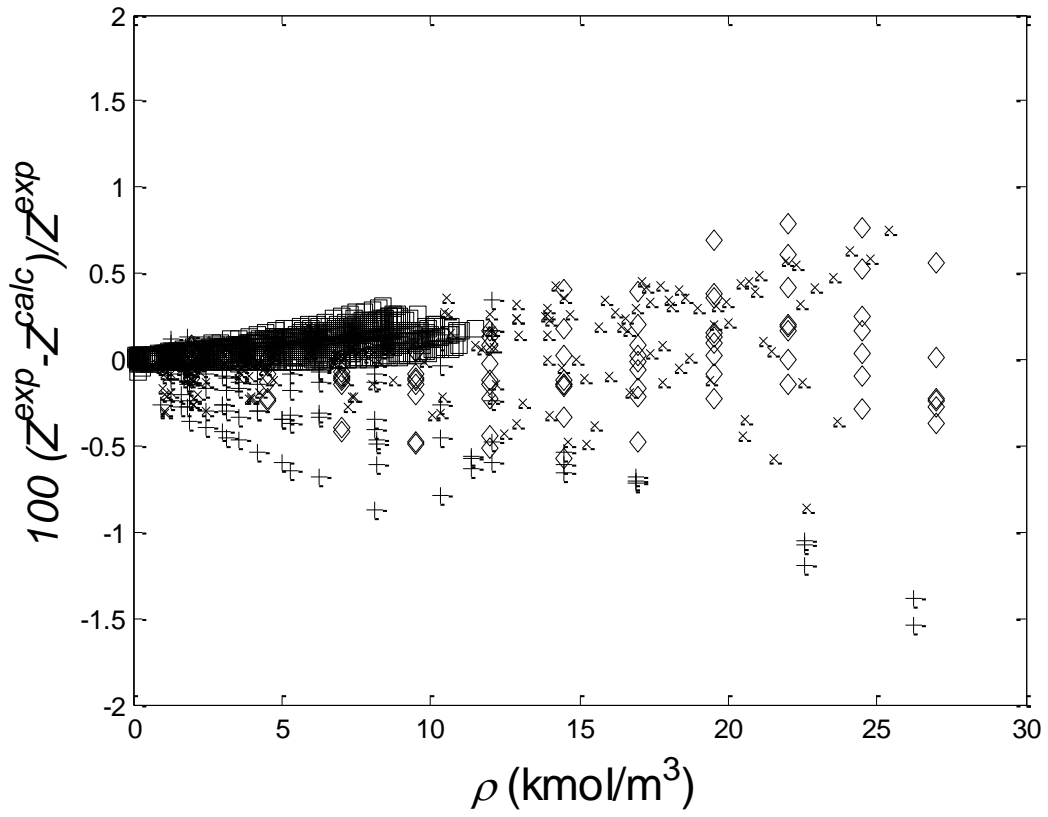


Figure 64. Relative deviation of the measured compressibility factors from the EoS predictions for hydrogen + nitrogen mixtures

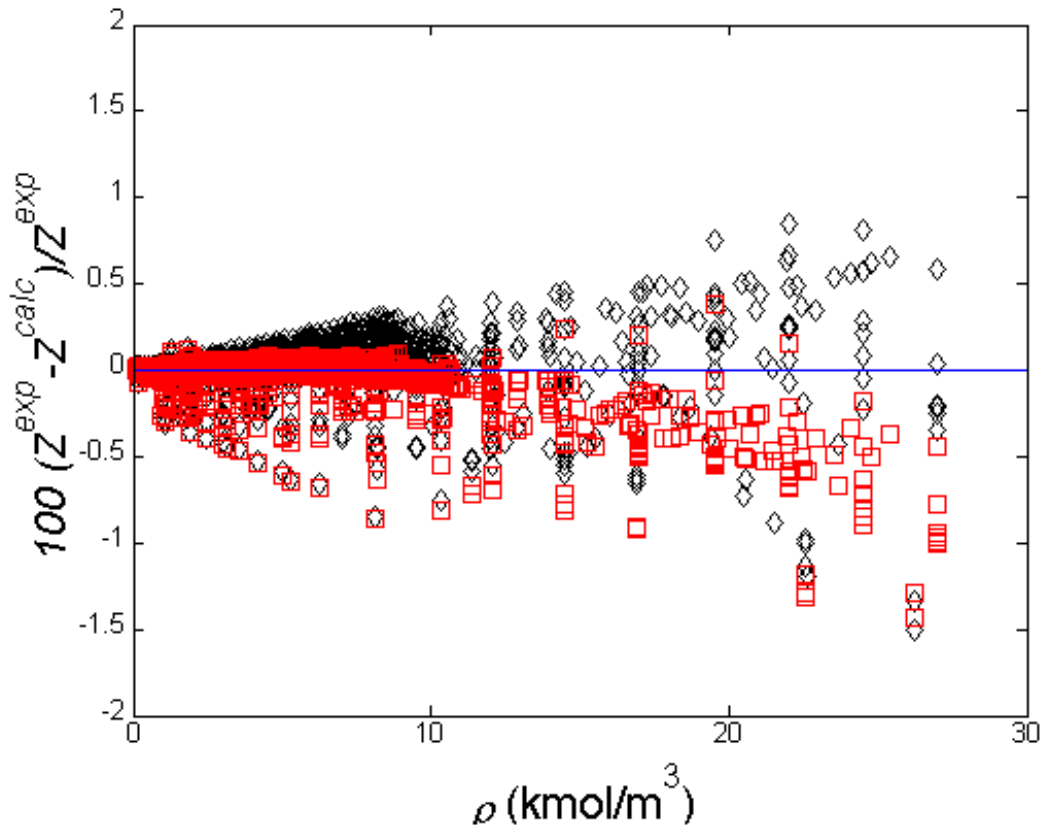


Figure 65. Relative deviation of the measured compressibility factors from the EoS predictions for hydrogen + nitrogen mixtures: this work (\diamond), GERG (\square)

4.2.3.3. Helium mixtures

Finally, binary mixtures containing helium with argon, krypton, nitrogen, or methane, were fit. In general, these fits required the most complex compositional dependence, and preferred this extra dependence, in the form of equation 4.23, to be in the denominator (n_4). This leads us to believe that this is caused by repulsion effects.

Helium + argon

For helium + argon only one data set, Blancett *et al.* [52] at 323 K, was used in the fit. Figures 66 and 67 show the results without and with the compositional dependence in n_4 respectively, with extra dependence, the data lie within $\Delta Z/Z = \pm 0.1\%$ compared to $\Delta Z/Z = \pm 0.15\%$ without the dependence.

At low densities, both equations show systematic trends with respect to composition, however, all deviations well the combined uncertainties of the experimental measurements and of the pure fluid reference equations. The additional compositional dependence contributes the most and improves the predictions at higher densities. The systematic trends are a concern, although they appear to be density rather than composition dependent. However, because the deviations lie within the experimental uncertainties, the systematic trends are not statistically significant. A comparison to GERG is shown in Figure 68.

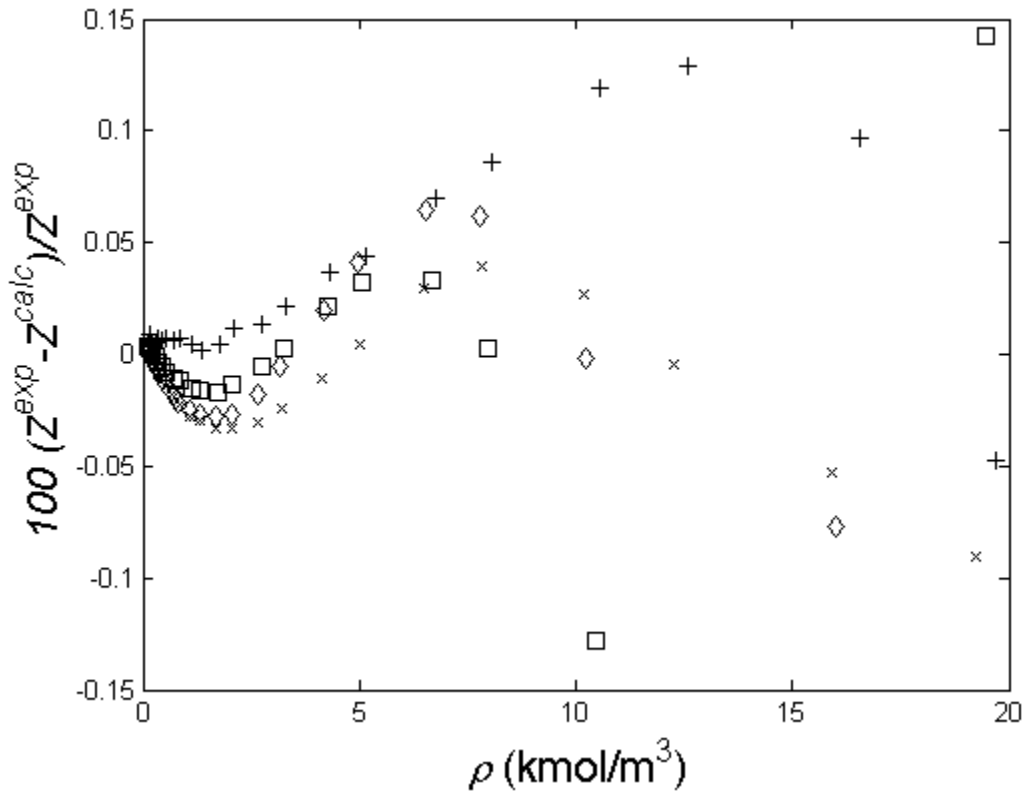


Figure 66. Relative deviation of the measured compressibility factors from the EoS predictions without compositional dependence in n_4 for helium + argon mixtures (+ $x_{\text{He}} = 0.80$, \times $x_{\text{He}} = 0.60$, \diamond $x_{\text{He}} = 0.41$, and \square $x_{\text{He}} = 0.22$)

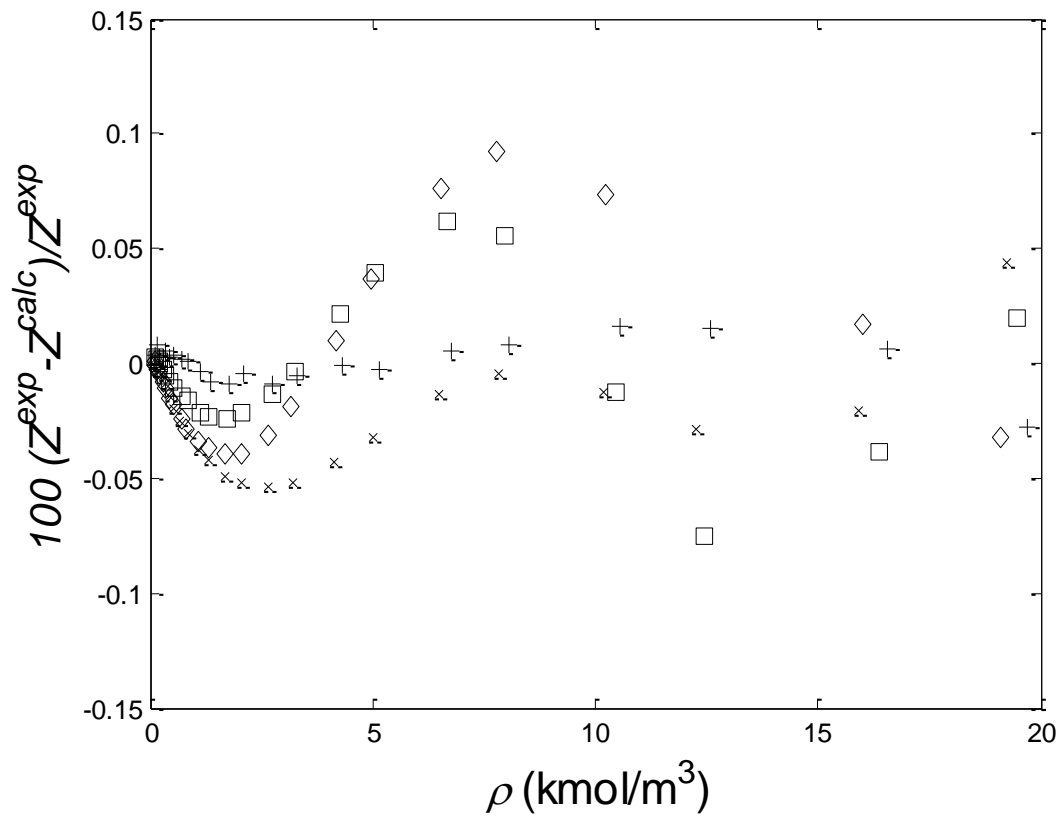


Figure 67. Relative deviation of the measured compressibility factors from the EoS predictions with compositional dependence in n_4 for helium + argon mixtures (+ $x_{\text{He}} = 0.80$, \times $x_{\text{He}} = 0.60$, \diamond $x_{\text{He}} = 0.41$, and \square $x_{\text{He}} = 0.22$)

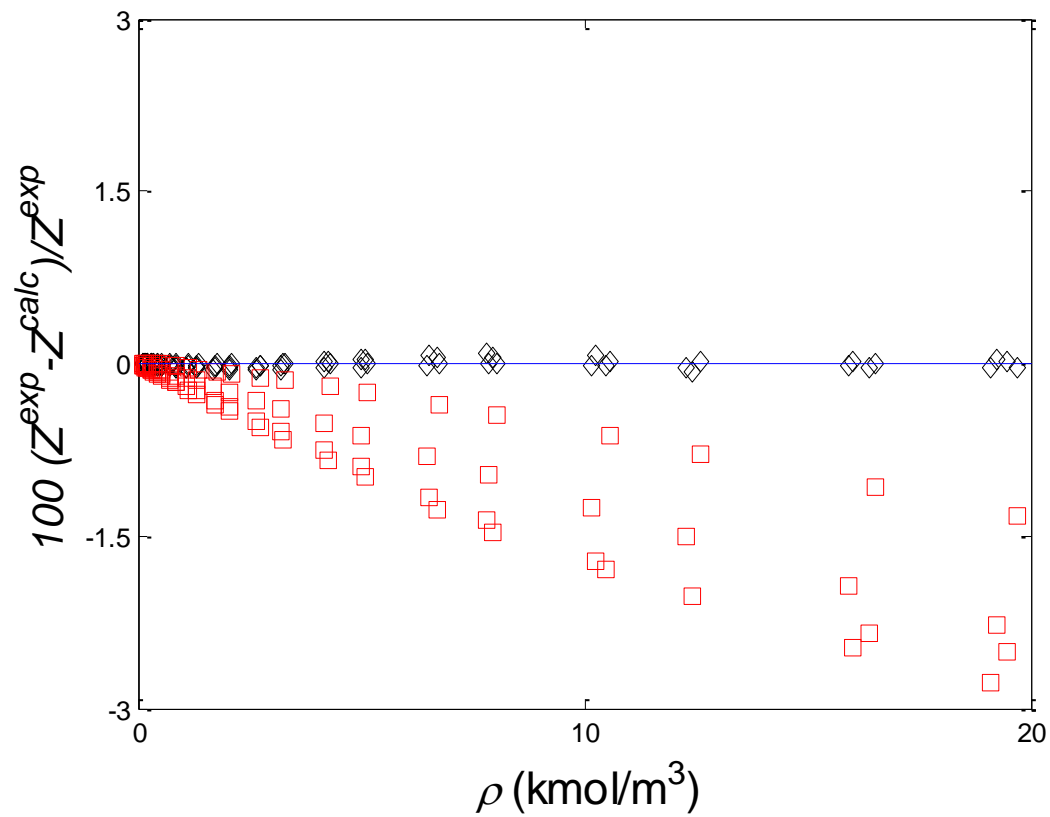


Figure 68. Relative deviation of the measured compressibility factors from the EoS predictions for the current model (\diamond) and GERG (\square) for mixtures of helium + argon

The argon + helium binary system was not part of the primary focus for the GERG development, so larger deviations are not unexpected. The GERG model does exhibit clear compositional trends that indicate that the compositional dependence, a modification of van Laar in the reducing parameters, is insufficient. The lack of experimental measurements severely limits development of the composition dependence.

Helium + krypton

Adding extra compositional dependence to the helium + argon fit provides one for helium + krypton. Data were limited to Dillard *et al.* [96]. This set does have a reasonable range of temperatures (223-323 K), but it is limited to low densities (up to 8 kmol/m⁻³). The krypton reference EoS [88] has a claimed uncertainty of $\Delta\rho/\rho = \pm 0.2\%$. Currently no data exist to validate or improve this assertion, so caution is advisable when interpreting the results. Fit results are shown without and with the additional composition dependence in the residual Helmholtz energy appear in Figure 69 and Figure 70 respectively.

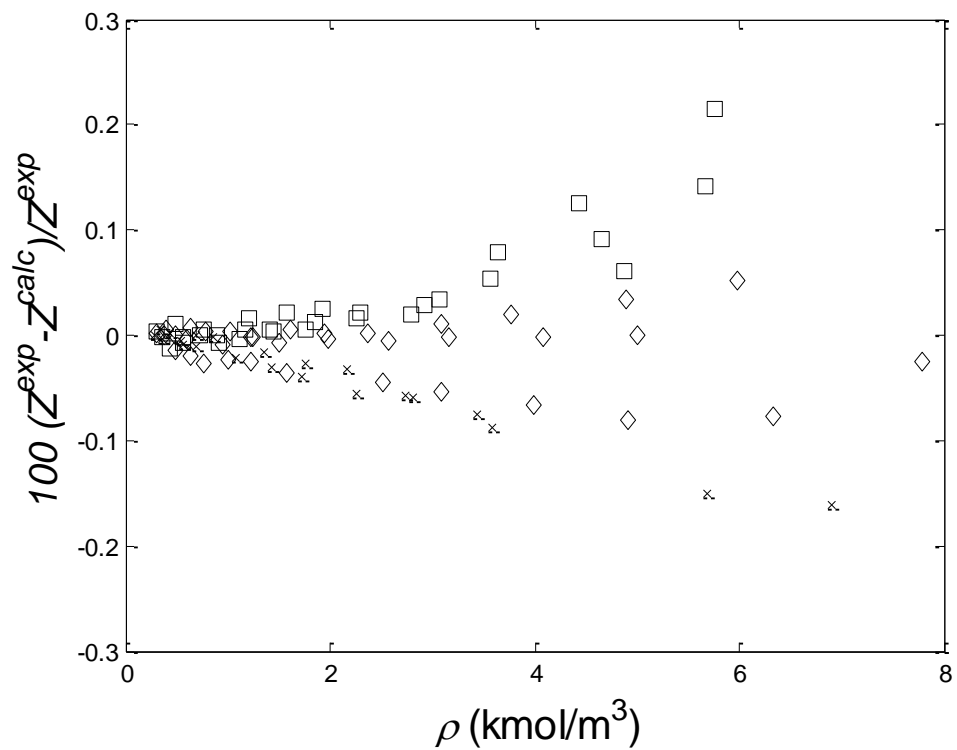


Figure 69. Relative deviation of the experimental compressibility factors from the equation of state predictions He + Kr mixtures with no composition dependence in the interaction residual Helmholtz energy (x He 0.25, ◇ He 0.50, and □ He 0.75)

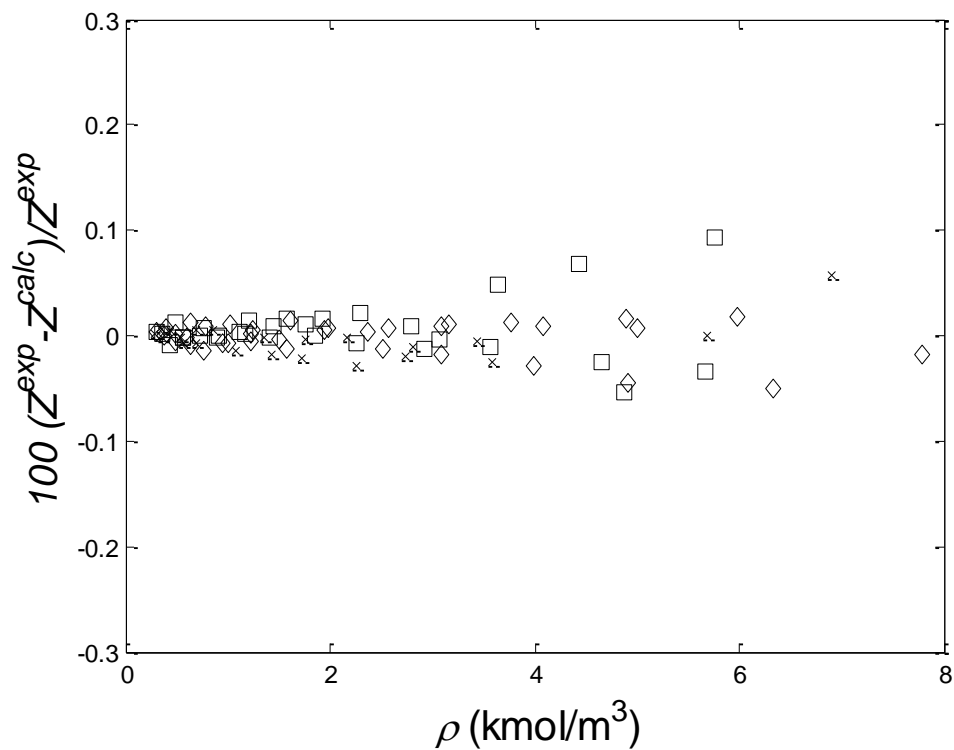


Figure 70. Relative deviation of the measured compressibility factors from the EoS predictions for He + Kr mixtures with additional composition dependence in the interaction residual Helmholtz energy (× He 0.25, \diamond He 0.50, and \square He 0.75)

Because the only available measurements are at low densities, neither fit includes a second order density term in the numerator, nor does the composition dependence appear in the denominator. The figures clearly show that adding composition dependence significantly improves the fit and removes the compositional trends seen in Figure 69. However, all deviations shown in Figure 69 lie within the uncertainty of the krypton reference (EoS), the compositional dependence must be viewed with caution. Because krypton was not included in the scope of work for GERG, no comparison can be made.

Helium + nitrogen

Because all the previous helium mixtures discussed above had data and reference equation limitations, no unqualified conclusions could be made. Significantly more experimental measurements and a validated reference equation exist for the helium + nitrogen binary system. Temperatures are restricted to a range of 273-373 K. Table 14 shows the experimental data sets used to fit the model. Figure 71 presents the fit without the composition dependence in n_4 .

Clearly, there is divergence for the Briggs *et al.* [97] data at higher densities. To get a better picture, Figure 72 depicts these data with each symbol representing a different composition.

Table 14. Helium + nitrogen mixture data used in the fit

Source	Symbol	Composition (mol He)	Temperature Range (K)	Pressure Range (MPa)
Briggs <i>et al</i> .[97]	x	0.11-0.89	273-298 K	Up to 101 MPa
Ku <i>et al.</i> [98]	◇	0.16-0.86	311-373 K	Up to 29 MPa
Miller <i>et al.</i> [99]	□	0.06-0.99	294 K	Up to 28 MPa

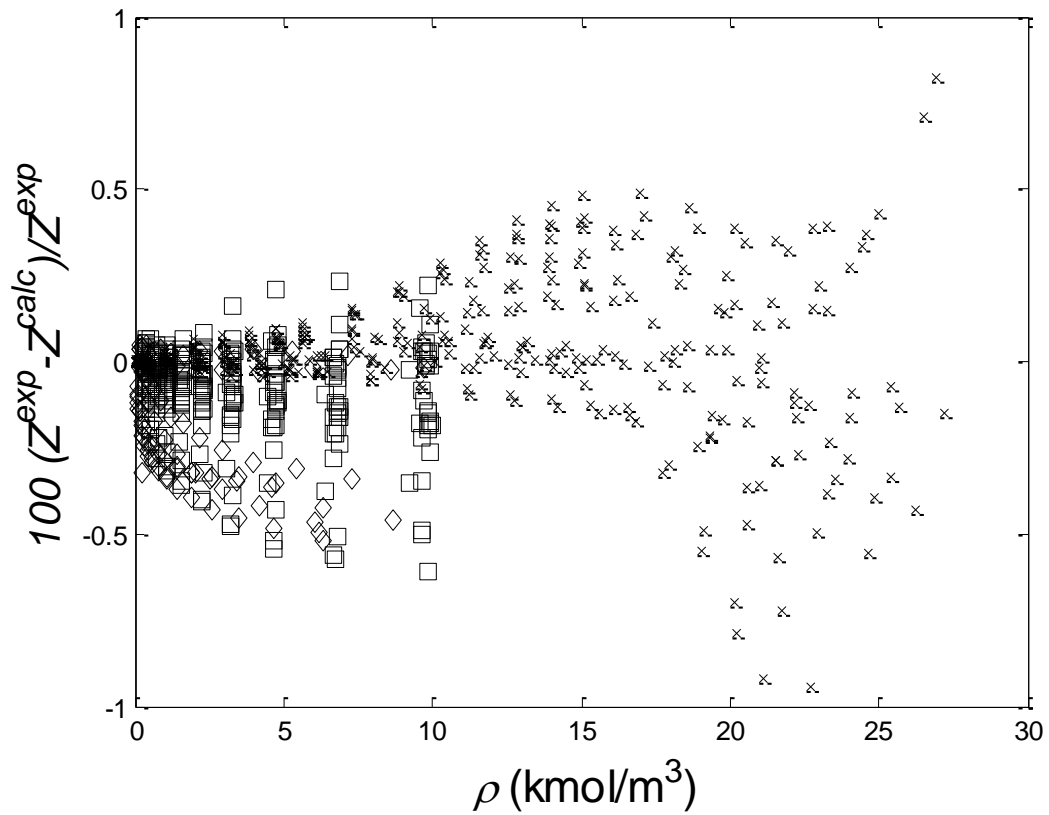


Figure 71. Relative deviation of the measured compressibility factors from the EoS predictions for helium + nitrogen mixtures without composition dependence in n_4

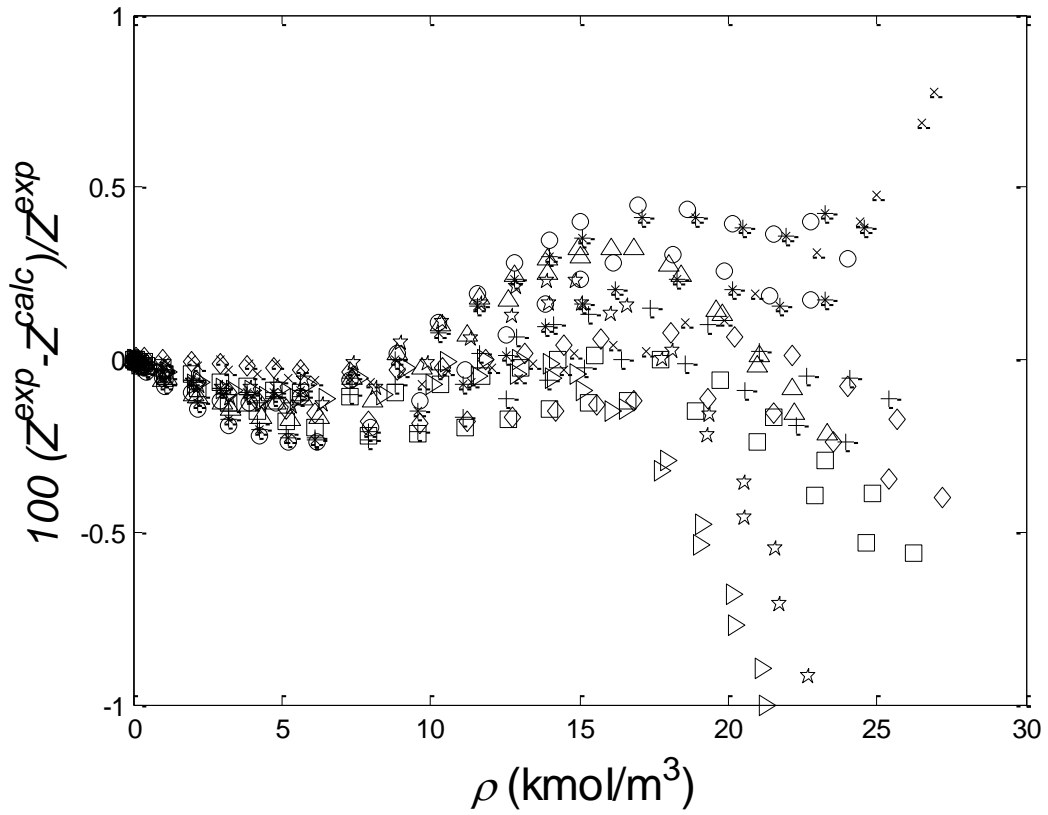


Figure 72. Relative deviation of the experimental compressibility factors from the EoS predictions for helium + nitrogen mixtures without composition dependence in n_4 for Briggs *et al.* [97] data (* He 0.90, \diamond He 0.80, \square He 0.70, + He 0.60, * He 0.50, o He 0.40, Δ He 0.30, \star He 0.20, and \triangleright He 0.10)

Figure 73 shows the fit with the composition dependence in n_4 , while Figure 74 shows only Briggs *et al.* [97] data. No improvement is seen for the lower densities potentially because of experimental uncertainties. However, a dramatic improvement is seen at higher densities. There still is however, a slight systematic trend in density, therefore, some work still needs to be done to improve this.

A comparison with GERG is shown in Figure 75. Helium mixtures were not their primary focus, however they did fit all the data presented with only the four reducing parameters. Their results are remarkable for how few parameters were used, but some compositional dependence still exists at the higher densities.

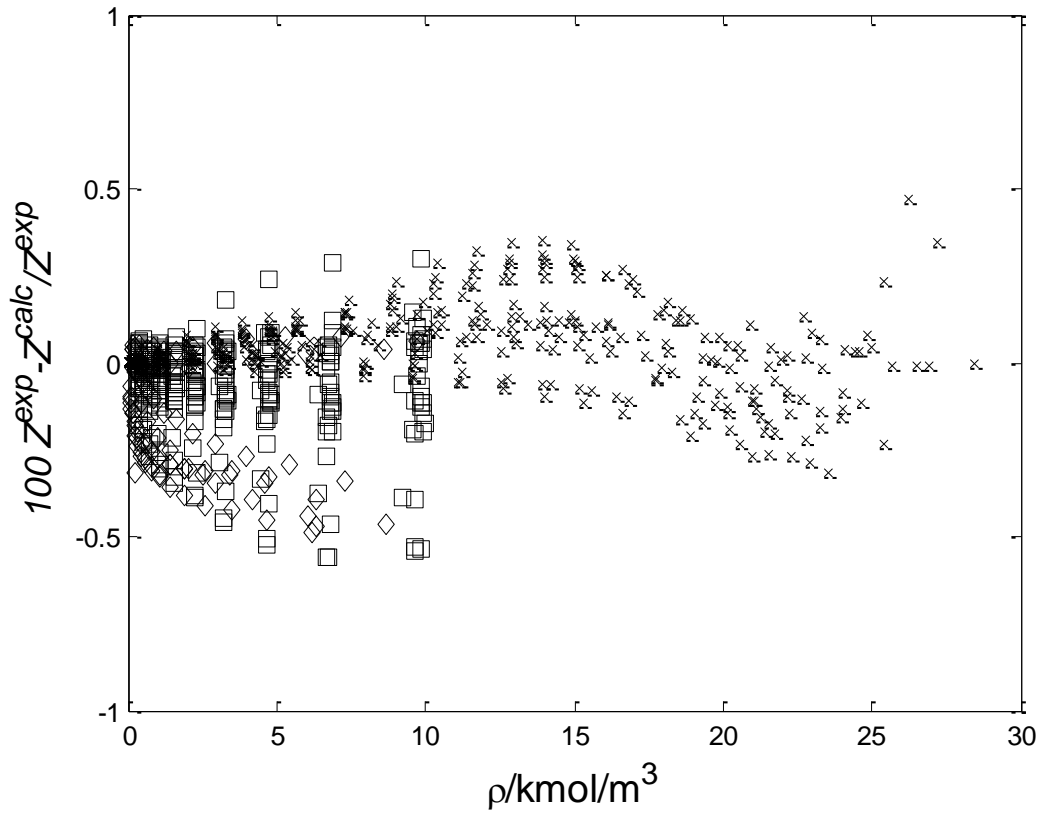


Figure 73. Relative deviation of the experimental compressibility factors from the EoS predictions for helium + nitrogen mixtures with composition dependence in n_4

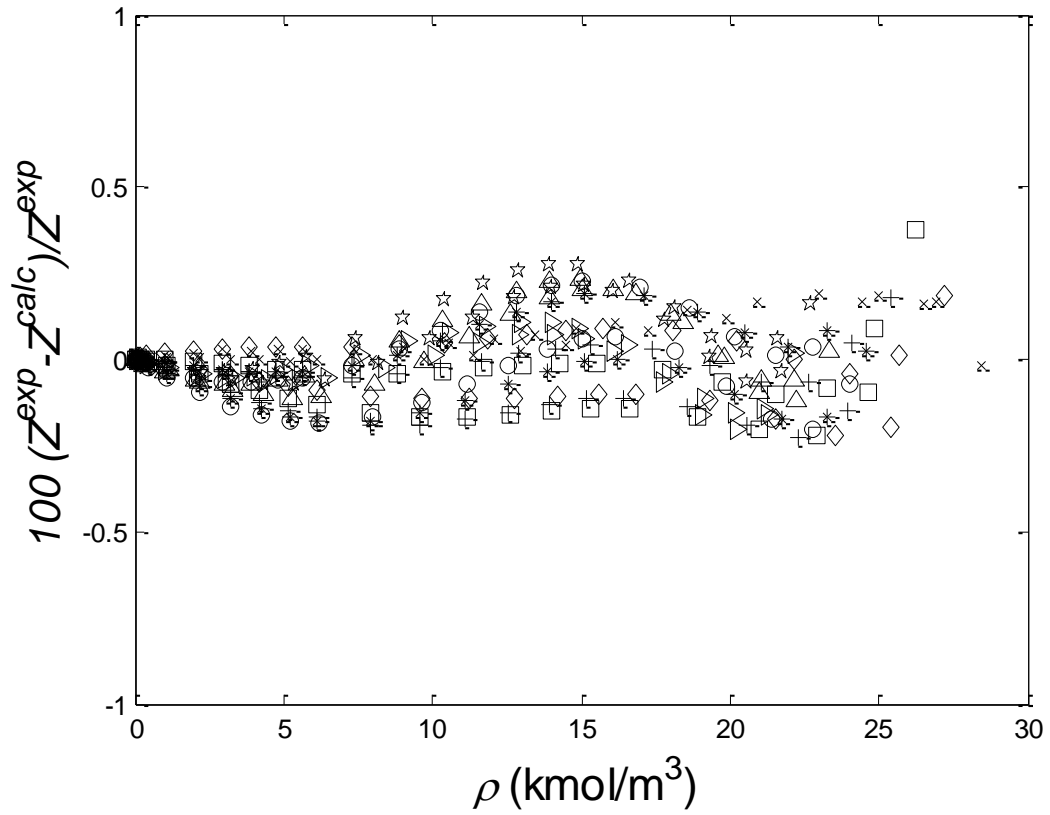


Figure 74. Relative deviation of the experimental compressibility factors from the EoS predictions for helium + nitrogen mixtures with composition dependence in n_4 for Briggs *et al.* [97] data (\times He 0.90, \diamond He 0.80, \square He 0.70, $+$ He 0.60, $*$ He 0.50, o He 0.40, \triangle He 0.30, \star He 0.20, and \triangleright He 0.10)

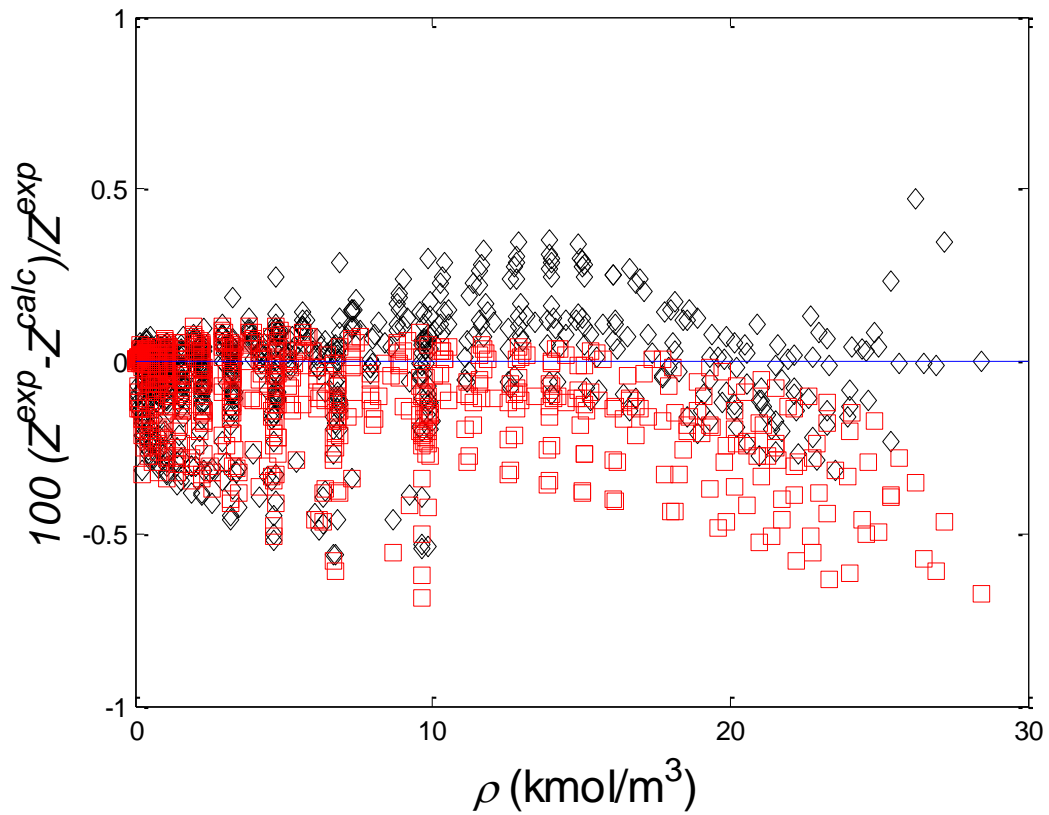


Figure 75. Relative deviation of the experimental compressibility factors from the EoS predictions for the current model (\diamond) and GERG (\square) for mixtures of helium + nitrogen

Helium + methane

Finally, the helium + methane mixtures described in Section 3.3 were fit. Figure 76-77 show the fit results without and with composition dependence in n_4 , respectively.

These figures confirm the need for composition dependence in n_4 . There is a clear systematic trend in the density. As with other fits, higher order density terms were tested with no success. When comparing to GERG, as in Figure 78, it is important to note that a very limited data set was used to determine the parameters and there are only two adjustable parameters. Because most of these data are at low temperature with no more than 0.37 mole fraction of helium, and the extrapolation is impressive.

This work has demonstrated that less complex forms with a smaller number of coefficients for the interaction Helmholtz energy can produce similar predictions compared to the more complex forms of GERG. The new forms for the interaction Helmholtz energy also have much lower power density compared to the pure fluids as shown by Gomez-Osorio *et al.* [20]. These characteristics make it an attractive approach to deal with mixtures for process modelling.

These fits are not intended to be the final form for predictions of mixture properties, but they serve as a starting point to be built upon to encompass all of the fluid behavior, including the super-critical fluid region, compressed liquid, *etc.* An important conclusion is the need for more experimental measurements for both pure fluids and mixtures to continue the development of the proposed model.

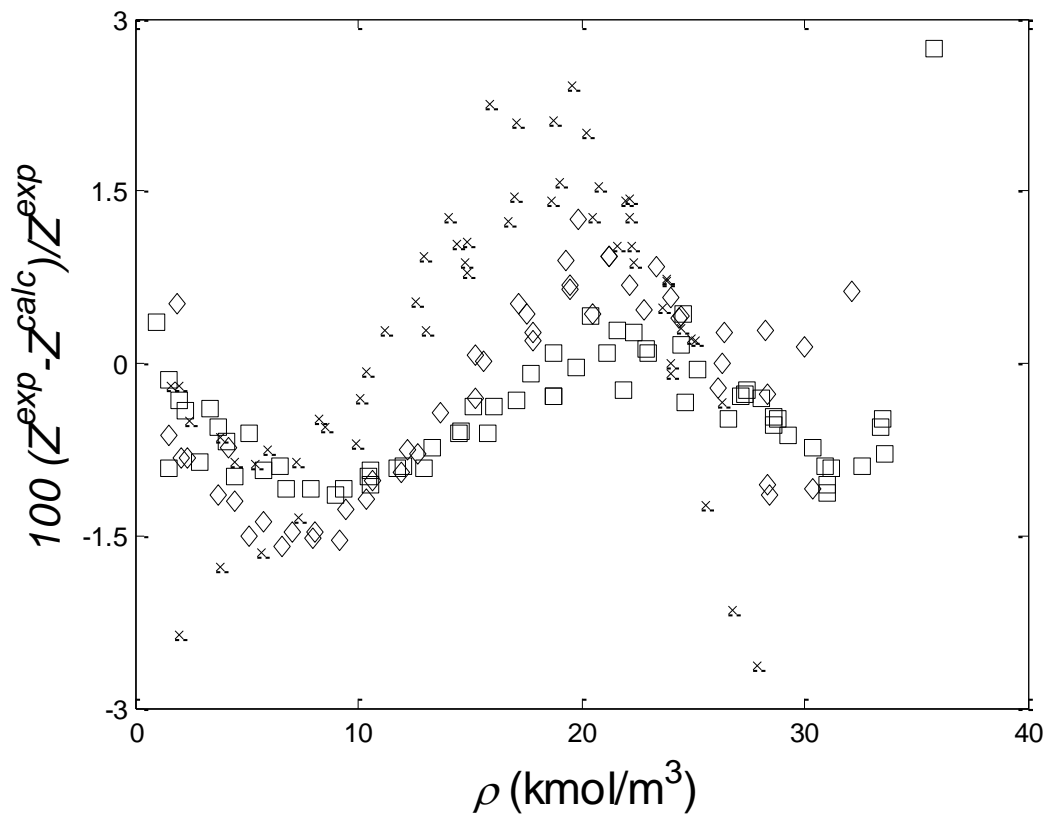


Figure 76. Relative deviations of experimental compressibility factors from the EoS predictions for helium + methane mixtures with composition dependence in n_2 but not n_4 (\square He 0.75, \diamond He 0.55, \times He 0.25)

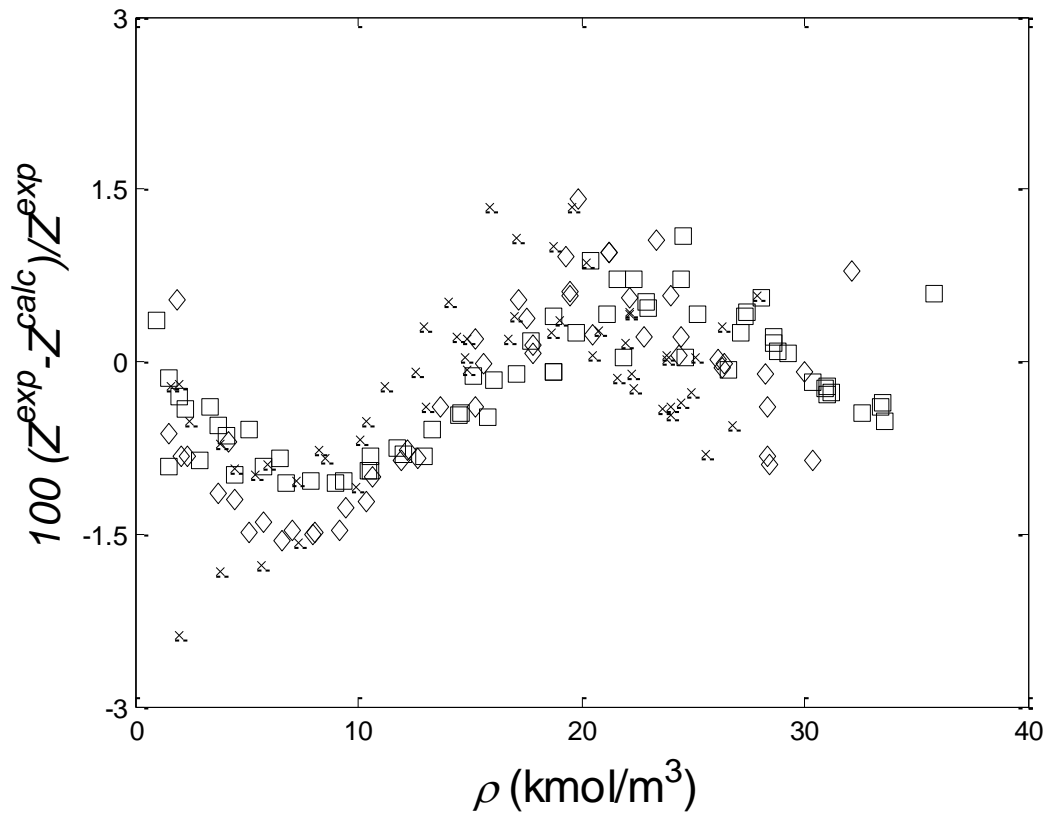


Figure 77. Relative deviations of the experimental compressibility factors from the EoS predictions for helium + methane mixtures with composition dependence in both n_2 and n_4 (\square He 0.75, \diamond He 0.55, \times He 0.25)

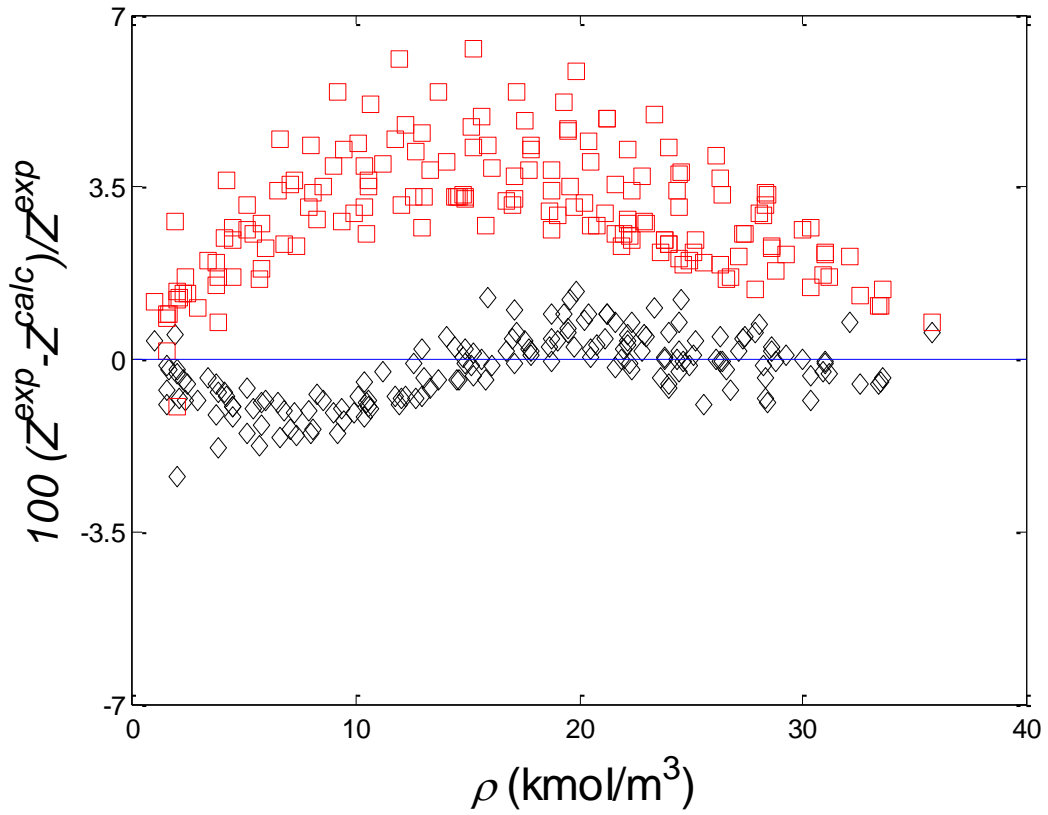


Figure 78. Relative deviation of the measured compressibility factors from the EoS predictions for helium + methane mixtures: this work (\diamond), GERG (\square)

5. CONCLUSIONS AND RECOMMENDATIONS

This work describes the redesign and recommissioning of a single-sinker, magnetic-suspension densimeter for measuring densities from 300 to 500 K at pressures up to 200 MPa. Some of these improvements to the system include an electrical heating system, new heating shields, vacuum insulation, a simpler leveling system, separation of temperature measurement devices, and a new measurement sequence that reduces the experimental run time. All these aspects provide a wider range in temperature measurement and improved measurement stabilities within the system. By extending the temperature range of the MSD, the apparatus now can operate in a range where very few other accurate apparatus can reach.

A new silicon sinker was tested and showed promise in improving the resolution of measurements in the lower density range. However, this also exposed a previously unknown limitation of the system, in which the density range of the apparatus is directly related to the density of the sinker. Densities must be at least half that of the sinkers, or control issues will occur.

Once commissioned and verified, the MSD provided densities for pure helium and argon at temperatures of 303 to 450 K at pressures up to 200 MPa. The argon data reduced significantly the uncertainty of the current reference EoS at high pressures, where no data previously existed. This validation now allows argon to be used as a calibration fluid for other high-pressure apparatus, such as vibrating tube densimeters.

For helium, the density measurements show that improvements can be made to the reference EoS in the high pressure range within the temperature range of 303 to 450 K

using these data. These data also displayed the advantages of using a silicon sinker that produced about half as much experimental uncertainty as the titanium sinker. Measurements of three binary mixtures of helium + methane for four isotherms between 300 and 450 K at pressures up to 200 MPa were conducted. These data cover a range where very limited data exist and indicate possible improvements for the current EoS.

There are still many mixtures that lack high-pressure data and measurements over a broad range of compositions. The MSD can provide these accurate measurements up to 200 MPa. Such mixtures include nitrogen + helium, helium + krypton, helium + argon, argon + methane, methane + propane, and nitrogen + propane. Measurement of ternary mixtures composed of the above species also would provide tests for current EoS and enable new ones, such as the one proposed in section 4.

Next, development of mixing rules based upon residual Helmholtz energy for binary systems was presented. This method combines statistical mechanics and quadratic dependence of the second virial coefficient with empirical models for excess Gibbs energy to cover wide ranges in densities. The approach requires significantly fewer parameters than current EoS and its less complex form makes it an attractive approach to process modeling. A least squares minimization algorithm calculates the parameters for eleven binary mixtures of methane, nitrogen, ethane, carbon dioxide, argon, helium, krypton, and hydrogen using p - ρ - T data. Further development of this model needs to be conducted to solve issues in regions such as critical and compressed liquid regions. Other functions and more complex molecules should be tested.

The most important finding was the need for more p - ρ - T data. There exist very few accurate p - ρ - T data sets with extensive ranges, especially in the case of mixtures. These data will be required to continue building our understanding and help improve predictive capabilities of EoS.

REFERENCES

1. U.S. Energy Information Administration, *Primary energy consumption by source*. 2016, U.S. Energy Information Administration: <https://www.eia.gov/totalenergy/data/browser/?tbl=T01.03#/?f=A>.
2. A. Shadravan and M. Amani, *HPHT 101: What every engineer or geoscientist should know about high pressure high temperature wells*. Society of Petroleum Engineers, 2012.
3. J.C. Holste, K.R. Hall, P.T. Eubank, and K.N. Marsh, *High pressure PVT measurements*. Fluid Phase Equilibria, 1986. **29**: p. 161-176.
4. A. Goodwin, K. Marsh, and W. Wakeham, *Measurement of the thermodynamic properties of single phases*. 2003: Elsevier.
5. E.S. Burnett, *Compressibility determinations without volume measurements*. Journal of Applied Mechanics, 1936. **3**: p. A136-A140.
6. I.H. Silberberg, K.A. Kobe, and J.J. McKetta, *Gas compressibilities with the burnett apparatus. Methods and apparatus*. Journal of Chemical & Engineering Data, 1959. **4**: p. 314-323.
7. A.E. Hoover, F.B. Canfield, R. Kobayashi, and T.W. Leland, *Determination of virial coefficients by the burnett method*. Journal of Chemical & Engineering Data, 1964. **9**(4): p. 568-573.
8. M. Waxman and J.R. Hastings, *A Burnett apparatus for the accurate determination of gas compressibility factors and second virial coefficients, and an evaluation of its capability based on some results for argon and carbon dioxide*.

Journal of Research of the National Bureau of Standards-C Engineering and Instrumentation, 1971. **75**: p. 165-176.

9. D.E. Cristancho, *Experimental characterization and molecular study of natural gas mixtures*. PhD. Dissertation. Texas A&M University, College Station, TX. 2010.
10. A.D. Tibaduiza, D.E. Cristancho, D. Ortiz-Vega, I.D. Mantilla, M.A. Gomez-Osorio, R.A. Browne, J.C. Holste, and K.R. Hall, *Calculation of energies and entropies from isochoric and isothermal experimental data*. Journal of Chemical and Engineering Data, 2014. **59**(4): p. 999-1005.
11. J.S. Rowlinson, G.J. Esper, J.C. Holste, K.R. Hall, M.A. Barrufet, and P.T. Eubank, *Collinearity of isochores at single- and two-phase boundaries for fluid mixtures*. in *ACS Symposium Series*. 1986.
12. P.L. Acosta-Perez, D.E. Cristancho, I.D. Mantilla, K.R. Hall, and G.A. Iglesias-Silva, *Method and uncertainties to determine phase boundaries from isochoric data*. Fluid Phase Equilibria, 2009. **283**(1-2): p. 17-21.
13. W.R. Lau, *A continuously weighed pycnometer providing densities for carbon dioxide + ethane mixtures between 240 and 350 K at pressures up to 35 MPa*. PhD. Dissertation. Texas A&M University, College Station, TX. 2001.
14. C.D. Holcomb and S.L. Outcalt, *A theoretically-based calibration and evaluation procedure for vibrating-tube densimeters*. Fluid Phase Equilibria, 1998. **150–151**: p. 815-827.

15. C. Bouchot and D. Richon, *An enhanced method to calibrate vibrating tube densimeters*. *Fluid Phase Equilibria*, 2001. **191**(1): p. 189-208.
16. E.F. May, W.J. Tay, M. Nania, A. Aleji, S. Al-Ghafri, and J. Martin Trusler, *Physical apparatus parameters and model for vibrating tube densimeters at pressures to 140 MPa and temperatures to 473 K*. *Review of Scientific Instruments*, 2014. **85**(9): p. 095111.
17. M.A. Gomez-Osorio, *Modeling and experimental measurements of thermodynamic properties of natural gas mixtures and their components*. PhD. Dissertation. Texas A&M University, College Station, TX. 2016.
18. S.L. Outcalt and M.O. McLinden, *Automated densimeter for the rapid characterization of industrial fluids*. *Industrial & Engineering Chemistry Research*, 2007. **46**(24): p. 8264-8269.
19. M.A. Gomez-Osorio, R.A. Browne, M. Carvajal Diaz, K.R. Hall, and J.C. Holste, *Density measurements for ethane, carbon dioxide, and methane + nitrogen mixtures from 300 to 470 K up to 137 MPa using a vibrating tube densimeter*. *Journal of Chemical & Engineering Data*, 2016. **61**(8): p. 2791-2798.
20. M.A. Gomez-Osorio, R.A. Browne, D.E. Cristancho, J.C. Holste, K.R. Hall, and Ian H. Bell, *An equation of state based upon a ratio of polynomials (rational) form for the residual helmholtz energy: Application to nitrogen, argon and methane*. *Molecular Physics*, 2017: p. 1-18.

21. W. Wagner and R. Kleinrahm, *Densimeters for very accurate density measurements of fluids over large ranges of temperature, pressure, and density*. Metrologia, 2004. **41**(2): p. S24.
22. P.V. Patil, *Commissioning of a magnetic suspension densitometer for high-accuracy density measurements of natural gas mixtures*. PhD Dissertation. Texas A&M University, College Station, TX. 2005.
23. R. Masui, W.M. Haynes, R.F. Chang, H.A. Davis, and J.M.H. Levelt Sengers, *Densimetry in compressed fluids by combining hydrostatic weighing and magnetic levitation*. Review of Scientific Instruments, 1984. **55**(7): p. 1132-1142.
24. R. Kleinrahm and W. Wagner, *Development and construction of a density measurement apparatus for measurement of boiling and dew densities of pure fluids over the complete phase boundary curve*. Progress Reports of the VDI Journals, Series, 1984. **3**.
25. R. Kleinrahm and W. Wagner, *Entwicklung und aufbau einer dichtemeßanlage zur messung der siede-und taudichten reiner fluider stoffe auf der gesamten phasengrenzkurve*. Forschung im Ingenieurwesen A, 1984. **50**(5): p. 166-166.
26. M.O. McLinden and C. Lösch-Will, *Apparatus for wide-ranging, high-accuracy fluid (p , ρ , T) measurements based on a compact two-sinker densimeter*. The Journal of Chemical Thermodynamics, 2007. **39**(4): p. 507-530.
27. K. Brachthäuser, *Entwicklung eines neuen dichtemessverfahrens für grosse temperatur-und druckbereiche und aufbau einer apparatur zur messung der dichte*

- fluider stoffe im temperaturbereich von -40°C bis + 250°C bei drücken bis zu 300 bar.*
1993.
28. W. Wagner, K. Brachthäuser, R. Kleinrahm, and H. Lösch, *A new, accurate single-sinker densitometer for temperatures from 233 to 523 K at pressures up to 30 MPa.* International Journal of Thermophysics, 1995. **16**(2): p. 399-411.
 29. M. McLinden, R.S.A. Hosseini, C. Will, and M. Richter. *Apparatus for high-temperature fluid mixture (p, ρ, T, x) measurements based on a single-sinker densimeter.* in *Eighteenth Symposium On Thermophysical Properties*. 2012. University of Colorado, Boulder, CO.
 30. D.E. Cristancho, I.D. Mantilla, S. Ejaz, K.R. Hall, M. Atilhan, and G.A. Iglesias-Silva, *Accurate $P\rho T$ data for methane from (300 to 450) K up to 180 MPa.* Journal of Chemical & Engineering Data, 2010. **55**(2): p. 826-829.
 31. D.E. Cristancho, I.D. Mantilla, S. Ejaz, K.R. Hall, M. Atilhan, and G.A. Iglesias-Silva, *Accurate $P\rho T$ data for ethane from (298 to 450) K up to 200 MPa.* Journal of Chemical & Engineering Data, 2010. **55**(8): p. 2746-2749.
 32. I.D. Mantilla, D.E. Cristancho, S. Ejaz, K.R. Hall, M. Atilhan, and G.A. Iglesias-Silva, *New $P-\rho-T$ data for nitrogen at temperatures from (265 to 400) K at pressures up to 150 MPa.* Journal of Chemical & Engineering Data, 2010. **55**(10): p. 4227-4230.
 33. I.D. Mantilla, D.E. Cristancho, S. Ejaz, K.R. Hall, M. Atilhan, and G.A. Iglesias-Silva, *$P-\rho-T$ data for carbon dioxide from (310 to 450) K up to 160 MPa.* Journal of Chemical & Engineering Data, 2010. **55**(11): p. 4611-4613.

34. M. Atilhan, S. Aparicio, S. Ejaz, D. Cristancho, and K.R. Hall, *PpT behavior of a lean synthetic natural gas mixture using magnetic suspension densimeters and an isochoric apparatus: Part i*. Journal of Chemical & Engineering Data, 2011. **56**(2): p. 212-221.
35. D.E. Cristancho, I.D. Mantilla, L.A. Coy, A. Tibaduiza, D.O. Ortiz-Vega, K.R. Hall, and G.A. Iglesias-Silva, *Accurate P–ρ–T data and phase boundary determination for a synthetic residual natural gas mixture*. Journal of Chemical & Engineering Data, 2011. **56**(4): p. 826-832.
36. C.R. Chamorro, J.J. Segovia, M.C. Martín, M.A. Villamañán, J.F. Estela-Urbe, and J.P.M. Trusler, *Measurement of the (pressure, density, temperature) relation of two (methane + nitrogen) gas mixtures at temperatures between 240 and 400 K and pressures up to 20 MPa using an accurate single-sinker densimeter*. Journal of Chemical Thermodynamics, 2006. **38**(7): p. 916-922.
37. W. Blanke, G. Klingenberg, and R. Weiss, *PVT Measurements on tetrafluoroethane (R134a) along the vapor-liquid equilibrium boundary between 288 and 373 K and in the liquid state from the triple point to 265 K*. International Journal of Thermophysics, 1995. **16**(5): p. 1143-1153.
38. W. Blanke, G. Klingenberg, and R. Weiss, *pvT Measurements on 1-chloro-1, 2, 2, 2-tetrafluoroethane (R124) along the gas– liquid boundary curve between 293 K and 395 K and in the liquid state from 120 K to 268 K*. Journal of Chemical & Engineering Data, 1996. **41**(3): p. 576-580.

39. GmbH Rubotherm, *Operating instructions- densitometer with magnetic suspension balance*. 1999: Bochum, Germany.
40. M. Atilhan, *High accuracy P - ρ - T measurements up to 200 MPa between 200 K and 500 K using a compact single sinker magnetic suspension densimeter for pure and natural gas like mixtures*. PhD. Dissertation. Texas A&M University, College Station, TX. 2007.
41. S. Ejaz, *High-accuracy P - ρ - T measurements of pure gas and natural gas like mixtures using a compact magnetic suspension densimeter*. PhD Dissertation. Texas A&M University, College Station, TX. 2007.
42. M.O. McLinden, R. Kleinrahm, and W. Wagner, *Force transmission errors in magnetic suspension densimeters*. International Journal of Thermophysics, 2007. **28**(2): p. 429-448.
43. D.E. Cristancho, I.D. Mantilla, S. Ejaz, K.R. Hall, G.A. Iglesias-Silva, and M. Atilhan, *Force transmission error analysis for a high-pressure single-sinker magnetic suspension densimeter*. International Journal of Thermophysics, 2010. **31**(4): p. 698-709.
44. D. Cristancho, I. Mantilla, S. Ejaz, K. Hall, G. Iglesias-Silva, and M. Atilhan, *Force transmission error analysis for a high-pressure single-sinker magnetic suspension densimeter*. International Journal of Thermophysics, 2010. **31**(4-5): p. 698-709.
45. M.E. Mondéjar, J.J. Segovia, and C.R. Chamorro, *Improvement of the measurement uncertainty of a high accuracy single sinker densimeter via setup*

- modifications based on a state point uncertainty analysis.* Measurement, 2011. **44**(9): p. 1768-1780.
46. M. Richter, M.A. Ben Souissi, R. Span, and P. Schley, *Accurate (p, ρ, T, x) measurements of hydrogen-enriched natural-gas mixtures at $T = (273.15, 283.15, \text{ and } 293.15) \text{ K}$ with pressures up to 8 MPa.* Journal of Chemical & Engineering Data, 2014. **59**(6): p. 2021-2029.
47. R. Span, E.W. Lemmon, R.T. Jacobsen, W. Wagner, and A. Yokozeki, *A reference equation of state for the thermodynamic properties of nitrogen for temperatures from 63.151 to 1000 K and pressures to 2200 MPa.* Journal of Physical and Chemical Reference Data, 2000. **29**(6): p. 1361-1433.
48. R. Span and W. Wagner, *A new equation of state for carbon dioxide covering the fluid region from the triple-point temperature to 1100 K at pressures up to 800 MPa.* Journal of Physical and Chemical Reference Data, 1996. **25**(6): p. 1509-1596.
49. C. Tegeler, R. Span, and W. Wagner, *A new equation of state for argon covering the fluid region for temperatures from the melting line to 700 K at pressures up to 1000 MPa.* Journal of Physical and Chemical Reference Data, 1999. **28**(3): p. 779-850.
50. D.O. Ortiz-Vega, K.R. Hall, V.D. Arp, and E.W. Lemmon, *Interim equation, a new wide range equation of state for helium-4.* International Journal of Thermophysics, 2010.

51. A. Michels, H. Wijker, and H. Wijker, *Isotherms of argon between 0°C and 150°C and pressures up to 2900 atmospheres*. *Physica*, 1949. **15**(7): p. 627-633.
52. A.L. Blancett, K.R. Hall, and F.B. Canfield, *Isotherms for the He-Ar system at 50° C, 0° C and -50° C up to 700 atm*. *Physica*, 1970. **47**(1): p. 75-91.
53. T. Briggs, *Compressibility data for helium over the temperature range -5°c to 80°c and at pressures to 800 atmospheres*. 1970, Bureau of Mines, Washington, DC (USA).
54. R. Wiebe, V. Gaddy, and C. Heins, *The compressibility isotherms of helium at temperatures from -70 to 200 and at pressures to 1000 atmospheres*. *Journal of the American Chemical Society*, 1931. **53**(5): p. 1721-1725.
55. R. Hernández-Gómez, D. Tuma, J.J. Segovia, and C.R. Chamorro, *Experimental determination of (p, ρ, T) data for binary mixtures of methane and helium*. *The Journal of Chemical Thermodynamics*, 2016. **96**: p. 1-11.
56. R. Hernández-Gómez, D. Tuma, R. Villamañán, and C.R. Chamorro, *Accurate experimental (p, ρ, T) values and virial coefficients for the (methane and helium) binary system*. *The Journal of Chemical Thermodynamics*, 2016. **101**: p. 168-179.
57. O. Kunz and W. Wagner, *The GERG-2008 wide-range equation of state for natural gases and other mixtures: An expansion of GERG-2004*. *Journal of Chemical and Engineering Data*, 2012. **57**(11): p. 3032-3091.
58. K. Starling and J. Savidge, *AGA transmission measurement committee Report Number 8*. 1992, American Gas Association, Virginia, USA.

59. G. Soave, *Application of a cubic equation of state to vapor-liquid equilibria of systems containing polar compounds*. Institution of Chemical Engineers Symposium Series. 1979.
60. D. Peng and D.B. Robinson, *A new two-constant equation of state*. Industrial & Engineering Chemistry Fundamentals, 1976. **15**(1): p. 59-64.
61. J.H. Keenan, *Steam tables: Thermodynamic properties of water, including vapor, liquid, and solid phases (english units)*. 1969: Wiley.
62. R. Pollak, *New fundamental equation for consistent representation of thermodynamic properties of water*. Brennstoff-Warme-Kraft, 1975. **27**(5): p. 210-215.
63. L. Haar and J.S. Gallagher, *Thermodynamic properties of ammonia*. Journal of Physical and Chemical Reference Data, 1978. **7**(3): p. 635-792.
64. R. Schmidt and W. Wagner, *A new form of the equation of state for pure substances and its application to oxygen*. Fluid Phase Equilibria, 1985. **19**(3): p. 175-200.
65. M. Jaeschke, A. Benito, A. Fredheim, J.M. Henault, B. Viglietti, P. van Wesenbeeck, R. Klimeck, O. Kunz, and W. Wagner, *GERG project: wide-range reference equation of state for natural gases*. GWF, Gas - Erdgas, 2003. **144**(7-8): p. 430-435.
66. M. Atilhan, S. Aparicio, S. Ejaz, D. Cristancho, I. Mantilla, and K.R. Hall, *p - ρ - T behavior of three lean synthetic natural gas mixtures using a magnetic suspension densimeter and isochoric apparatus from (250 to 450) K with pressures up to 150*

- MPa: part ii*. Journal of Chemical & Engineering Data, 2011. **56**(10): p. 3766-3774.
67. H. Rutishauser, and A. Reichmuth, *The new METTLER AT analytical balance*. 1988, Mettler Instruments AG.
68. J. Klimeck, R. Kleinrahm, and W. Wagner, *An accurate single-sinker densimeter and measurements of the (p, ρ, T) relation of argon and nitrogen in the temperature range from (235 to 520) K at pressures up to 30 MPa*. The Journal of Chemical Thermodynamics, 1998. **30**(12): p. 1571-1588.
69. H. Preston-Thomas, *The international temperature scale of 1990 (ITS-90)*. Metrologia, 1990. **27**(1): p. 3.
70. Minco, *Report of calibration for platinum resistance thermometer model S1059-2, Serial Number 204*, 2000: Friedley, Minnesota.
71. M.S. Izidro, *Real-time labview assessment on adsorption systems*. Masters Thesis. Universidade Nova de Lisboa. 2014
72. D.A. Osage, C.D. Rodery, T.P. Pastor, R.G. Brown, P.A. Henry, and J.C. Sowinski, *SECTION VIII: Division 2–Alternative Rules*, in *Companion Guide to the ASME Boiler and Pressure Vessel Code Fourth Edition*, K.R. Rao, Editor. 2012. p. 22-55.56.
73. D. Edwards, *Temperature and strain rate effects in high strength high conductivity copper alloys tested in air*. 1998, Oak Ridge National Lab., TN (United States).

74. R. Weggel, J.O. Ratka, W. Spiegelberg, and Y. Sakai, *Strength of Hycon 3 HP Be-Cu and other copper alloys from 20° C to 200° C*. *Magnetics, IEEE Transactions on*, 1994. **30**(4): p. 2188-2191.
75. D.O. Ortiz-Vega, I.D. Mantilla, H.Y. Acosta, M.A. Gomez-Osorio, J.C. Holste, K.R. Hall, and G.A. Iglesias-Silva, *Uncertainty estimates for experimental density measurements: Effects of temperature, pressure and sample preparation*. *The Journal of Chemical Thermodynamics*, 2013. **58**: p. 14-19.
76. P.T. Eubank and K.R. Hall, *Optimum mixture compositions for measurement of cross virial coefficients*. *AIChE Journal*, 1990. **36**(11): p. 1661-1668.
77. S.I. Sandier, H. Orbey, J.V. Sengers, and R.F. Kayser, *9 Mixing and combining rules equations of state for fluids and fluid mixtures*. Vol. 5. 2000. 321-357.
78. D.R. McGregor, J.C. Holste, P.T. Eubank, K.N. Marsh, K.R. Hall, and J. Schouten, *An interaction model for third virial coefficients which provides simplified equations for mixtures*. *Fluid Phase Equilibria*, 1987. **35**(1-3): p. 153-164.
79. P. Bishnoi and D. Robinson, *Mixing rules improve BWR use*. *Hydrocarbon Processing*, 1972. **51**(11): p. 152-&.
80. J.M. Smith, H.C. Van Ness, and M.M. Abbott, *Introduction to chemical engineering thermodynamics* 6th ed. McGraw-Hill Chemical Engineering Series, ed. McGraw-Hill. 2001, New York, NY: McGraw-Hill.
81. E.W. Lemmon and R.T. Jacobsen, *A generalized model for the thermodynamic properties of mixtures*. *International Journal of Thermophysics*, 1999. **20**(3): p. 825-835.

82. N.F. Carnahan and K.E. Starling, *Equation of state for nonattracting rigid spheres*. The Journal of Chemical Physics, 1969. **51**(2): p. 635-636.
83. N.F. Carnahan and K.E. Starling, *Intermolecular repulsions and the equation of state for fluids*. AIChE Journal, 1972. **18**(6): p. 1184-1189.
84. N.D. Kosov and I.S. Brovanov, *Compressibility of a binary mixture of argon and nitrogen at different concentrations in the 59–590 bar pressure range*. Journal of Engineering Physics, 1979. **36**(4): p. 413-417.
85. U. Setzmann and W. Wagner, *A new equation of state and tables of thermodynamic properties for methane covering the range from the melting line to 625 K at pressures up to 100 MPa*. Journal of Physical and Chemical Reference Data, 1991. **20**(6): p. 1061-1155.
86. D. Bücker and W. Wagner, *A reference equation of state for the thermodynamic properties of ethane for temperatures from the melting line to 675 K and pressures up to 900 MPa*. Journal of Physical and Chemical Reference Data, 2006. **35**(1): p. 205-266.
87. J.W. Leachman, R.T. Jacobsen, S. Penoncello, and E. Lemmon, *Fundamental equations of state for parahydrogen, normal hydrogen, and orthohydrogen*. Journal of Physical and Chemical Reference Data, 2009. **38**(3): p. 721-748.
88. E.W. Lemmon and R. Span, *Short fundamental equations of state for 20 industrial fluids*. Journal of Chemical & Engineering Data, 2006. **51**(3): p. 785-850.

89. E. Lemmon, M. Huber, and M. McLinden, *NIST reference database 23: Reference fluid thermodynamic and transport properties-REFPROP, version 9.1*. National Institute of Standards and Technology, Standard Reference Data Program, 2013.
90. P.J. McElroy and J. Fang, *Compression factors and virial coefficients of (methane + ethane)*. *The Journal of Chemical Thermodynamics*, 1994. **26**(6): p. 617-623.
91. E. Hala, V. Fried, and O. Vilim, *Vapour-liquid equilibrium*. 2nd ed. 1967, New York, NY: Standard, Pergamon Press.
92. H. Achtermann, T. Bose, H. Rögener, and J. St-Arnaud, *Precise determination of the compressibility factor of methane, nitrogen, and their mixtures from refractive index measurements*. *International Journal of Thermophysics*, 1986. **7**(3): p. 709-720.
93. P.W. Townsend, *Pressure-volume-temperature relationships of binary gaseous mixtures*. Columbia University. 1956
94. L. Lialine, P. Hestermans, and L. Deffet. *De-termination of the Compressibility of a Hydrogen-Nitrogen Mixture by a Method Suitable for the Study of Industrial Gases*. in *Joint Conf. of Thermodynamic and Transport Properties of Fluids*, IUPAC, London. 1957.
95. W.E. Deming and L.E. Shupe, *The Beattie-Bridgeman equation of state and Bartlett's PVT data on a 3: 1 hydrogen-nitrogen mixture*. *Journal of the American Chemical Society*, 1931. **53**(3): p. 860-869.

96. D.D. Dillard, M. Waxman, and R.L. Robinson Jr, *Volumetric data and virial coefficients for helium, krypton, and helium-krypton mixtures*. Journal of Chemical and Engineering Data, 1978. **23**(4): p. 269-274.
97. T.C. Briggs and A.R. Howard, *Compressibility data for helium, nitrogen, and helium-nitrogen mixtures at 0, 250, and 500 C and at pressures to 1,000 atmospheres*. Vol. 7639. 1972: US Department of Interior, Bureau of Mines.
98. P.S. Ku and B.F. Dodge, *Compressibility of the binary systems: Helium-nitrogen and carbon dioxide-ethylene*. Journal of Chemical and Engineering Data, 1967. **12**(2): p. 158-164.
99. J.E. Miller, L.W. Brandt, and L. Stroud, *Compressibility factors for helium and helium-nitrogen mixtures*. Vol. 5845. 1961: US Department of the Interior, Bureau of Mines.

APPENDIX A

O-RING AND BACK-UP RING DRAWING

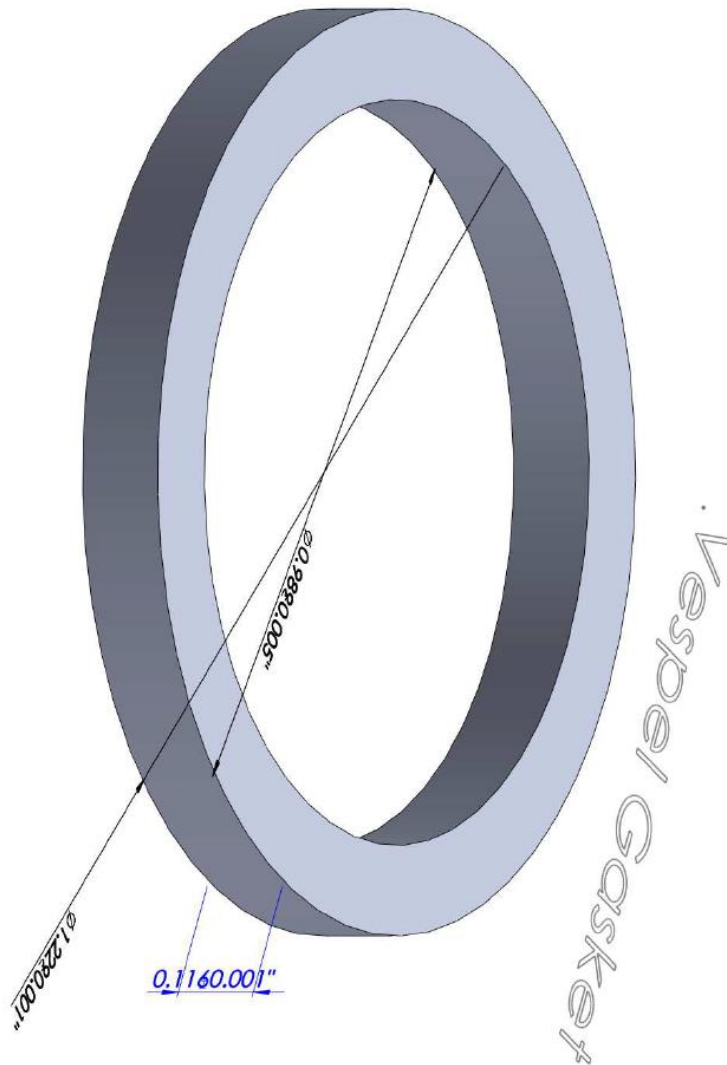


Figure A.1 Vespel O-ring drawing with dimensions

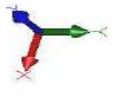


Figure A.2 Copper back-up ring drawing with dimensions

APPENDIX C

VOLTAGE VALUES FOR THE CONTROL SYSTEM

Table C.1 Expected and nominal voltage readings for the magnetic suspension densimeter control system

Signal	Nominal Value in Voltage	Measured Value in Voltage
- 15 V	- 15 ± 0.5 V	- 14.85 V
+ 15 V	+15 ± 0.5 V	+15.06 V
+ 18 V	+18 ± 0.5 V	+17.37 V
- 18 V	- 18 ± 0.5 V	-17.58 V
U _s	-5.6 V	- 5.60 V
U _a	5.6 V	+ 5.60 V
U _{ag}	0.0 V	0.00 V
U _R	0.1 V	- 0.11 V
U _m	0.0 V	0.00 V
U _{KSH}	0.0 V	0.00 V
U _{KSR}	0.0 V	0.00 V

APPENDIX D

SHIELD AND SUPPORT DRAWINGS

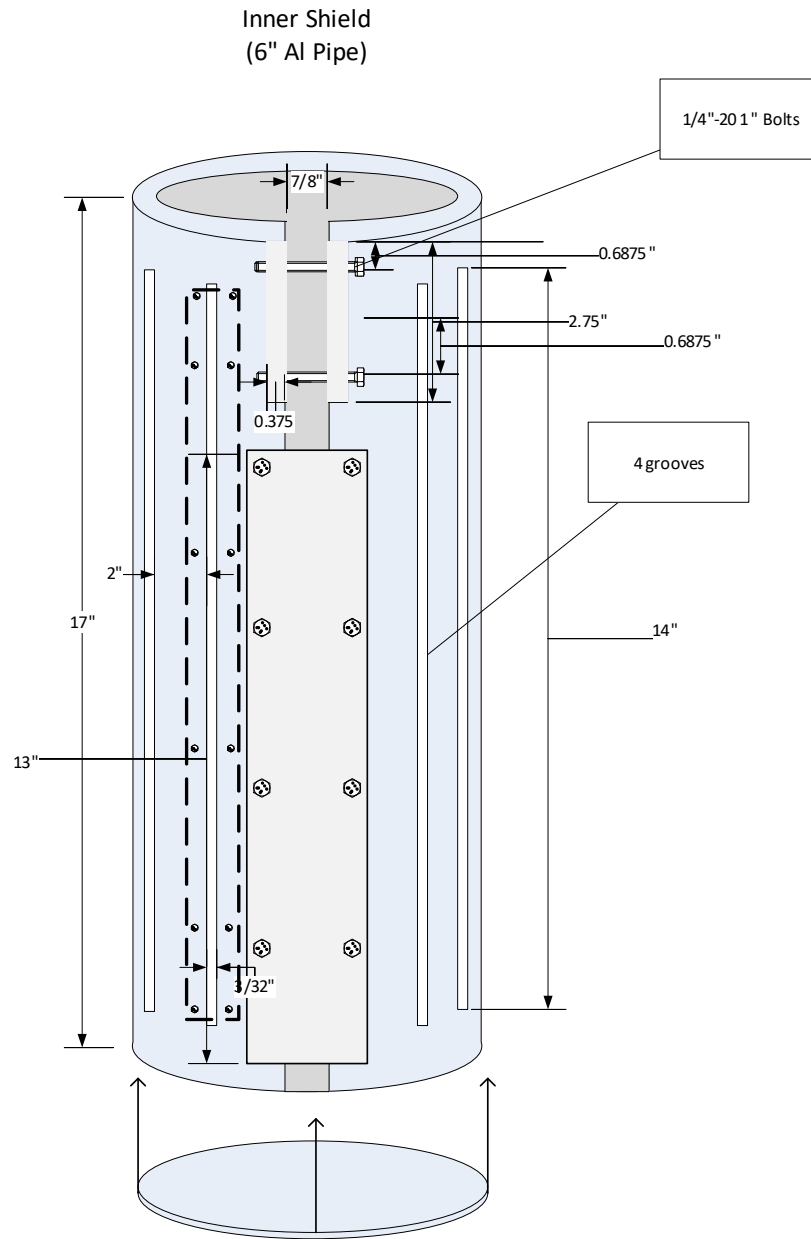


Figure D.1 Inner Shield Drawing

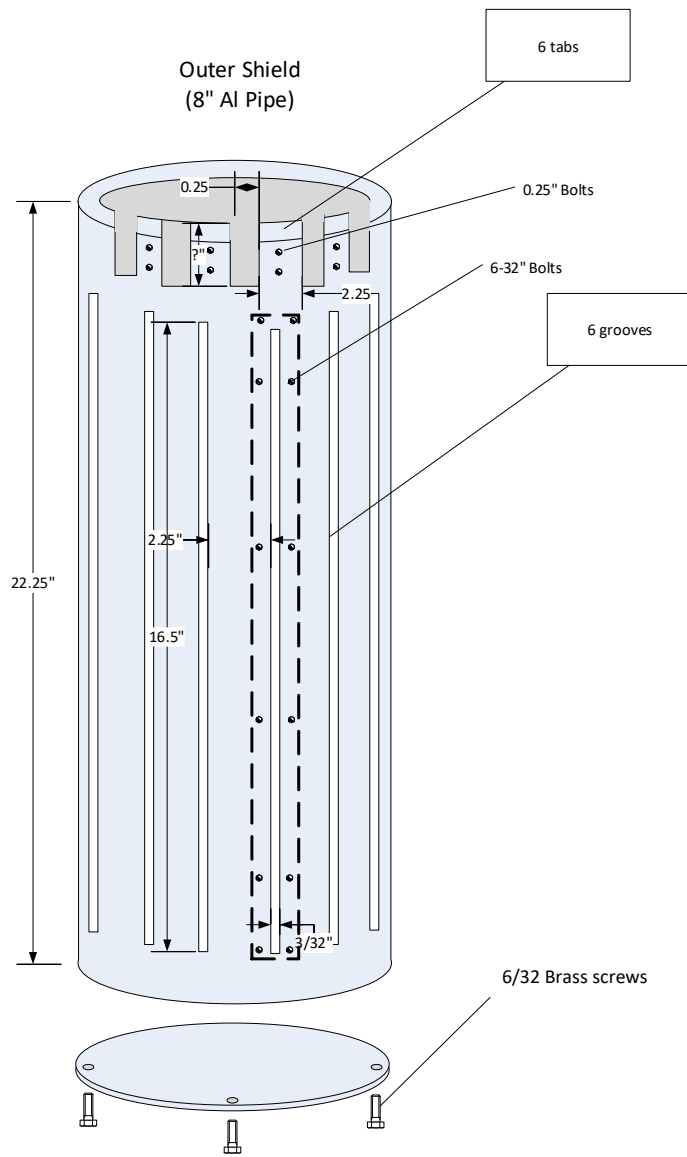


Figure D.2 Outer Shield Drawing

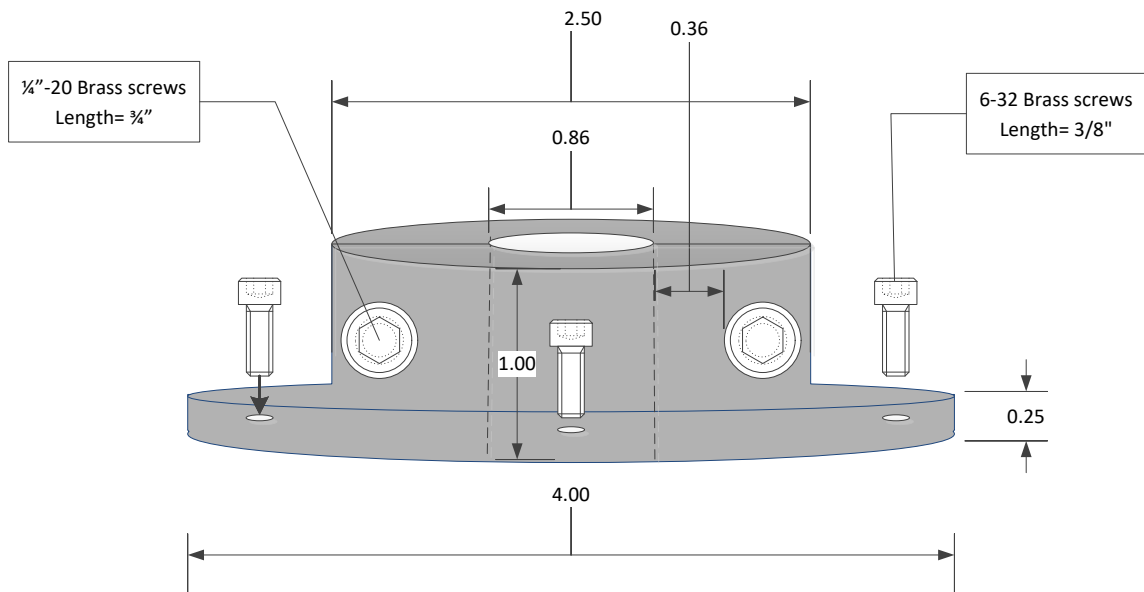


Figure D.4 Outer shield EM clamp

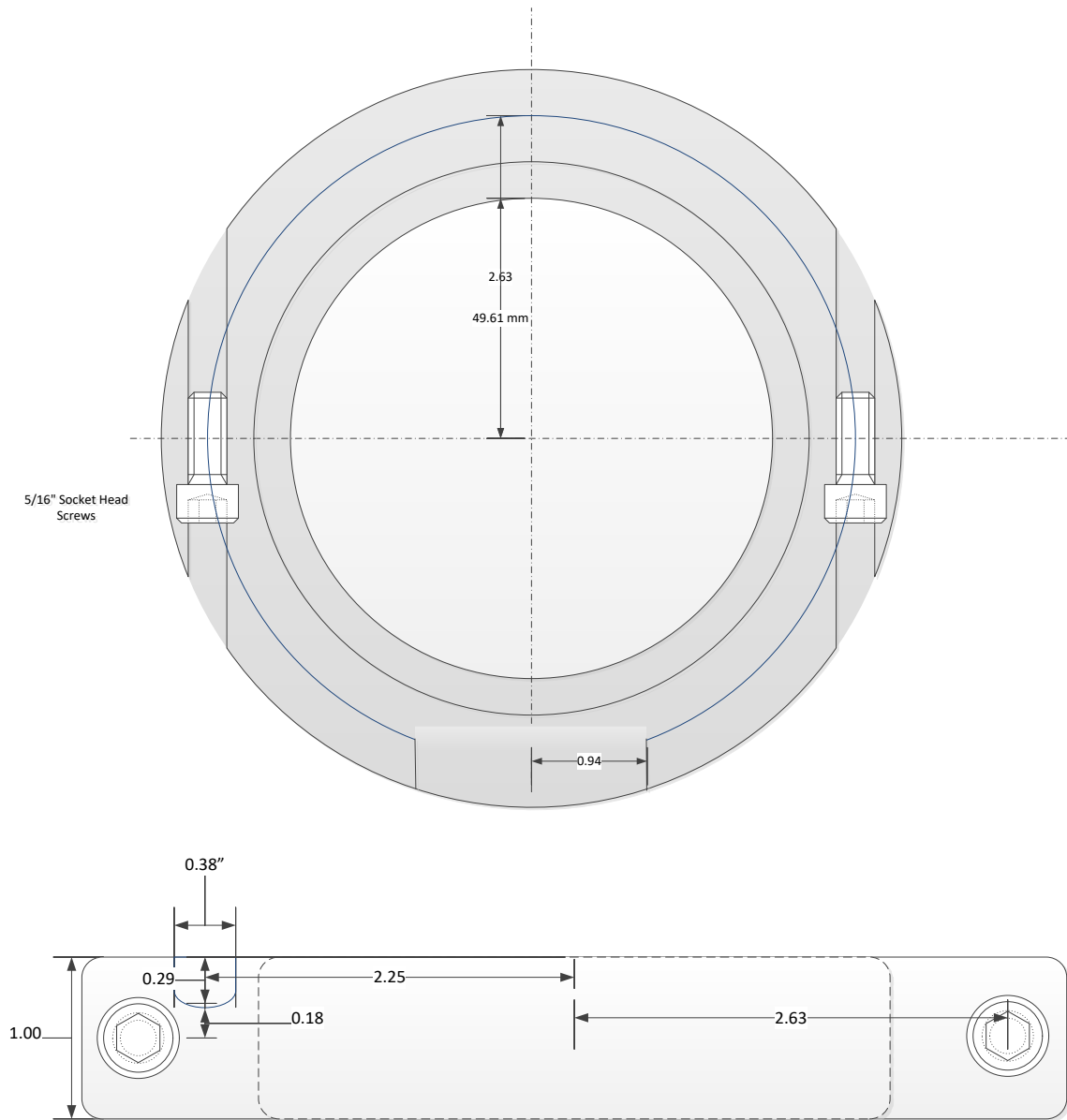


Figure D.5 Cell heater support drawing

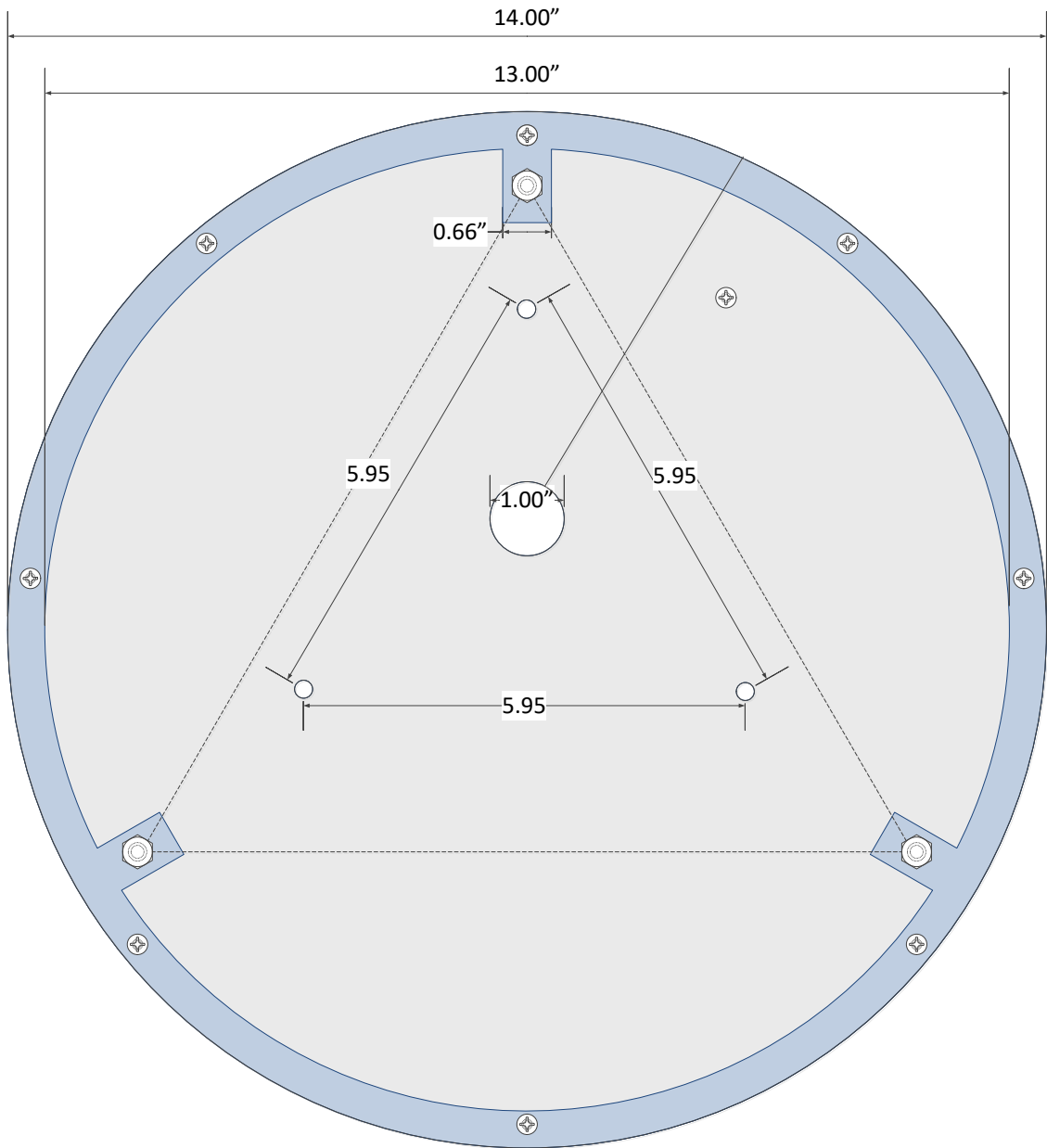


Figure D.6 Upper radiation shield drawing top ring, bottom view

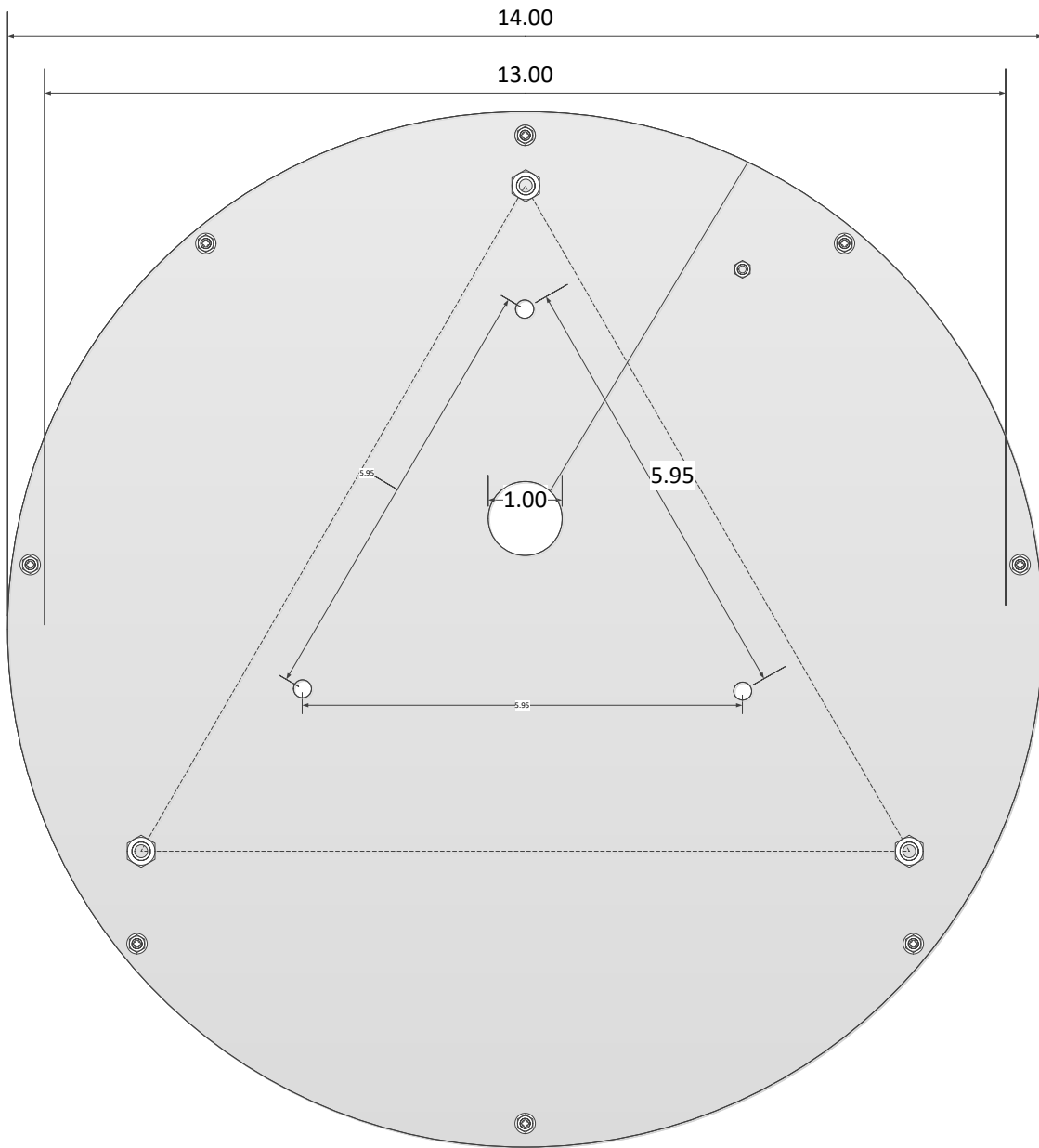


Figure D.7 Upper radiation shield drawing top ring, top view

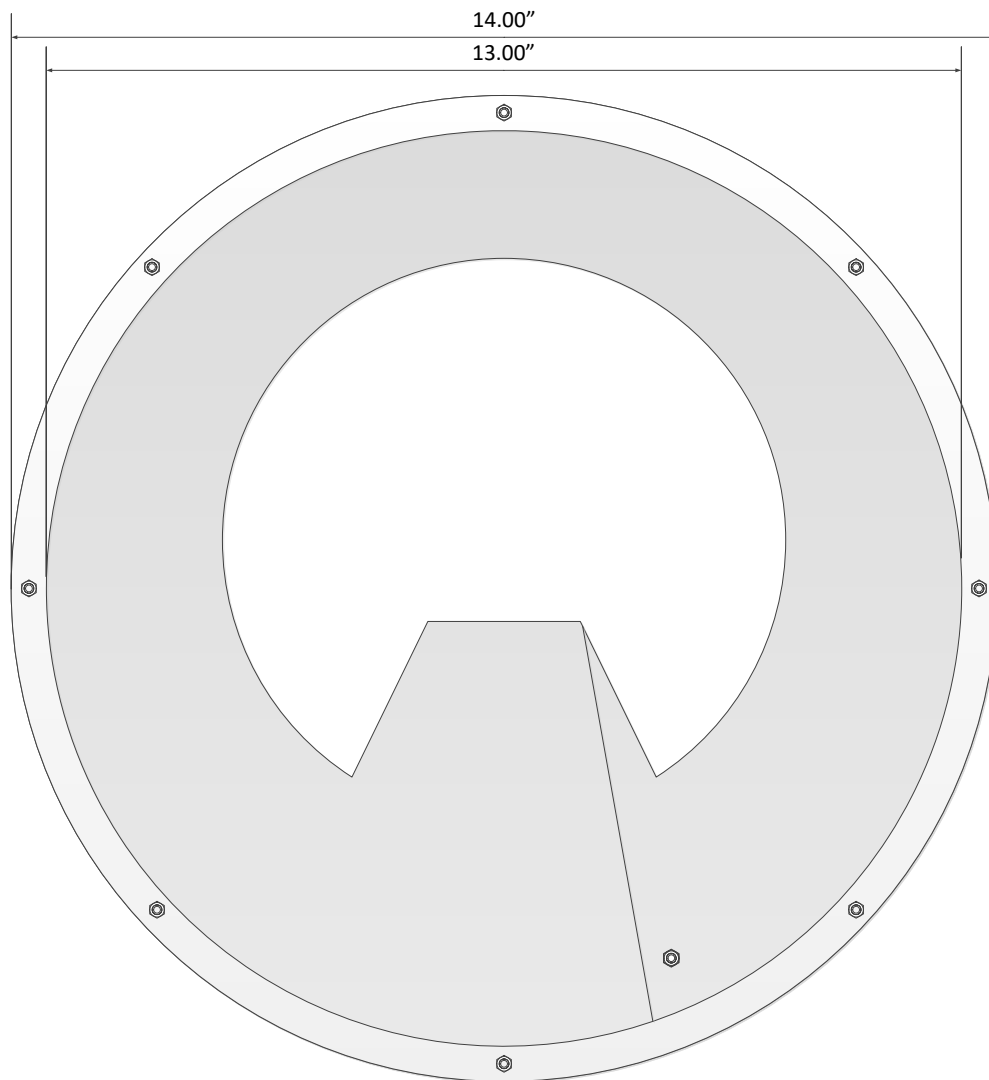


Figure D.8 Upper radiation shield drawing bottom ring, bottom view

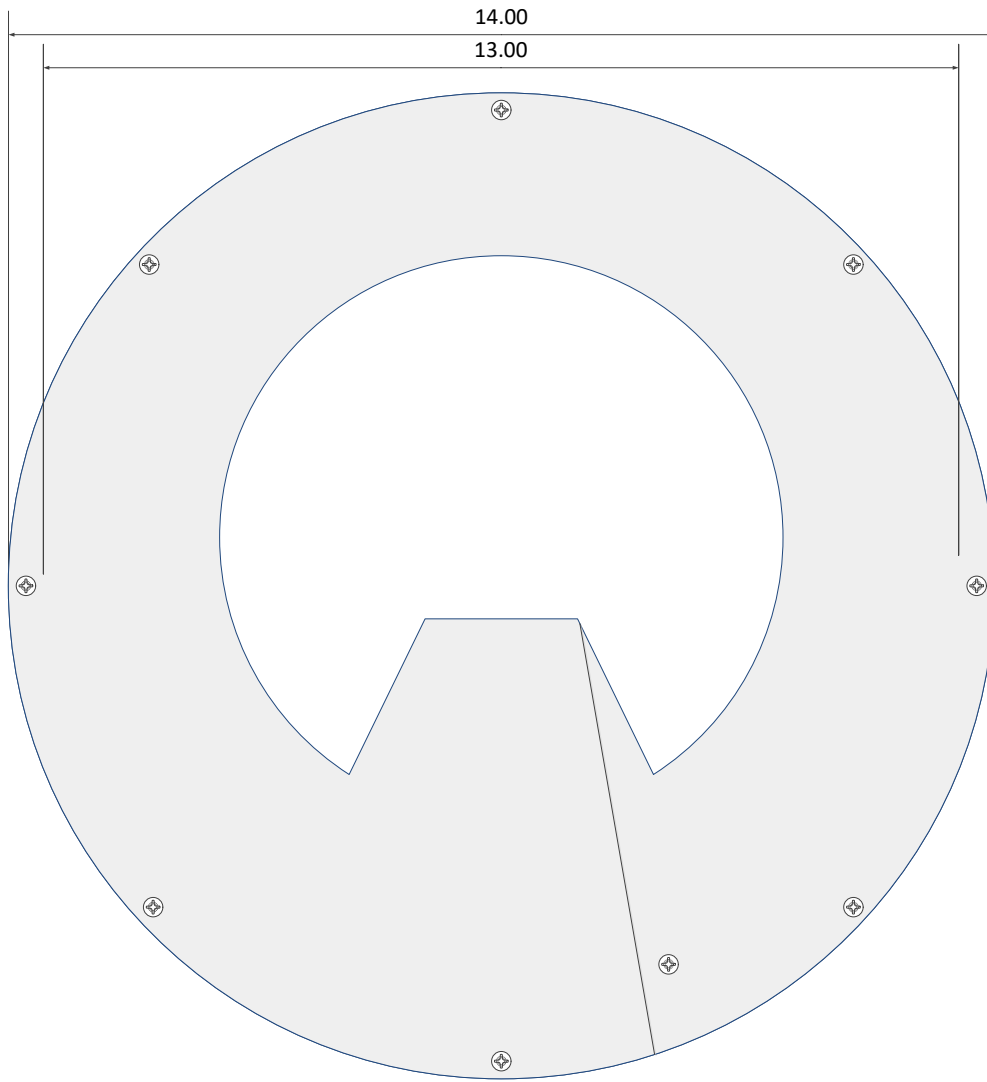


Figure D.9 Upper radiation shield drawing bottom ring, top view

APPENDIX E

SPRT CALIBRATION AND ITS-90 COEFFICIENTS

The International Temperature Scale (ITS-90) is designed to characterize the absolute thermodynamic scale in the range of 0.65 K to 1358 K. Thermodynamic equilibrium states of fourteen pure chemical elements and degassed water are used to determine reference temperature points in ITS-90 scale. These defined reference points are used to calibrate thermometers. Some formulas are used to interpolate between the reference points.

ITS-90 expresses the temperature in Kelvin in terms of the ratio of the measured resistance of the SPRT at the temperature and its resistance at triple point of water; 273.16 K:

$$W(T) = \frac{R(T)}{R(273.16K)} \quad (\text{E.1})$$

The deviation equation given by equation E.2 and reference function given by equation E.3 are used to calculate the temperature below 273.16 K.

$$W_{ref}(T) = W(T) - a_4[W(T) - 1] - b_4[W(T) - 1]\ln(W(T)) \quad (\text{E.2})$$

$$\frac{T}{273.16K} = B_0 + \sum_1^{15} B_i \left[\frac{W_{ref}(T)^{1/6} - 0.65}{0.35} \right]^i \quad (\text{E.3})$$

The deviation equation given by equation E.4 and the reference function given by equation E.5 is used to calculate the temperature above 273.16 K.

$$W_{ref}(T) = W(T) - a_8[W(T) - 1] - b_8[W(T) - 1]^2 \quad (\text{E.4})$$

$$\frac{T}{273.16K} = D_0 + \sum_1^9 D_i \left[\frac{W_{ref}(T)^{1/6} - 2.64}{1.64} \right]^i \quad (\text{E.5})$$

The constants a_4 , b_4 , a_8 and b_8 were determined by Minco by calibrating the SPRT at fixed temperature points defined by ITS-90. These constants and values of the constants B_i and D_i are given in Table E.1. The resistance of the SPRT at the triple point of water measured during the original calibration done by Minco was $R(273.16\text{K}) = 100.4244 \Omega$.

Table E. 1 ITS-90 coefficients

Constants in Deviation Equations and Reference Functions of ITS-90

a_4	-0.000418264140	B_0	0.183324722
b_4	0.000080228227	B_1	0.240975303
a_8	-0.000568113400	B_2	0.209108771
b_8	0.000260761350	B_3	0.190439972
		B_4	0.142648498
		B_5	0.077993465
D_0	439.932854	B_6	0.012475611
D_1	472.418020	B_7	-0.032267127
D_2	37.6844940	B_8	-0.075291522
D_3	7.472018	B_9	-0.056470670
D_4	2.920828	B_{10}	0.076201285
D_5	0.005184	B_{11}	0.123893204
D_6	-0.963864	B_{12}	-0.029201193
D_7	-0.188732	B_{13}	-0.091173542
D_8	0.191203	B_{14}	0.001317696
D_9	0.049025	B_{15}	0.026025526

APPENDIX F

Pressure transducer calibration coefficients

CALIBRATION COEFFICIENTS		SERIAL NO : 80872	
PRESSURE TRANSDUCER		DATE : 03-13-2001	
MODEL :	PRESSURE RANGE :	TEMP. RANGE :	PORT :
430K-101	0 to 30000 psia	0 to 50 deg C	

<p>TEMPERATURE COEFFICIENTS</p> <p>X = temperature period (μsec)</p> <p>U = X - U₀</p> <p>Temperature : (deg C)</p> <p>Temp = Y₁U + Y₂U² + Y₃U³</p> <p>PRESSURE COEFFICIENTS</p> <p>T = pressure period (μsec)</p> <p>C = C₁ + C₂U + C₃U²</p> <p>D = D₁ + D₂U</p> <p>T₀ = T₁ + T₂U + T₃U² + T₄U³ + T₅U⁴</p> <p>Pressure : (psia)</p> $P = C \left(1 - \frac{T_0^2}{T^2}\right) \left(1 - D \left(1 - \frac{T_0^2}{T^2}\right)\right)$	<table border="1" style="width: 100%; border-collapse: collapse;"> <tr><td>U₀</td><td>5.885922</td><td>μsec</td></tr> <tr><td>Y₁</td><td>-3931.764</td><td>deg C/μsec</td></tr> <tr><td>Y₂</td><td>-9249.725</td><td>deg C/μsec^2</td></tr> <tr><td>Y₃</td><td>0</td><td></td></tr> </table> <table border="1" style="width: 100%; border-collapse: collapse;"> <tr><td>C₁</td><td>-140860.4</td><td>psia</td></tr> <tr><td>C₂</td><td>-7430.274</td><td>psia/μsec</td></tr> <tr><td>C₃</td><td>462172.9</td><td>psia/μsec^2</td></tr> </table> <table border="1" style="width: 100%; border-collapse: collapse;"> <tr><td>D₁</td><td>0.019458</td><td></td></tr> <tr><td>D₂</td><td>0</td><td></td></tr> </table> <table border="1" style="width: 100%; border-collapse: collapse;"> <tr><td>T₁</td><td>30.10170</td><td>μsec</td></tr> <tr><td>T₂</td><td>0.521056</td><td>$\mu\text{sec}/\mu\text{sec}$</td></tr> <tr><td>T₃</td><td>57.57619</td><td>$\mu\text{sec}/\mu\text{sec}^2$</td></tr> <tr><td>T₄</td><td>-294.5308</td><td>$\mu\text{sec}/\mu\text{sec}^3$</td></tr> <tr><td>T₅</td><td>0</td><td></td></tr> </table> <p style="text-align: right;">(03-13-2001)</p>	U ₀	5.885922	μsec	Y ₁	-3931.764	deg C/ μsec	Y ₂	-9249.725	deg C/ μsec^2	Y ₃	0		C ₁	-140860.4	psia	C ₂	-7430.274	psia/ μsec	C ₃	462172.9	psia/ μsec^2	D ₁	0.019458		D ₂	0		T ₁	30.10170	μsec	T ₂	0.521056	$\mu\text{sec}/\mu\text{sec}$	T ₃	57.57619	$\mu\text{sec}/\mu\text{sec}^2$	T ₄	-294.5308	$\mu\text{sec}/\mu\text{sec}^3$	T ₅	0	
U ₀	5.885922	μsec																																									
Y ₁	-3931.764	deg C/ μsec																																									
Y ₂	-9249.725	deg C/ μsec^2																																									
Y ₃	0																																										
C ₁	-140860.4	psia																																									
C ₂	-7430.274	psia/ μsec																																									
C ₃	462172.9	psia/ μsec^2																																									
D ₁	0.019458																																										
D ₂	0																																										
T ₁	30.10170	μsec																																									
T ₂	0.521056	$\mu\text{sec}/\mu\text{sec}$																																									
T ₃	57.57619	$\mu\text{sec}/\mu\text{sec}^2$																																									
T ₄	-294.5308	$\mu\text{sec}/\mu\text{sec}^3$																																									
T ₅	0																																										

<p>PAROSCIENTIFIC, INC.</p> <p>4500 148th AVENUE N.E. REDMOND, WA. 98052</p>	<p>CUSTOMER : TEXAS A&M UNIVERSITY</p> <p>SALES ORDER : 17655 PREPARED BY : CME</p>
---	---

Figure F.1 Pressure transducer calibration for the 30 k transducer

CALIBRATION COEFFICIENTS		SERIAL NO : 84267	
PRESSURE TRANSDUCER		DATE : 03-13-2001	
MODEL : 46K-101	PRESSURE RANGE : 0 to 6000 psia	TEMP. RANGE : 0 to 125 deg C	PORT :

<p>TEMPERATURE COEFFICIENTS</p> <p>X = temperature period (μsec)</p> <p>$U = X - U_0$</p> <p>Temperature : (deg C)</p> <p>Temp = $Y_1U + Y_2U^2 + Y_3U^3$</p> <p>PRESSURE COEFFICIENTS</p> <p>T = pressure period (μsec)</p> <p>$C = C_1 + C_2U + C_3U^2$</p> <p>$D = D_1 + D_2U$</p> <p>$T_0 = T_1 + T_2U + T_3U^2 + T_4U^3 + T_5U^4$</p> <p>Pressure : (psia)</p> <p>$P = C \left(1 - \frac{T_0^2}{T^2}\right) \left(1 - D \left(1 - \frac{T_0^2}{T^2}\right)\right)$</p>	<table border="1" style="width: 100%; border-collapse: collapse;"> <tr><td>U₀</td><td>5.872036</td><td>μsec</td></tr> <tr><td>Y₁</td><td>-3921.533</td><td>deg C/μsec</td></tr> <tr><td>Y₂</td><td>-11539.00</td><td>deg C/μsec^2</td></tr> <tr><td>Y₃</td><td>0</td><td></td></tr> </table> <table border="1" style="width: 100%; border-collapse: collapse;"> <tr><td>C₁</td><td>-23214.56</td><td>psia</td></tr> <tr><td>C₂</td><td>564.4182</td><td>psia/μsec</td></tr> <tr><td>C₃</td><td>73606.34</td><td>psia/μsec^2</td></tr> </table> <table border="1" style="width: 100%; border-collapse: collapse;"> <tr><td>D₁</td><td>0.037428</td><td></td></tr> <tr><td>D₂</td><td>0</td><td></td></tr> </table> <table border="1" style="width: 100%; border-collapse: collapse;"> <tr><td>T₁</td><td>30.03705</td><td>μsec</td></tr> <tr><td>T₂</td><td>1.415628</td><td>$\mu\text{sec}/\mu\text{sec}$</td></tr> <tr><td>T₃</td><td>59.87418</td><td>$\mu\text{sec}/\mu\text{sec}^2$</td></tr> <tr><td>T₄</td><td>190.2078</td><td>$\mu\text{sec}/\mu\text{sec}^3$</td></tr> <tr><td>T₅</td><td>0</td><td></td></tr> </table> <p style="text-align: right;">(03-13-2001)</p>	U ₀	5.872036	μsec	Y ₁	-3921.533	deg C/ μsec	Y ₂	-11539.00	deg C/ μsec^2	Y ₃	0		C ₁	-23214.56	psia	C ₂	564.4182	psia/ μsec	C ₃	73606.34	psia/ μsec^2	D ₁	0.037428		D ₂	0		T ₁	30.03705	μsec	T ₂	1.415628	$\mu\text{sec}/\mu\text{sec}$	T ₃	59.87418	$\mu\text{sec}/\mu\text{sec}^2$	T ₄	190.2078	$\mu\text{sec}/\mu\text{sec}^3$	T ₅	0	
U ₀	5.872036	μsec																																									
Y ₁	-3921.533	deg C/ μsec																																									
Y ₂	-11539.00	deg C/ μsec^2																																									
Y ₃	0																																										
C ₁	-23214.56	psia																																									
C ₂	564.4182	psia/ μsec																																									
C ₃	73606.34	psia/ μsec^2																																									
D ₁	0.037428																																										
D ₂	0																																										
T ₁	30.03705	μsec																																									
T ₂	1.415628	$\mu\text{sec}/\mu\text{sec}$																																									
T ₃	59.87418	$\mu\text{sec}/\mu\text{sec}^2$																																									
T ₄	190.2078	$\mu\text{sec}/\mu\text{sec}^3$																																									
T ₅	0																																										

<p>PAROSCIENTIFIC, INC. 4500 148th AVENUE N.E. REDMOND, WA. 98052</p>	<p>CUSTOMER : TEXAS A&M UNIVERSITY</p>	<p style="text-align: right;">SALES ORDER : 17655 PREPARED BY : CME</p>
--	---	--

Figure F.2 Pressure transducer calibration for the 6 k transducer

CALIBRATION COEFFICIENTS		SERIAL NO : 106030	
PRESSURE TRANSDUCER		DATE : 10-24-2007	
MODEL :	PRESSURE RANGE :	TEMP. RANGE :	PORT :
410K-101	0 to 10000 psia	0 to 125 deg C	

TEMPERATURE COEFFICIENTS		U_0	5.759152	μsec
$X =$ temperature period (μsec)		Y_1	-3996.592	$\text{deg C}/\mu\text{sec}$
$U = X - U_0$		Y_2	-11654.91	$\text{deg C}/\mu\text{sec}^2$
Temperature : (deg C)		Y_3	0	
$\text{Temp} = Y_1U + Y_2U^2 + Y_3U^3$				
PRESSURE COEFFICIENTS		C_1	-48519.30	psia
$T =$ pressure period (μsec)		C_2	1198.666	$\text{psia}/\mu\text{sec}$
$C = C_1 + C_2U + C_3U^2$		C_3	146458.9	$\text{psia}/\mu\text{sec}^2$
$D = D_1 + D_2U$		D_1	0.036784	
$T_0 = T_1 + T_2U + T_3U^2 + T_4U^3 + T_5U^4$		D_2	0	
Pressure : (psia)		T_1	29.99754	μsec
$P = C \left(1 - \frac{T_0^2}{T^2}\right) \left(1 - D \left(1 - \frac{T_0^2}{T^2}\right)\right)$		T_2	1.518527	$\mu\text{sec}/\mu\text{sec}$
		T_3	47.46710	$\mu\text{sec}/\mu\text{sec}^2$
		T_4	-15.23986	$\mu\text{sec}/\mu\text{sec}^3$
		T_5	0	
				(10-24-2007)


PAROSCIENTIFIC, INC. 4500 148th AVENUE N.E. REDMOND, WA. 98052	CUSTOMER : TEXAS A&M UNIVERSITY	
	SALES ORDER : 24818 PREPARED BY : WMR	

Figure F.3 Pressure transducer calibration for the 10 k transducer

APPENDIX G

DENSITY MEASUREMENT TABLES

Table G. 1 Experimental Values of Temperature T , Pressure p , Density ρ , and Relative Density Deviations from Values Calculated with the reference equation[47] for Nitrogen

T/K	p/MPa	$\rho^{exp}/kg\cdot m^{-3}$	$\frac{100(\rho^{exp}-\rho^{EoS})}{\rho^{exp}}$	$\frac{100 U(\rho)}{\rho^{exp}}$
T = 303 K				
303.186	201.566	722.06	0.034	0.013
303.158	189.563	708.67	0.028	0.013
303.150	172.456	688.02	0.026	0.014
303.142	155.066	664.72	0.017	0.014
303.103	137.881	638.99	0.020	0.015
303.195	131.328	628.18	0.023	0.015
303.173	120.795	609.67	0.016	0.016
303.063	120.606	609.41	0.014	0.016
303.106	120.547	609.34	0.026	0.016
303.022	103.496	575.35	0.012	0.018
303.043	96.474	559.55	0.014	0.018
303.291	96.371	559.06	0.017	0.018
303.013	86.173	534.08	0.023	0.020
303.013	86.135	533.88	0.003	0.020

303.008	68.988	483.04	0.011	0.024
302.990	68.937	482.95	0.022	0.024
303.051	51.795	416.35	0.013	0.031
302.988	51.653	415.83	0.028	0.031
303.012	34.492	322.56	0.031	0.031
303.074	34.457	322.25	0.027	0.031
303.021	27.636	274.00	0.032	0.038
303.045	27.546	273.23	0.011	0.038
303.023	17.245	184.35	0.047	0.061
303.006	17.219	184.07	0.024	0.061
303.007	10.322	113.89	0.024	0.102
302.994	10.297	113.62	0.020	0.102
T = 349 K				
349.067	202.195	684.01	0.024	0.014
349.098	174.915	650.73	0.020	0.015
349.080	149.848	615.16	0.017	0.016
349.099	125.330	573.87	0.021	0.017
349.060	125.002	573.26	0.015	0.017
349.025	74.953	453.91	0.029	0.025
349.020	50.095	360.46	0.047	0.036
349.016	25.021	216.37	0.047	0.048
349.169	15.009	137.86	0.028	0.078

T = 398 K

398.246	103.665	488.09	0.032	0.021
398.306	74.966	411.69	0.051	0.027
398.302	50.105	320.57	0.056	0.040
398.286	49.957	319.96	0.062	0.040
398.046	24.864	187.32	0.076	0.054
398.092	7.640	63.04	0.086	0.167
398.175	7.636	62.99	0.088	0.167

T = 450 K

450.705	170.535	570.44	-0.016	0.017
450.664	150.110	539.40	-0.017	0.018
450.657	125.008	495.15	-0.009	0.020
450.717	100.222	442.28	0.002	0.023
450.612	100.131	442.13	0.002	0.023
450.682	74.979	374.74	0.006	0.029
450.647	49.982	286.72	-0.004	0.043
450.620	24.963	165.51	-0.009	0.059
450.695	9.985	71.56	-0.047	0.142

Table G. 2 Experimental Values of Temperature T, Pressure p, Density ρ , and Relative Density Deviations from Values Calculated with the reference EoS[49] for Pure Argon

T/K	p/MPa	$\rho^{exp}/kg\cdot m^{-3}$	$\frac{100(\rho^{exp}-\rho^{EoS})}{\rho^{exp}}$	$\frac{100 U(\rho)}{\rho^{exp}}$
T=303 K				
303.502	202.016	1210.00	-0.008	0.012
303.442	189.532	1187.74	-0.005	0.012
303.377	172.308	1154.36	-0.004	0.013
303.338	155.074	1117.19	-0.001	0.013
303.303	137.817	1075.21	0.001	0.014
303.325	120.607	1027.00	0.010	0.015
303.560	120.495	1026.26	0.015	0.015
303.305	103.574	971.11	0.016	0.016
303.279	86.178	902.00	0.026	0.019
303.306	69.029	815.65	0.028	0.023
303.270	51.669	698.58	0.031	0.031
303.279	34.325	529.58	0.036	0.031
303.340	27.483	441.71	0.022	0.039
303.444	17.223	286.09	0.062	0.063
303.333	17.221	286.17	0.047	0.063
303.370	6.879	112.71	0.106	0.161
T=349 K				

349.019	200.344	1136.71	0.005	0.013
349.000	188.653	1114.20	0.006	0.013
349.055	172.371	1080.17	0.009	0.014
349.031	155.215	1040.53	0.014	0.014
348.988	137.878	995.33	0.016	0.015
348.992	130.872	975.26	0.018	0.016
348.966	107.921	900.24	0.028	0.018
349.020	103.486	883.64	0.032	0.018
349.115	103.312	882.78	0.028	0.018
349.069	89.385	825.29	0.035	0.020
349.021	74.216	750.33	0.036	0.024
348.995	61.738	675.47	0.045	0.029
348.995	51.262	599.94	0.043	0.036
349.104	42.426	524.60	0.046	0.045
349.084	34.728	448.85	0.036	0.035
349.077	28.045	374.60	0.036	0.043
349.026	21.874	299.11	0.029	0.063
349.054	16.176	224.30	0.050	0.075
349.162	10.698	149.07	0.050	0.114
T=397 K				
397.429	144.540	940.22	0.024	0.016
397.364	134.978	912.88	0.026	0.017
397.035	130.557	900.05	0.036	0.017
397.014	102.220	801.10	0.048	0.020

397.023	79.985	701.30	0.055	0.025
397.008	64.529	614.85	0.068	0.031
397.553	64.122	611.41	0.048	0.031
396.987	48.021	500.40	0.071	0.043
396.958	36.163	400.08	0.055	0.038
395.987	25.916	300.46	0.072	0.054
397.658	16.819	199.70	0.088	0.081
397.489	8.201	98.96	0.118	0.164

T=450 K

450.674	170.077	937.29	0.027	0.016
450.684	141.891	862.84	0.026	0.018
450.714	118.061	787.20	0.021	0.020
450.658	117.962	786.95	0.024	0.020
450.702	98.081	711.42	0.021	0.023
450.679	80.966	634.18	0.013	0.027
450.656	66.925	559.74	0.015	0.033
450.675	54.977	486.41	0.013	0.040
450.717	44.952	416.45	0.002	0.050
450.737	34.987	338.47	0.004	0.045
450.750	25.933	259.90	0.022	0.059
450.746	17.913	184.30	0.021	0.084
450.718	9.936	104.32	0.022	0.150

Table G. 3 Experimental Values of Temperature T, Pressure p, Density ρ , and Relative Density Deviations from Values Calculated with the reference EoS[50] for Pure Helium using the titanium sinker

T/K	p/MPa	$\rho^{exp}/\text{kg}\cdot\text{m}^{-3}$	$\frac{100(\rho^{exp}-\rho^{EoS})}{\rho^{EoS}}$	$\frac{100 U(\rho)}{\rho^{exp}}$
T=303 K				
303.299	200.607	176.90	0.414	0.050
303.028	175.019	162.64	0.406	0.054
302.969	149.973	147.26	0.384	0.060
302.920	125.026	130.34	0.376	0.068
303.956	100.676	111.65	0.358	0.080
302.904	99.986	111.33	0.336	0.080
302.883	81.966	96.11	0.258	0.093
302.820	60.951	76.36	0.167	0.114
302.934	45.006	59.52	0.053	0.147
302.910	25.984	36.93	-0.014	0.237
302.887	10.947	16.53	-0.238	0.530
T=303 K				
303.672	100.074	111.20	0.322	0.080
303.513	100.059	111.20	0.297	0.080
303.425	74.971	89.67	0.219	0.100

303.474	32.869	45.41	0.027	0.192
303.547	15.932	23.52	-0.163	0.373
303.305	15.931	23.51	-0.277	0.373
303.714	9.772	14.80	-0.180	0.592

T=350 K

350.168	200.240	163.09	0.449	0.054
350.282	174.983	149.40	0.439	0.059
350.171	149.961	134.62	0.380	0.065
350.249	149.926	134.58	0.378	0.065
349.246	149.664	134.79	0.473	0.065
350.236	124.963	118.45	0.343	0.074
350.214	100.041	100.57	0.228	0.088
350.240	74.844	80.39	0.167	0.110
350.206	52.974	60.59	0.034	0.144
350.204	32.899	40.01	-0.307	0.218
350.207	15.971	20.61	-0.306	0.424
350.240	9.956	13.10	-0.562	0.668

T=399 K

398.996	159.651	129.49	0.538	0.068
399.216	149.678	123.67	0.528	0.071
399.226	124.762	108.32	0.463	0.081
399.225	99.919	91.52	0.367	0.096

399.258	87.256	82.27	0.307	0.107
398.823	87.208	82.31	0.315	0.107
399.260	72.811	71.09	0.245	0.125
399.261	49.837	51.65	0.134	0.169
399.291	24.853	27.68	0.077	0.315
399.339	9.922	11.59	0.115	0.754

T=450 K

450.713	169.850	124.93	0.590	0.070
450.708	149.667	113.95	0.537	0.077
450.670	124.891	99.48	0.460	0.088
450.738	100.447	83.93	0.366	0.105
450.692	100.017	83.64	0.350	0.105
450.702	84.852	73.22	0.261	0.120
450.679	70.630	62.90	0.219	0.140
450.729	57.920	53.12	0.197	0.164
450.713	45.911	43.33	0.109	0.201
450.686	22.843	22.89	0.086	0.381
450.703	9.873	10.27	0.214	0.850

Table G. 4 Experimental Values of Temperature T, Pressure p, Density ρ , and Relative Density Deviations from Values Calculated with the reference EoS[50] for Pure Helium using the silicon sinker

T/K	p/MPa	$\rho^{\text{exp}}/\text{kg}\cdot\text{m}^{-3}$	$\frac{100(\rho^{\text{exp}}-\rho^{\text{EoS}})}{\rho^{\text{EoS}}}$	$\frac{100 U(\rho)}{\rho^{\text{exp}}}$
T=304 K				
304.212	149.968	146.90	0.397	0.035
304.216	99.867	110.91	0.335	0.048
304.199	74.852	89.41	0.241	0.061
304.209	50.020	64.82	0.158	0.080
304.214	24.897	35.42	0.020	0.148
304.227	9.833	14.89	0.003	0.356

Table G. 5 Experimental Values of Temperature T , Pressure p , Density ρ , and Relative Density Deviations from Values Calculated with the GERG-2008 and AGA8-DC92 for a Binary Gas Mixture of Helium + Methane with a Molar Composition of (0.24515 He + 0.75485 CH₄)

T/K	p/MPa	$\rho^{exp}/\text{kg}\cdot\text{m}^{-3}$	$\frac{100(\rho^{exp}-\rho^{GERG})}{\rho^{exp}}$	$\frac{100(\rho^{exp}-\rho^{AGA8})}{\rho^{exp}}$	$\frac{100 U(\rho)}{\rho^{exp}}$
T = 303 K					
303.561	200.063	365.15	-1.452	3.039	0.021
303.532	175.093	350.89	-1.682	2.861	0.022
303.506	150.128	334.30	-1.985	2.628	0.023
303.476	125.091	314.37	-2.390	2.315	0.025
303.481	124.878	314.24	-2.374	2.329	0.025
303.505	100.007	289.58	-2.889	1.939	0.027
303.471	75.039	256.78	-3.627	1.378	0.032
303.470	49.969	208.55	-4.566	0.613	0.043
303.461	36.045	169.36	-4.848	0.183	0.046
303.513	25.973	131.65	-4.601	-0.203	0.060
303.495	17.950	94.85	-3.752	-0.470	0.086
303.496	10.957	58.60	-2.492	-0.558	0.140
303.491	4.989	26.35	-1.430	-0.630	0.310
T = 350 K					

350.053	200.209	344.56	-1.943	2.713	0.022
349.981	174.900	329.16	-2.206	2.478	0.023
349.962	149.969	311.61	-2.490	2.228	0.025
350.039	149.853	311.54	-2.473	2.242	0.025
349.960	125.072	290.66	-2.847	1.898	0.027
349.985	100.122	264.63	-3.276	1.485	0.030
349.971	85.022	245.35	-3.540	1.208	0.033
349.966	71.006	223.78	-3.853	0.862	0.037
349.926	50.975	184.21	-4.164	0.347	0.048
349.933	36.907	147.00	-4.117	-0.076	0.052
349.940	26.122	111.16	-3.650	-0.402	0.069
349.949	15.966	71.07	-2.577	-0.477	0.110
349.933	7.039	31.79	-1.361	-0.445	0.248

T = 395 K

395.889	199.699	326.90	-2.019	2.680	0.023
395.797	188.590	320.20	-2.100	2.597	0.024
395.775	172.492	309.62	-2.244	2.445	0.025
395.886	149.403	292.44	-2.484	2.183	0.026
396.528	148.094	291.01	-2.546	2.121	0.026
395.875	137.903	282.88	-2.609	2.039	0.027
395.863	122.648	268.80	-2.796	1.821	0.029
395.846	99.843	244.01	-3.086	1.446	0.032
395.830	81.418	219.40	-3.302	1.101	0.037
395.854	66.412	195.02	-3.418	0.802	0.042

398.593	66.285	193.58	-3.441	0.754	0.043
395.918	53.939	170.68	-3.408	0.546	0.050
395.877	36.954	129.51	-3.049	0.218	0.058
395.782	25.871	96.36	-2.369	0.135	0.079
395.887	19.417	74.54	-1.677	0.267	0.102
395.911	12.734	50.15	-0.725	0.575	0.153
395.832	6.315	25.46	0.961	1.601	0.302

T = 450 K

450.678	169.992	287.49	-2.598	1.997	0.026
450.702	150.015	272.10	-2.786	1.738	0.028
450.685	124.971	249.70	-3.015	1.387	0.031
450.651	99.956	222.44	-3.244	0.969	0.035
450.694	79.090	194.34	-3.369	0.582	0.041
450.676	75.506	188.80	-3.425	0.468	0.043
450.674	60.940	164.17	-3.405	0.164	0.051
450.643	46.943	136.08	-3.224	-0.131	0.064
450.627	34.918	107.64	-2.873	-0.355	0.069
450.627	23.953	77.71	-2.311	-0.473	0.096
450.607	14.956	50.27	-1.634	-0.443	0.150
450.597	5.982	20.62	-0.911	-0.426	0.367

Table G. 6 Experimental Values of Temperature T , Pressure p , Density ρ , and Relative Density Deviations from Values Calculated with the GERG-2008 and AGA8-DC92 for a Binary Gas Mixture of Helium + Methane with a Molar Composition of (0.54601 He + 0.45399 CH₄)

T/K	p/MPa	$\rho^{\text{exp}}/\text{kg}\cdot\text{m}^{-3}$	$\frac{100(\rho^{\text{exp}} - \rho^{\text{GERG}})}{\rho^{\text{exp}}}$	$\frac{100(\rho^{\text{exp}} - \rho^{\text{AGA8}})}{\rho^{\text{exp}}}$	$\frac{100 U(\rho)}{\rho^{\text{exp}}}$
T = 303 K					
303.564	200.803	303.81	-2.132	7.299	0.025
303.513	175.024	287.35	-2.753	6.726	0.026
303.511	150.017	268.91	-3.470	6.057	0.028
303.530	149.909	268.78	-3.485	6.044	0.028
303.486	125.073	247.32	-4.289	5.265	0.031
303.479	100.028	221.03	-5.252	4.276	0.036
303.485	75.046	188.09	-6.210	3.094	0.043
303.493	50.017	144.59	-6.717	1.741	0.060
303.512	36.028	113.18	-6.516	0.790	0.068
303.480	26.017	86.69	-5.781	0.159	0.087
303.481	18.003	62.67	-4.682	-0.237	0.122
303.509	10.990	39.38	-3.796	-0.916	0.195
303.485	4.977	18.16	-2.865	-1.499	0.424
T = 350 K					

350.381	199.938	284.34	-2.705	6.675	0.027
350.333	175.038	268.08	-3.233	6.093	0.028
350.306	150.050	249.38	-3.833	5.398	0.031
350.277	125.025	227.53	-4.486	4.581	0.034
350.249	100.066	201.43	-5.162	3.605	0.039
350.409	99.950	201.26	-5.149	3.606	0.039
350.274	84.981	182.86	-5.517	2.943	0.044
350.265	70.970	163.15	-5.751	2.272	0.050
350.243	51.010	129.65	-5.781	1.208	0.065
350.235	36.969	101.05	-5.408	0.381	0.074
350.234	25.997	75.28	-4.538	-0.064	0.099
350.312	15.954	48.57	-3.235	-0.274	0.155
350.303	7.007	22.18	-1.689	-0.300	0.340

T = 399 K

398.671	199.834	267.22	-2.990	6.134	0.028
398.656	174.553	250.44	-3.469	5.499	0.030
398.654	150.041	232.02	-3.929	4.821	0.033
398.639	125.003	210.21	-4.421	4.004	0.037
398.650	100.042	184.47	-4.878	3.047	0.042
398.675	99.940	184.31	-4.899	3.023	0.042
398.636	85.004	166.49	-5.065	2.419	0.047
398.640	71.036	147.60	-5.162	1.769	0.054
398.695	51.020	115.97	-4.961	0.799	0.071
398.671	36.959	89.70	-4.450	0.147	0.083

398.661	26.021	66.49	-3.669	-0.204	0.111
398.653	15.989	42.75	-2.675	-0.413	0.174
398.655	7.002	19.48	-1.241	-0.199	0.382

T = 450 K

450.701	169.855	230.95	-3.554	4.876	0.033
450.669	150.008	215.90	-3.850	4.311	0.035
450.651	125.036	194.45	-4.185	3.529	0.039
450.655	100.013	169.29	-4.462	2.614	0.046
450.696	99.848	169.04	-4.497	2.573	0.046
450.656	78.944	144.44	-4.531	1.769	0.054
450.661	60.974	119.73	-4.403	0.984	0.067
450.643	46.993	97.75	-4.085	0.380	0.083
450.652	34.875	76.40	-3.493	0.005	0.097
450.649	23.969	54.96	-2.853	-0.340	0.134
450.653	14.947	35.59	-2.038	-0.414	0.207
450.665	5.991	14.80	-0.876	-0.200	0.499

Table G. 7 Experimental Values of Temperature T , Pressure p , Density ρ , and Relative Density Deviations from Values Calculated with the GERG-2008 and AGA8-DC92 for a Binary Gas Mixture of Helium + Methane with a Molar Composition of (0.74768 He + 0.25232 CH₄)

T/K	p/MPa	$\rho^{exp}/\text{kg}\cdot\text{m}^{-3}$	$\frac{100(\rho^{exp}-\rho^{GERG})}{\rho^{exp}}$	$\frac{100(\rho^{exp}-\rho^{AGA8})}{\rho^{exp}}$	$\frac{100 U(\rho)}{\rho^{exp}}$
T = 303 K					
303.521	199.782	252.33	-0.745	10.589	0.030
303.510	175.044	236.45	-1.416	9.711	0.033
303.513	150.052	218.30	-2.176	8.672	0.035
303.800	149.977	218.06	-2.213	8.632	0.035
303.152	125.044	197.45	-3.066	7.392	0.039
303.155	99.985	172.94	-3.929	5.935	0.045
303.173	74.942	143.63	-4.631	4.267	0.055
303.163	49.733	107.03	-4.933	2.280	0.076
303.189	36.009	82.99	-4.657	1.150	0.090
303.157	25.985	63.12	-4.083	0.419	0.117
303.897	18.012	45.46	-3.523	-0.241	0.164
303.612	10.893	28.60	-2.540	-0.446	0.259
T = 350 K					
348.981	200.312	236.11	-1.090	9.728	0.033

348.853	189.494	229.49	-1.316	9.369	0.033
348.709	172.116	218.04	-1.748	8.695	0.035
348.600	154.969	205.81	-2.176	7.979	0.037
348.527	138.184	192.74	-2.616	7.200	0.045
348.602	138.103	192.67	-2.607	7.202	0.040
348.595	114.583	172.19	-3.180	6.013	0.045
348.565	94.322	151.98	-3.659	4.816	0.051
348.758	77.075	132.38	-3.958	3.695	0.059
349.025	61.931	112.94	-4.076	2.627	0.071
349.100	48.546	93.67	-4.000	1.651	0.085
349.101	36.662	74.57	-3.725	0.790	0.098
349.019	25.955	55.49	-3.179	0.158	0.132
348.940	16.102	36.00	-2.658	-0.505	0.204
348.917	10.346	23.78	-2.033	-0.616	0.310
348.915	5.856	13.78	-1.239	-0.420	0.535
348.886	2.829	6.73	-1.165	-0.756	1.098
350.105	199.893	235.52	-1.083	9.710	0.032
350.095	175.083	219.58	-1.683	8.782	0.035
350.147	149.939	201.53	-2.286	7.742	0.038
350.097	149.697	201.30	-2.326	7.704	0.038
350.074	100.022	157.48	-3.524	5.138	0.049
350.068	71.142	124.72	-3.999	3.273	0.063
350.097	36.685	74.48	-3.633	0.857	0.098
350.053	6.943	16.21	-1.351	-0.395	0.455

T = 398 K

397.578	189.414	213.98	-1.490	8.492	0.036
397.751	172.318	202.80	-1.832	7.842	0.038
397.711	155.111	190.82	-2.133	7.169	0.040
397.705	137.821	177.68	-2.468	6.408	0.043
397.655	118.579	161.59	-2.836	5.457	0.047
397.636	118.525	161.53	-2.843	5.447	0.048
397.597	104.939	149.13	-3.053	4.739	0.051
397.564	94.905	139.28	-3.200	4.173	0.055
397.558	77.013	120.06	-3.388	3.076	0.064
397.557	62.792	103.03	-3.420	2.161	0.076
397.570	61.955	101.99	-3.392	2.124	0.077
397.561	48.983	84.74	-3.232	1.309	0.093
397.547	36.256	66.01	-2.894	0.557	0.110
397.548	24.957	47.64	-2.369	0.029	0.153
397.561	15.993	31.75	-1.687	-0.147	0.230
397.577	9.991	20.39	-1.052	-0.086	0.359
397.609	5.022	10.51	-0.176	0.318	0.698

T = 450 K

450.662	170.040	187.34	-1.665	7.126	0.040
450.670	149.956	173.39	-1.962	6.337	0.044
450.645	124.656	153.83	-2.347	5.194	0.049
450.642	99.932	132.08	-2.712	3.875	0.058
450.642	99.932	132.08	-2.712	3.875	0.058

450.660	78.980	111.29	-2.793	2.751	0.069
450.637	60.998	91.17	-2.731	1.716	0.084
450.629	46.968	73.63	-2.613	0.850	0.105
450.667	23.644	40.40	-1.852	-0.181	0.180
450.626	14.998	26.47	-1.522	-0.494	0.275
450.599	5.990	10.96	-0.855	-0.454	0.665

Table G. 8 Experimental Values of Temperature T , Pressure p , Density ρ , and Relative Density Deviations from Values Calculated with the GERG-2008 and AGA8-DC92 for a Binary Gas Mixture of Helium + Methane with a Molar Composition of (0.27079 He + 0.72921 CH₄)

T/K	p/MPa	$\rho^{exp}/\text{kg}\cdot\text{m}^{-3}$	$\frac{100(\rho^{exp} - \rho^{GERG})}{\rho^{exp}}$	$\frac{100(\rho^{exp} - \rho^{AGA8})}{\rho^{exp}}$	$\frac{100 U(\rho)}{\rho^{exp}}$
303.532	149.917	329.15	-2.166	2.923	0.024
303.490	124.756	308.88	-2.601	2.588	0.025
303.489	100.028	284.03	-3.186	2.137	0.028
303.536	99.846	283.76	-3.207	2.118	0.028
303.483	74.986	250.80	-3.991	1.515	0.034
303.537	49.878	202.43	-4.906	0.736	0.046
303.480	24.988	123.04	-4.776	-0.200	0.067
303.502	9.994	51.79	-2.361	-0.478	0.164

Table G. 9 Experimental Values of Temperature T , Pressure p , Density ρ , and Relative Density Deviations from Values Calculated with the GERG-2008 and AGA8-DC92 for a Binary Gas Mixture of Helium + Methane with a Molar Composition of (0.50055 He + 0.49945 CH₄)

T/K	p/MPa	$\rho^{exp}/\text{kg}\cdot\text{m}^{-3}$	$\frac{100(\rho^{exp} - \rho^{GERG})}{\rho^{exp}}$	$\frac{100(\rho^{exp} - \rho^{AGA8})}{\rho^{exp}}$	$\frac{100 U(\rho)}{\rho^{exp}}$
303.497	149.941	279.42	-3.463	5.477	0.028
303.467	125.008	257.89	-4.253	4.759	0.031
303.549	124.891	257.71	-4.270	4.743	0.031
303.460	100.052	231.63	-5.183	3.870	0.035
303.462	77.040	201.25	-6.090	2.889	0.041
303.496	49.960	153.26	-6.830	1.496	0.058
303.433	15.962	59.95	-4.315	-0.283	0.129
303.463	9.868	38.10	-2.827	-0.242	0.205
303.494	4.887	19.19	-1.459	-0.146	0.407

Table G. 10 Experimental Values of Temperature T , Pressure p , Density ρ , and Relative Density Deviations from Values Calculated with the GERG-2008 and AGA8-DC92 for a Binary Gas Mixture of Helium + Methane with a Molar Composition of (0.73540 He + 0.26460 CH₄)

T/K	p/MPa	$\rho^{\text{exp}}/\text{kg}\cdot\text{m}^{-3}$	$\frac{100(\rho^{\text{exp}} - \rho^{\text{GERG}})}{\rho^{\text{exp}}}$	$\frac{100(\rho^{\text{exp}} - \rho^{\text{AGA8}})}{\rho^{\text{exp}}}$	$\frac{100 U(\rho)}{\rho^{\text{exp}}}$
303.172	150.071	221.74	-2.320	8.527	0.037
303.158	125.044	200.77	-3.148	7.341	0.041
303.155	100.030	176.14	-4.008	5.927	0.047
303.157	99.998	176.11	-4.002	5.929	0.047
303.164	74.828	146.31	-4.726	4.282	0.057
303.235	24.951	62.30	-4.046	0.447	0.123
303.515	9.990	26.99	-2.238	-0.230	0.280

APPENDIX H

MODEL AND FIT RESULTS FOR DIMENSIONLESS INTERACTION

RESIDUAL HELMHOLTZ ENERGY

Table H.1. Model and numerical parameters for methane + nitrogen

$$\text{Model: } \alpha_{12}^r(\rho, T) = \frac{n_1 \rho + n_2 \rho^2 + n_3 \rho^3}{1 + n_4 \rho}$$

$n_1 = c_{0,1} + c_{1,1} / T$	$\frac{c_{0,1}}{\text{m}^3 \cdot \text{kmol}^{-1}}$	$\frac{c_{1,1}}{\text{m}^3 \cdot \text{K} \cdot \text{kmol}^{-1}}$
	0.0546	-21.664
$n_2 = c_{0,2} + c_{1,2} / T$	$\frac{c_{0,2}}{\text{m}^6 \cdot \text{kmol}^{-2}}$	$\frac{c_{1,2}}{\text{m}^6 \cdot \text{K} \cdot \text{kmol}^{-2}}$
	-5.846E-04	0.5144
$n_3 = c_{0,3} + c_{1,3} / T$	$\frac{c_{0,3}}{\text{m}^9 \cdot \text{kmol}^{-3}}$	$\frac{c_{1,3}}{\text{m}^9 \cdot \text{K} \cdot \text{kmol}^{-3}}$
	2.319E-06	-0.001986
$n_4 = c_{0,4} + c_{1,4} / T$	$\frac{c_{0,4}}{\text{m}^3 \cdot \text{kmol}^{-1}}$	$\frac{c_{1,4}}{\text{m}^3 \cdot \text{K} \cdot \text{kmol}^{-1}}$
	-0.0169	-1.2578

Table H.2. Model and numerical parameters for methane + ethane

$$\text{Model: } \alpha_{12}^r(\rho, T) = \frac{n_1 \rho + n_2 \rho^2}{1 + n_3 \rho}$$

$n_1 = c_{0,1} + c_{1,1}/T + c_{1,2}/T^2$	$\frac{c_{0,1}}{\text{m}^3 \cdot \text{kmol}^{-1}}$	$\frac{c_{1,1}}{\text{m}^3 \cdot \text{K} \cdot \text{kmol}^{-1}}$	$\frac{c_{1,2}}{\text{m}^3 \cdot \text{K}^2 \cdot \text{kmol}^{-1}}$
	0.055016	-26.7853	-4807.96
$n_2 = c_{0,2} + c_{1,2}/T$	$\frac{c_{0,2}}{\text{m}^6 \cdot \text{kmol}^{-2}}$	$\frac{c_{1,2}}{\text{m}^6 \cdot \text{K} \cdot \text{kmol}^{-2}}$	
	0	0.8953	
$n_3 = c_{0,3} + c_{1,3}/T$	$\frac{c_{0,3}}{\text{m}^3 \cdot \text{kmol}^{-1}}$	$\frac{c_{1,3}}{\text{m}^3 \cdot \text{K} \cdot \text{kmol}^{-1}}$	
	-0.0342	6.4460	

Table H.3. Model and numerical parameters for nitrogen + carbon dioxide

$$\text{Model: } \alpha_{12}^r(\rho, T) = \frac{n_1 \rho + n_2 \rho^2 + n_3 \rho^3}{1 + n_4 \rho}$$

$n_1 = c_{0,1} + c_{1,1}/T$	$\frac{c_{0,1}}{\text{m}^3 \cdot \text{kmol}^{-1}}$	$\frac{c_{1,1}}{\text{m}^3 \cdot \text{K} \cdot \text{kmol}^{-1}}$
	0.0631	-31.007
$n_2 = c_{0,2} + c_{1,2}/T$	$\frac{c_{0,2}}{\text{m}^6 \cdot \text{kmol}^{-2}}$	$\frac{c_{1,2}}{\text{m}^6 \cdot \text{K} \cdot \text{kmol}^{-2}}$
	-0.00118	0.908
$n_3 = c_{0,3} + c_{1,3}/T$	$\frac{c_{0,3}}{\text{m}^9 \cdot \text{kmol}^{-3}}$	$\frac{c_{1,3}}{\text{m}^9 \cdot \text{K} \cdot \text{kmol}^{-3}}$
	4.159E-06	-0.00513
$n_4 = c_{0,4} + c_{1,4}/T$	$\frac{c_{0,4}}{\text{m}^3 \cdot \text{kmol}^{-1}}$	$\frac{c_{1,4}}{\text{m}^3 \cdot \text{K} \cdot \text{kmol}^{-1}}$
	-0.0191	-1.819

Table H.4. Model and numerical parameters for methane + carbon dioxide

$$\text{Model: } \alpha_{12}^r(\rho, T) = \frac{n_1 \rho + n_2 \rho^2 + n_3 \rho^3 + n_4 \rho^4}{1 + n_5 \rho}$$

$n_1 = c_{0,1} + c_{1,1}/T$	$\frac{c_{0,1}}{\text{m}^3 \cdot \text{kmol}^{-1}}$	$\frac{c_{1,1}}{\text{m}^3 \cdot \text{K} \cdot \text{kmol}^{-1}}$	
	0.0698	-39.8352	
$n_2 = c_{0,2} + c_{1,2}/T + c_{2,2}x_1x_2$	$\frac{c_{0,2}}{\text{m}^6 \cdot \text{kmol}^{-2}}$	$\frac{c_{1,2}}{\text{m}^6 \cdot \text{K} \cdot \text{kmol}^{-2}}$	$\frac{c_{2,2}}{\text{m}^6 \cdot \text{kmol}^{-2}}$
	8.3497E-04	0	3.3517E-04
$n_3 = c_{0,3} + c_{1,3}/T$	$\frac{c_{0,3}}{\text{m}^9 \cdot \text{kmol}^{-3}}$	$\frac{c_{1,3}}{\text{m}^9 \cdot \text{K} \cdot \text{kmol}^{-3}}$	
	8.7271E-05	-0.0484	
$n_4 = c_{0,4} + c_{1,4}/T$	$\frac{c_{0,4}}{\text{m}^{12} \cdot \text{kmol}^{-4}}$	$\frac{c_{1,4}}{\text{m}^{12} \cdot \text{K} \cdot \text{kmol}^{-4}}$	
	0	0.00114	
$n_5 = c_{0,5} + c_{1,5}/T$	$\frac{c_{0,5}}{\text{m}^3 \cdot \text{kmol}^{-1}}$	$\frac{c_{1,5}}{\text{m}^3 \cdot \text{K} \cdot \text{kmol}^{-1}}$	
	0	0.0225	

Table H.5. Model and numerical parameters for ethane(1) + carbon dioxide(2)

$$\text{Model: } \alpha_{12}^r(\rho, T) = \frac{n_1 \rho + n_2 \rho^2 + n_3 \rho^3}{1 + n_4 \rho + n_5 \rho^2}$$

$n_1 = c_{0,1} + c_{1,1}/T + c_{2,1}/T^2$	$\frac{c_{0,1}}{\text{m}^3 \cdot \text{kmol}^{-1}}$	$\frac{c_{1,1}}{\text{m}^3 \cdot \text{K} \cdot \text{kmol}^{-1}}$	$\frac{c_{2,1}}{\text{m}^3 \cdot \text{K}^2 \cdot \text{kmol}^{-1}}$
	0.0399	-11.8255	-11120
$n_2 = c_{0,2} + c_{1,2}/T + c_{2,2}/T^2 + c_{3,2}x_1x_2(c_{4,2}x_1 + x_2) + c_{5,2}x_1^2x_2^2(c_{6,2}x_1 + x_2)$	$\frac{c_{0,2}}{\text{m}^6 \cdot \text{kmol}^{-2}}$	$\frac{c_{1,2}}{\text{m}^6 \cdot \text{K} \cdot \text{kmol}^{-2}}$	$\frac{c_{2,2}}{\text{m}^6 \cdot \text{K}^2 \cdot \text{kmol}^{-2}}$
	-0.0036585	3.5306	0
$\frac{c_{3,2}}{\text{m}^6 \cdot \text{kmol}^{-2}}$	$\frac{c_{4,2}}{\text{m}^6 \cdot \text{kmol}^{-2}}$	$\frac{c_{5,2}}{\text{m}^6 \cdot \text{kmol}^{-2}}$	$\frac{c_{6,2}}{\text{m}^6 \cdot \text{kmol}^{-2}}$
-1.4296E-03	0.6860	4.08195E-03	0.3323
$n_3 = c_{0,3} + c_{1,3}/T$	$\frac{c_{0,3}}{\text{m}^9 \cdot \text{kmol}^{-3}}$	$\frac{c_{1,3}}{\text{m}^9 \cdot \text{K} \cdot \text{kmol}^{-3}}$	
	-5.0017E-05	-0.02222	

Table H.5 (Cont.). Model and numerical parameters for ethane (1)+ carbon dioxide(2)

$n_4 = c_{0,4} + c_{1,4} / T$	$\frac{c_{0,4}}{\text{m}^3 \cdot \text{kmol}^{-1}}$	$\frac{c_{1,4}}{\text{m}^3 \cdot \text{K} \cdot \text{kmol}^{-1}}$
	-0.1240	25.8827
$n_5 = c_{0,5} + c_{1,5} / T$	$\frac{c_{0,5}}{\text{m}^6 \cdot \text{kmol}^{-2}}$	$\frac{c_{1,5}}{\text{m}^6 \cdot \text{K} \cdot \text{kmol}^{-2}}$
	2.6322E-03	-0.8242

Table H.6. Model and numerical parameters for argon + nitrogen

$$\text{Model: } \alpha_{12}^r(\rho, T) = \frac{n_1 \rho + n_2 \rho^2 + n_3 \rho^3}{1 + n_4 \rho}$$

$n_1 = c_{0,1} + c_{1,1}/T$	$\frac{c_{0,1}}{\text{m}^3 \cdot \text{kmol}^{-1}}$	$\frac{c_{1,1}}{\text{m}^3 \cdot \text{K} \cdot \text{kmol}^{-1}}$	$\frac{c_{2,1}}{\text{m}^3 \cdot \text{K}^2 \cdot \text{kmol}^{-1}}$
	0.0382	-11.361	-930.44
$n_2 = c_{0,2} + c_{1,2}/T + c_{2,2}/T^2 + c_{3,2}x_1x_2$	$\frac{c_{0,2}}{\text{m}^6 \cdot \text{kmol}^{-2}}$	$\frac{c_{1,2}}{\text{m}^6 \cdot \text{K} \cdot \text{kmol}^{-2}}$	$\frac{c_{2,2}}{\text{m}^6 \cdot \text{K}^2 \cdot \text{kmol}^{-2}}$
	2.3108E-03	-1.2995	246.57
			-1.5111E-04
$n_3 = c_{0,3} + c_{1,3}/T + c_{2,3}/T^2$	$\frac{c_{0,3}}{\text{m}^9 \cdot \text{kmol}^{-3}}$	$\frac{c_{1,3}}{\text{m}^9 \cdot \text{K} \cdot \text{kmol}^{-3}}$	$\frac{c_{2,3}}{\text{m}^9 \cdot \text{K}^2 \cdot \text{kmol}^{-3}}$
	-3.5199E-04	0.21204	-31.873
$n_4 = c_{0,4} + c_{1,4}/T + c_{2,4}/T^2$	$\frac{c_{0,4}}{\text{m}^3 \cdot \text{kmol}^{-1}}$	$\frac{c_{1,4}}{\text{m}^3 \cdot \text{K} \cdot \text{kmol}^{-1}}$	$\frac{c_{2,4}}{\text{m}^3 \cdot \text{K}^2 \cdot \text{kmol}^{-1}}$
	-0.35267	200.39	-29737

Table H.7. Model and numerical parameters for nitrogen + hydrogen

$$\text{Model: } \alpha_{12}^r(\rho, T) = \frac{n_1 \rho + n_2 \rho^2}{1 + n_3 \rho}$$

$n_1 = c_{0,1} + c_{1,1}/T$	$\frac{c_{0,1}}{\text{m}^3 \cdot \text{kmol}^{-1}}$	$\frac{c_{1,1}}{\text{m}^3 \cdot \text{K} \cdot \text{kmol}^{-1}}$	
	0.0302	-5.2699	
$n_2 = c_{0,2} + c_{1,2}/T + c_{2,2}x_1x_2$	$\frac{c_{0,2}}{\text{m}^6 \cdot \text{kmol}^{-2}}$	$\frac{c_{1,2}}{\text{m}^6 \cdot \text{K} \cdot \text{kmol}^{-2}}$	$\frac{c_{2,2}}{\text{m}^6 \cdot \text{kmol}^{-2}}$
	0	6.7039E-02	-3.4443E-05
$n_3 = c_{0,3}$	$\frac{c_{0,3}}{\text{m}^9 \cdot \text{kmol}^{-3}}$		
	-8.1155E-03		

Table H.8. Model and numerical parameters for helium(2) + argon(1)

$$\text{Model: } \alpha_{12}^r(\rho, T) = \frac{n_1 \rho + n_2 \rho^2}{1 + n_3 \rho}$$

$n_1 = c_{0,1}$	$\frac{c_{0,1}}{\text{m}^3 \cdot \text{kmol}^{-1}}$		
	0.019779		
$n_2 = c_{0,2} + c_{1,2} x_1 x_2 (c_{2,2} x_1 + x_2)$	$\frac{c_{0,2}}{\text{m}^6 \cdot \text{kmol}^{-2}}$	$\frac{c_{1,2}}{\text{m}^6 \cdot \text{kmol}^{-2}}$	$\frac{c_{2,2}}{\text{m}^6 \cdot \text{kmol}^{-2}}$
	-5.8262E-04	3.0871E-03	-0.72622
$n_3 = c_{0,3} + c_{1,3} x_1 x_2 (c_{2,3} x_1 + x_2)$	$\frac{c_{0,3}}{\text{m}^3 \cdot \text{kmol}^{-1}}$	$\frac{c_{1,3}}{\text{m}^3 \cdot \text{kmol}^{-1}}$	$\frac{c_{02,3}}{\text{m}^3 \cdot \text{kmol}^{-1}}$
	-0.031169	0.14208	-0.69583

Table H.9. Model and numerical parameters for helium + krypton

Model: $\alpha_{12}^r(\rho, T) = \frac{n_1 \rho}{1 + n_3 \rho}$

$n_1 = c_{0,1} + c_{1,1}/T + c_{2,1}/T^2$	$\frac{c_{0,1}}{\text{m}^3 \cdot \text{kmol}^{-1}}$	$\frac{c_{1,1}}{\text{m}^3 \cdot \text{K} \cdot \text{kmol}^{-1}}$	$\frac{c_{2,1}}{\text{m}^3 \cdot \text{K}^2 \cdot \text{kmol}^{-1}}$
	0.016973	3.7931	-693.90
$n_2 = c_{0,2} + c_{1,2}/T + c_{2,2}x_1x_2$	$\frac{c_{0,2}}{\text{m}^6 \cdot \text{kmol}^{-2}}$	$\frac{c_{1,2}}{\text{m}^6 \cdot \text{K} \cdot \text{kmol}^{-2}}$	$\frac{c_{2,2}}{\text{m}^6 \cdot \text{kmol}^{-2}}$
	-1.0134	3.9256	0.98854

Table H.10. Model and numerical parameters for helium (2)+ nitrogen(1)

$$\text{Model: } \alpha_{12}^r(\rho, T) = \frac{n_1\rho + n_2\rho^2 + n_3\rho^3}{1 + n_4\rho}$$

$n_1 = c_{0,1}$	$\frac{c_{0,1}}{\text{m}^3 \cdot \text{kmol}^{-1}}$		
	0.020918		
$n_2 = c_{0,2} + c_{1,2}x_1x_2(c_{2,2}x_1 + x_2)$	$\frac{c_{0,2}}{\text{m}^6 \cdot \text{kmol}^{-2}}$	$\frac{c_{1,2}}{\text{m}^6 \cdot \text{kmol}^{-2}}$	$\frac{c_{2,2}}{\text{m}^6 \cdot \text{kmol}^{-2}}$
	-6.5322E-04	1.4028E-03	0.60245
$n_3 = c_{0,3}$	$\frac{c_{0,3}}{\text{m}^9 \cdot \text{kmol}^{-3}}$		
	-6.7647E-06		
$n_4 = c_{0,4} + c_{1,4}x_1x_2(c_{2,4}x_1 + x_2)$	$\frac{c_{0,4}}{\text{m}^3 \cdot \text{kmol}^{-1}}$	$\frac{c_{1,4}}{\text{m}^3 \cdot \text{kmol}^{-1}}$	$\frac{c_{02,4}}{\text{m}^3 \cdot \text{kmol}^{-1}}$
	-0.03910	0.049528	0.79061

Table H.11. Model and numerical parameters for helium(2) + methane(1)

$$\text{Model: } \alpha_{12}^r(\rho, T) = \frac{n_1 \rho + n_2 \rho^2}{1 + n_3 \rho}$$

$n_1 = c_{0,1} + c_{1,1}/T$	$\frac{c_{0,1}}{\text{m}^3 \cdot \text{kmol}^{-1}}$	$\frac{c_{1,1}}{\text{m}^3 \cdot \text{K} \cdot \text{kmol}^{-1}}$		
	0.033658	-0.28104		
$n_2 = c_{0,2} + c_{1,2}x_1x_2(c_{2,2}x_1 + x_2)$	$\frac{c_{0,2}}{\text{m}^6 \cdot \text{kmol}^{-2}}$	$\frac{c_{1,2}}{\text{m}^6 \cdot \text{kmol}^{-2}}$	$\frac{c_{2,2}}{\text{m}^6 \cdot \text{kmol}^{-2}}$	
	-8.5185E-04	-1.3038E-03	-0.98459	
$n_3 = c_{0,3} + c_{1,3}x_1x_2(c_{2,3}x_1 + x_2)$	$\frac{c_{0,3}}{\text{m}^3 \cdot \text{kmol}^{-1}}$	$\frac{c_{1,3}}{\text{m}^3 \cdot \text{kmol}^{-1}}$	$\frac{c_{02,3}}{\text{m}^3 \cdot \text{kmol}^{-1}}$	
	-0.0205097	-0.024967	-1.3006	